ERCOFTAC

Bulletin

March 2012

90

European Research Community On Flow, Turbulence and Combustion

ERCOFTAC is a leading European association of research, education and industry groups in the technology of flow, turbulence and combustion. The main objectives of *ERCOFTAC* are: To promote joint efforts of European research institutes and industries with the aim of **exchanging technical and scientific information**; to promote **Pilot Centres** for collaboration, stimulation and application of research across Europe; to stimulate, through the creation of **Special Interest Groups**, well-coordinated European-wide research efforts on specific topics; to stimulate the creation of advanced training activities; and to be influential on funding agencies, governments, the European Commission and the European Parliament.

www.ercoftac.org

Honorary Presidents

Mathieu, J.   Spalding, D.B.

Executive Committee

Chairman	Hutton, A.G.
	Airbus UK
	Building 09B
	Bristol BS99 7AR
	United Kingdom
	Tel: +44 117 936 7519
	anthony.hutton@airbus.com
Deputy Chairman	Tomboulides. A.
Deputy Chairman	Hirsch, C.
Treasurer	Duursma, R.P.J.
Deputy Treasurer	Ooms, G.
SPC Chairman	Geurts, B.J.
SPC Deputy Chairman	Von Terzi, D.
IPC Chairman	Geuzaine, P.
IPC Deputy Chairman	Oliemans, R.V.A.
Horizon 10 Chairman	Jakirlic, S.
Ind. Engagement Officer	Seoud, R.E.
Knowledge Base Editor	Rodi, W.
Bulletin Editor	Elsner, W.
Observer	Hunt, J.
Observer	Jacquin, L.
Secretary	Borhani, N.

ERCOFTAC Seat of the Organisation

Director	Hirsch, C.
	Numeca International
	Chaussée de la Hulpe 189
	Terhulpsesteenweg
	B-1170 Brussels
	Belgium
	Tel: +32 2 643 3572
	Fax: +32 2 647 9398
	ado@ercoftac.be
Secretaries	Bongaerts, S.
	stephane.bongaerts@ercoftac.be
	Laurent, A.
	anne.laurent@ercoftac.be

Scientific Programme Committee

Chairman	Geurts, B.J.
	University of Twente
	Mathematical Sciences
	PO Box 217
	NL-7500 AE Enschede
	The Netherlands
	Tel: +31 53 489 4125
	b.j.geurts@utwente.nl
Deputy Chairman	Von Terzi, D.

Industrial Programme Committee

Chairman	Geuzaine, P.
Deputy Chairman	Oliemans, R.V.A.
Engagement Officer	Seoud, R.E.
	ERCOFTAC
	Crown House
	72 Hammersmith Road
	London W14 8TH
	United Kingdom
	Tel: +44 207 559 1430
	Fax: +44 207 559 1428
	richard.seoud-ieo@ercoftac.org

ERCOFTAC Central Administration and Development Office

ERCOFTAC CADO
Crown House
72 Hammersmith Road
London W14 8TH
United Kingdom
Tel: +44 (0)207 559 1427
Fax: +44 (0)207 559 1428

CADO Manager and Industrial Engagement Officer
Richard Seoud
Tel: +44 (0)207 559 1430
Richard.Seoud-ieo@ercoftac.org

ERCOFTAC Bulletin 90, March 2012

TABLE OF CONTENTS

NEXT *ERCOFTAC* EVENTS

ERCOFTAC SPRING FESTIVAL
10TH MAY 2012
HELSINKI, FINLAND.

ERCOFTAC SPC, IPC & MB-GA MEETINGS
11TH MAY 2012
HELSINKI, FINLAND.

A note from the Editor

The first issue of 2012 of ERCOFTAC Bulletin brings some changes to our journal. First, from 2012 the task of editing and publishing of the Bulletin has been transferred from Ecole Polytechnique Federale de Lausanne to Częstochowa University of Technology, Poland. I am pleased to welcome the new Editor Dr Maciej Marek and his co-worker the Technical Editor Łukasz Kuban MSc. At this point, it is necessary to express gratitude to the previous publisher, who hosted the Bulletin for many years. The outstanding contribution and effort made by the former Editor Dr Navid Borhani, who maintained to keep the magazine on high editorial level should be emphasized.

Changing the publisher is a good moment to refresh the appearance of the Bulletin. After the discussion among the board of the Executive Committee, it was decided to choose a new cover that you have in your hands. I hope that this refreshed form will obtain your approval. Small changes in the structure, resulting from the newly developed layout, have also been implemented.

We will try to maintain a high level of the Bulletin in future. The success of the Bulletin depends upon all contributing authors. That is why I would like to thank all past and the new contributors, who respond positively to the invitation of Editorial Board.

Witold Elsner
Editor-in-Chief

The ERCOFTAC Best Practice Guidelines for Industrial Computational Fluid Dynamics

The Best Practice Guidelines (BPG) were commissioned by ERCOFTAC following an extensive consultation with European industry which revealed an urgent demand for such a document. The first edition was completed in January 2000 and constitutes generic advice on how to carry out quality CFD calculations. The BPG therefore address mesh design; construction of numerical boundary conditions where problem data is uncertain; mesh and model sensitivity checks; distinction between numerical and turbulence model inadequacy; preliminary information regarding the limitations of turbulence models etc. The aim is to encourage a common best practice by virtue of which separate analyses of the same problem, using the same model physics, should produce consistent results. Input and advice was sought from a wide cross-section of CFD specialists, eminent academics, end-users and, (particularly important) the leading commercial code vendors established in Europe. Thus, the final document can be considered to represent the consensus view of the European CFD community.

Inevitably, the Guidelines cannot cover every aspect of CFD in detail. They are intended to offer roughly those 20% of the most important general rules of advice that cover roughly 80% of the problems likely to be encountered. As such, they constitute essential information for the novice user and provide a basis for quality management and regulation of safety submissions which rely on CFD. Experience has also shown that they can often provide useful advice for the more experienced user. The technical content is limited to single-phase, compressible and incompressible, steady and unsteady, turbulent and laminar flow with and without heat transfer. Versions which are customised to other aspects of CFD (the remaining 20% of problems) are planned for the future.

The seven principle chapters of the document address numerical, convergence and round-off errors; turbulence modelling; application uncertainties; user errors; code errors; validation and sensitivity tests for CFD models and finally examples of the BPG applied in practice. In the first six of these, each of the different sources of error and uncertainty are examined and discussed, including references to important books, articles and reviews. Following the discussion sections, short simple bullet-point statements of advice are listed which provide clear guidance and are easily understandable without elaborate mathematics. As an illustrative example, an extract dealing with the use of turbulent wall functions is given below:

- Check that the correct form of the wall function is being used to take into account the wall roughness. An equivalent roughness height and a modified multiplier in the law of the wall must be used.

- Check the upper limit on $y+$. In the case of moderate Reynolds number, where the boundary layer only extends to $y+$ of 300 to 500, there is no chance of accurately resolving the boundary layer if the first integration point is placed at a location with the value of $y+$ of 100.

- Check the lower limit of $y+$. In the commonly used applications of wall functions, the meshing should be arranged so that the values of $y+$ at all the wall-adjacent integration points is only slightly above the recommended lower limit given by the code developers, typically between 20 and 30 (the form usually assumed for the wall functions is not valid much below these values). This procedure offers the best chances to resolve the turbulent portion of the boundary layer. It should be noted that this criterion is impossible to satisfy close to separation or reattachment zones unless $y+$ is based upon $y*$.

- Exercise care when calculating the flow using different schemes or different codes with wall functions on the same mesh. Cell centred schemes have their integration points at different locations in a mesh cell than cell vertex schemes. Thus the $y+$ value associated with a wall-adjacent cell differs according to which scheme is being used on the mesh.

- Check the resolution of the boundary layer. If boundary layer effects are important, it is recommended that the resolution of the boundary layer is checked after the computation. This can be achieved by a plot of the ratio between the turbulent to the molecular viscosity, which is high inside the boundary layer. Adequate boundary layer resolution requires at least 8-10 points in the layer.

All such statements of advice are gathered together at the end of the document to provide a 'Best Practice Checklist'. The examples chapter provides detailed expositions of eight test cases each one calculated by a code vendor (viz FLUENT, AEA Technology, Computational Dynamics, NUMECA) or code developer (viz Electricité de France, CEA, British Energy) and each of which highlights one or more specific points of advice arising in the BPG. These test cases range from natural convection in a cavity through to flow in a low speed centrifugal compressor and in an internal combustion engine valve.

Copies of the Best Practice Guidelines can be acquired from:

ERCOFTAC CADO
Crown House
72 Hammersmith Road
London W14 8TH, United Kingdom

Tel: +44 (0)207 559 1429
Fax: +44 (0)207 559 1428
Email: Richard.Seoud-ieo@ercoftac.org

The price per copy (not including postage) is:

ERCOFTAC members

First copy		*Free*
Subsequent copies		45 Euros
Students		30 Euros
Non-ERCOFTAC academics		75 Euros
Non-ERCOFTAC industrial		150 Euros

Special Issue Coordinated by SIG-39 on Aeroacoustics

C. Bailly

Université de Lyon, Ecole Centrale de Lyon, LMFA - UMR CNRS 5509
Institut Universitaire de France
christophe.bailly@ec-lyon.fr, http://acoustique.ec-lyon.fr

Introduction

Aeroacoustics is one of the disciplines that has exceptionally grown since the 1990s, in agreement with the *second golden age* predicted by Lighthill[1]. This can be associated with the development of accurate time-resolution algorithms to solve the Navier-Stokes equations combined with the increase in computational resources. This is however not the only explanation of this rapid expansion. Social and environmental challenges in aeroacoustics are currently manifold.

Frontiers of aeroacoustics

The primary goal of aeroacoustics is the comprehensive understanding of aerodynamic noise, that is sound generated by turbulent flows. Turbulence is therefore the heart of the subject, involving fundamental studies from isotropic turbulence to sheared turbulent flows as jets or boundary layers. Simulations and experiments at sufficiently high Reynolds numbers are often needed to describe realistic physics, and this concern seems shared in the literature[2]. I would naturally mention at this point the work performed in our group[3], and also invite the reader to consider the contributions in this issue.

This strong link between fluid dynamics and aeroacoustics is of course not completely surprising for a subject mainly devoted to flow noise, but should be preserved and reinforced in teaching methods and in industrial organizations.

Aeroacoustics is not only the subject devoted to the investigation of aerodynamic noise, but also to its propagation in an often inhomogeneous medium, to its radiation in the far field, and moreover to means for reducing this noise, including possible active control. Note that only generation and propagation in gas are here considered, but similar physics occurs in the case of heavy fluids, as in underwater acoustics for instance, and more generally in hydroacoustics. Thermoacoustic instabilities, noise induced by wall-pressure fluctuations or modelling of boundary conditions in the framework of propagation and control are part of aeroacoustics.

Finally, aerodynamic noise should not only be associated with noise pollution or instrumental music ! Noise monitoring is used as a diagnostic tool in duct propagation or in turbomachineries. Applications in medicine, namely medical imaging or lithotripsy, are also at the frontiers of aeroacoustics.

Present issue and upcoming course

This special issue is a nice opportunity to become more familiar with some topics and research teams in aeroacoustics. The objective is not to cover all subjects or to provide reviews, but rather to highlight recent progress. I would like to acknowledge all the authors for their contribution, and also Dr. Damiano Casalino (former at Cira, Italy, and now at Exa Corporation, Germany) & Prof. Lars-Erik Eriksson (Chalmers University of Technology, Goteborg, Sweden), even if it was not possible to include their text in this bulletin.

This is finally the opportunity to mention that the SIG-39 (Special Interest Group) organizes its first school next October[4]. It will provide a comprehensive overview of recent progress in aeroacoustics theories (practical applications of Lighthills analogy and vortex sound, Goldsteins analogy, and coupling with instability waves). A number of practical problems involving the coupling between CFD results and CAA will be also thoroughly discussed (*e.g.* how to design a mesh for aeroacoustics simulations using large eddy simulation, inclusion of mean flow effects via hybrid formulations) and realistic applications performed by the instructors (aeronautics, car industry, propulsion, energy,...) will be analysed. Moreover, advanced computational aeroacoustics methods will be presented, as well as what we can learn from the direct computation of aerodynamic noise. The involved lecturers are Prof. Anurag Agarwal (University of Cambridge, UK), Prof. Christophe Bailly (Ecole Centrale de Lyon, France), Dr. Christophe Bogey, Ecole Centrale de Lyon, France), Prof. Christophe Schram (Institute von Karman, Belgium), Prof. Wolfgang Schröder (Institute of Aerodynamics, Aachen, Germany), and Dr. Gwenael Gabard (University of Southampton, UK).

References

[1] Lighthill, J., 1992, Report on the final panel discussion on computational aeroacoustics, Workshop on Computational Aeroacoustics, ICASE and NASA Langley Reseach Center, 6 - 9 April, *Icase Report 92-53.*

[2] Philipp Schlatter, P., Örlü, R., Li, Q., Brethouwer G., Johansson, A.V., Alfredsson, H. & Henningson, D.S., 2011, Progress in simulations of turbulent boundary layers, *Seventh International Symposium on Turbulence and Shear Flow Phenomena (TSFP-7).* `http://www.mech.kth.se/~pschlatt/DATA/TSFP7-Presentation.pdf`

[3] Bogey, C., Marsden, O. & Bailly, C., 2011, On the spectra of nozzle-exit velocity disturbances in initially nominally turbulent, transitional jets, *Physics of Fluids*, **23**, 091702, 1-4.

[4] Refer to Ercoftac website, `http://www.ercoftac.org/products_and_services/industry_events_for_2012/computational_aeroacoustics/`

Direct Numerical Simulations of Airfoil Self-Noise

R. D. Sandberg[1], L. E. Jones[2]

[1] *Faculty of Engineering and the Environment, University of Southampton,*
Southampton SO17 1BJ, UK, sandberg@soton.ac.uk
[2] *Faculty of Engineering and the Environment, University of Southampton,*
Southampton SO17 1BJ, UK, ljones@soton.ac.uk

Abstract

Airfoil self-noise is the noise produced by the interaction between an airfoil with its own boundary layers and wake. Self-noise is of concern as it is an important contributor to the overall noise in many applications, e.g. wind turbines, fan blades, or air frames, to name a few. This contribution aims to give an overview of recent and on-going research on airfoil noise at Southampton. The goal of this work is to better understand the exact noise source mechanisms, identify noise sources other than trailing-edge noise, study acoustic feedback loops, and to investigate methods of noise reduction. To enable an in-depth study of airfoil noise, direct numerical simulations of transitional flow over airfoils have been performed. By solving the compressible Navier–Stokes equations using high-order accuracy spatial and temporal numerical schemes, both the hydrodynamic and the acoustic field could be computed directly at the same time.

1 Introduction

When considering airfoil self-noise it is typical for studies to focus primarily on trailing-edge noise. Brooks *et al.* [1] classified five mechanisms for airfoil self-noise, for which all but one (noise generated via the wing-tip vortex) are generated by disturbance interaction with the airfoil trailing edge (TE). Turbulent fluctuations that scatter off a sharp edge of a solid body radiate more efficiently at low Mach numbers than fluctuations in free-space (M^5 c.f. M^8)[2, 3], hence trailing-edge noise is increasingly significant at low Mach numbers. For that reason, TE noise is typically one of the main noise sources, particularly at low Mach numbers, and hence the development of trailing-edge noise theories has been given much attention.

Under certain flow conditions, additional noise sources distinct from sources at the airfoil trailing edge have been observed. In two-dimensional numerical simulations, Tam and Ju [4] observed that vortices in the airfoil wake may themselves generate pressure waves, while Sandberg *et al.*[5] noticed additional noise sources on the suction surface associated with vortex shedding caused by a laminar separation bubble. Because these noise generation mechanisms are different from that occurring at the trailing-edge, classical methods that are based on surface pressure difference (e.g. Amiet's theory [6]) cannot predict the overall airfoil self-noise accurately. Therefore, some of our ongoing work is on determining the nature and significance of noise sources distinct from the TE noise mechanism.

Besides these additional noise sources, in several experimental and numerical studies discrete tones have been observed to be emitted for certain flow parameters, occurring at increased amplitudes with respect to the background broadband contribution. This phenomenon was first reported by Paterson *et al.* [7], who performed an experimental study on NACA-0012 and NACA-0018 airfoils. Several different mechanisms have been proposed for the tonal noise phenomenon: Paterson *et al.* [7] determined that the phenomenon is associated with laminar flow on the pressure side of the airfoil, and hence does not occur for sufficiently high Reynolds numbers. Tam [8] suggested that an acoustic feedback loop involving the airfoil trailing edge and an acoustic source in the airfoil wake may be responsible for the tonal noise phenomenon. Arbey and Bataille [9] found that the tonal peak in their spectra was a superposition of a broadband peak at a main frequency and a set of regularly spaced discrete frequencies. In contrast, Nash *et al.* [10] in an experimental study of a NACA-0012 airfoil geometry found only one discrete tone. The authors concluded that hydrodynamic instabilities play a major role in the tone phenomenon. In a numerical study, Desquesnes *et al.* [11] concluded that the mechanism for the dominant tone was the acoustic feedback loop proposed by Nash *et al.* [10]. Although the majority of the mechanisms involved in the tonal noise phenomenon are well documented (e.g. primary instability growth), the acoustic feedback mechanism and its role in tonal noise is less well understood. Hence, rigorously proving the presence of a feedback loop for airfoil flows exhibiting tonal noise has been one of the objectives of our studies.

Although the presence of additional noise sources or the presence of tones might be important for certain flow conditions or airfoil geometries, for most practical applications the broadband TE noise mechanism will dominate. Thus any successful airfoil self-noise reduction measures will have to address the trailing-edge noise mechanism. Previous experimental and analytical studies have shown that TE modifications can reduce airfoil self-noise without compromising aerodynamic performance. The addition of brushes to airfoil trailing edges, for example, was found to reduce the intensity of trailing-edge noise [12]. The noise reduction in that case is likely due to increased compliancy of the brushes weakening the diffraction effect at the airfoil trailing edge and alleviating the surface pressure difference.

Alternatively, TE serrations have been considered. Howe [13] performed a numerical analysis of a flat plate with TE serrations possessing sawtooth-like profiles and predicted that the intensity of TE noise radiation could be reduced by such modifications, with the magnitude of the reduction depending on the length and spanwise spacing of the teeth, and the frequency of the radiation. It was determined that longer, narrower teeth should yield a greater intensity reduction. Oerlemans *et al.* [14] investigated experimentally the effect of adding such TE

serrations to full size wind-turbine blades and found overall self-noise reductions of 2-3dB without adversely affecting aerodynamic performance. Nevertheless, the precise mechanism by which this noise reduction occurs is not yet fully understood. Understanding those mechanisms could lead to improvements in serration design, and possibly the development of alternative techniques based on similar physical principles. Our studies have therefore also aimed at numerically investigating the flow around airfoils with trailing edge modifications to identify the mechanism by which the noise reduction effect is achieved.

Direct numerical simulation (DNS) is the preferred tool for such fundamental studies due to the absence of modelling. Compressible DNS allow an accurate representation of hydrodynamic phenomena such as turbulence and transition to turbulence, and of the propagation of acoustic waves. Conducting direct noise simulations avoids interfacing between solution methods as required for hybrid approaches, and allows for the presence of acoustic feed-back loops [15]. The complex geometries associated with trailing edge modifications represent a considerable numerical challenge using high-order accuracy spatial schemes. For this reason a purposely developed immersed boundary method representing the trailing edge modification has been employed.

Governing equations

Our in-house DNS code directly solves the unsteady, compressible Navier-Stokes equations, written in nondimensional form as

$$\rho_{,t} + (\rho u_k)_{,k} = 0 , \tag{1}$$

$$(\rho u_i)_{,t} + [\rho u_i u_k + p\delta_{ik} - \tau_{ik}]_{,k} = 0 , \tag{2}$$

$$(\rho E)_{,t} + [u_k(\rho E + p) + q_k - u_i\tau_{ik}]_{,k} = 0 , \tag{3}$$

where the total energy is defined as $E = T/[\gamma(\gamma-1)M^2] + 0.5u_iu_i$. The stress tensor and the heat-flux vector are computed as

$$\tau_{ik} = \mu(u_{i,k} + u_{k,i} - 2/3u_{j,j}\delta_{ik})/Re$$
$$q_k = -\mu T_{,k}/[(\gamma-1)M^2PrRe] , \tag{4}$$

respectively, where the Prandtl number is assumed to be constant at $Pr = 0.72$, and $\gamma = 1.4$. The molecular viscosity μ is computed using Sutherland's law [16], setting the ratio of the Sutherland constant over freestream temperature to 0.36867. To close the system of equations, the pressure is obtained from the non-dimensional equation of state $p = (\rho T)/(\gamma M^2)$. The primitive variables ρ, u_i, and T have been nondimensionalized by the freestream conditions and the airfoil chord is used as the reference length scale. Dimensionless parameters Re, Pr and M are defined using free-stream (reference) flow properties.

Numerical method

The finite-difference code used for the current investigation is based on a code extensively used for compressible turbulence research, such as compressible turbulent plane channel flow [17], or turbulent flow over a flat-plate trailing-edge [18]. The underlying numerical algorithm consists of a five-point fourth-order accurate central difference scheme combined with a fourth-order accurate Carpenter boundary scheme [19] for the spatial discretization, and an explicit fourth-order accurate Runge-Kutta scheme for time-stepping. No artificial viscosity or filtering is used. Instead, stability is enhanced by appropriate treatment of the viscous terms in combination with entropy splitting of the inviscid flux terms [17]. The code was extended so that it could be applied to a C-type grid with wake connection. At the freestream boundary, where the only disturbances likely to reach the boundary will be in the form of acoustic waves, an integral characteristic boundary condition is applied [20], in addition to a sponge layer comprising a dissipation term added to the governing equations. At the downstream exit boundary, which is subject to the passage of nonlinear amplitude fluid structures, a zonal characteristic boundary condition [21] is applied for increased effectiveness. At the airfoil surface an adiabatic, no slip condition is applied. This variant of the code has been recently used for direct numerical simulations of transitional flows on full airfoil configurations [15, 22]. For simulations of airfoils with serrated and non-serrated flat-plate trailing-edge extensions an immersed boundary method (IBM), as described in Sandberg and Jones [23], was used.

All simulations conducted used a C-type domain with dimensions of 5 chord-lengths from the trailing edge to the outflow boundary, 7.3 chord-lengths from the airfoil surface to the freestream boundary, and, in three dimensional cases, a spanwise width of 0.2 chords. The influence of domain size and grid resolution have been investigated thoroughly for the flow around a NACA-0012 airfoil at $Re = 5 \times 10^4$ and $\alpha = 5°$ in Jones et al.[22]. At a chord-Reynolds number of $Re = 5 \times 10^4$, in the tangential direction, 2570 grid points were used, with 1066 and 1126 points clustered over the airfoil for the cases without and with trailing edge extensions, respectively. In the lateral direction, 692 grid points were used and for fully turbulent flows the spanwise domain was discretized with 96 points [23]. For the investigation of acoustic feedback loops, the Reynolds number was specified at $Re = 1 \times 10^5$ and the domain was discretized using 3122 tangential and 736 normal grid points [24].

Results

Acoustic feedback loop

A study by Jones et al. [15] showed that in two dimensional simulations of flow over a NACA-0012 airfoil the vortex shedding frequency was considerably lower than that of the most unstable hydrodynamic instability obtained through linear stability analysis. Using a forced Navier–Stokes simulation approach, it was also shown that the time-averaged flow fields are globally unstable due to an acoustic feedback loop, while classical linear stability theory predicted no local absolute instability. The acoustic feedback loop was shown to be composed of (A) instability waves convecting over the suction side of the airfoil, (B) an acoustic scattering at the trailing edge of the airfoil, (C) acoustic waves propagating upstream, and (D) a region of receptivity within boundary layer downstream of the leading edge, as illustrated in Figure (1). The preferred frequency of the acoustic-feedback loop is significantly lower than that of the most convectively amplified instability wave and is comparable to that of the vortex shedding observed in two dimensions. It was therefore suggested that the acoustic-feedback loop may play a role in frequency selection for the vortex shedding that occurs naturally.
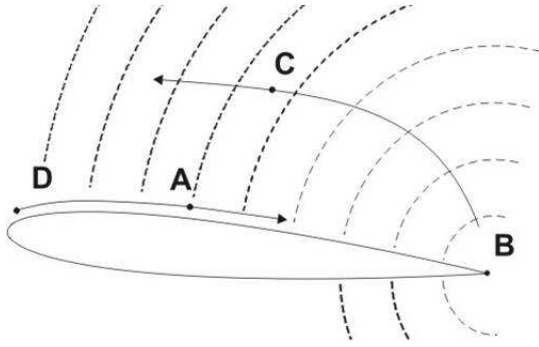
Figure 1: Schematic of acoustic feedback loop.

Figure 3: Frequency of the (∘) vortex shedding, (▽) most convectively amplified instability and (◇) acoustic feedback loop.

Figure 4: Instantaneous contours of dilatation rate and second invariant of the velocity gradient tensor $Q = 100$ for flow over NACA-0006 case at $\alpha = 7°$, $Re_C = 50,000$ and $M = 0.4$.

This hypothesis was studied in more detail in Jones and Sandberg [24]. In this study, two dimensional DNS of four airfoil flows were conducted at a chord Reynolds number of $Re_C = 100,000$ and Mach number 0.4, varying the airfoil incidence α. Figure (2) shows the instantaneous dilatation fields for two different angles of attack. In both cases tonal noise, radiating in a predominantly upstream direction and with opposite phase above and below the airfoil chord-line, can be observed. It was demonstrated that the tonal airfoil noise could be successfully predicted using Amiet's classical trailing-edge noise theory [6]. It was therefore concluded that the mechanism for noise production is mainly trailing-edge scattering.

Scrutinizing frequency spectra, at $\alpha = 0.0°$ and $\alpha = 0.5°$ a significant tonal peak was observed, caused predominantly by the passage of vortices over the airfoil trailing edge. At $\alpha = 2.0°$ it was no longer possible to identify a dominant tone. In an effort to relate the tone frequency to the frequency of hydrodynamic instabilities or an acoustic feedback loop, linear stability analysis and forced Navier–Stokes simulations were conducted. It was found that the frequency of the tone was in all cases significantly lower than the most convectively amplified instability wave. The forced Navier–Stokes analysis revealed that an acoustic feedback loop existed in all cases, although it was only unstable, i.e. lead to growing amplitudes of the initial perturbation, at $\alpha = 0.0°$ and $\alpha = 0.5°$, whereas the feedback loop was stable for $\alpha = 1.0°$ and $\alpha = 2.0°$. The frequency of the dominant acoustic tone, acoustic feedback loop and most convectively amplified instability wave are shown in Figure (3). In cases where the feedback loop is unstable, its frequency is close to that of the acoustic tone and vortex shedding behaviors. In contrast, when the feedback loop is stable, its frequency is much closer to the most convectively amplified stability wave.

From these results it was suggested that an acoustic feedback loop may act as a frequency selection mechanism and lead to the development of a discrete acoustic tone. It was also found that two key elements of the acoustic feedback loop, the boundary layer receptivity and trailing-edge scattering processes, become increasingly efficient at low frequencies. The acoustic feedback loop was therefore proposed as an explanation for why the frequency of acoustic tones observed in time-dependent DNS [15] is significantly lower than that of the most convectively amplified instability wave.

Additional noise sources

Another objective of the ongoing work is to determine the nature and significance of noise sources distinct from the TE noise mechanism. Visual inspection of Figure (4) reveals that acoustic waves originate from locations other than the trailing edge. However, rigorously pinpointing and assessing these additional noise sources turns out to be a considerable challenge. One possible method chosen by Jones *et al.* [25] is to use cross-correlations between pressure recorded in the free-stream and at the airfoil surface to identify the main noise sources.

Figure 2: Instantaneous contours of the divergence of velocity over the range $[-1 \times 10^{-1}; 1 \times 10^{-1}]$ for cases at $\alpha = 0°$ (left) and $\alpha = 2°$ (right).
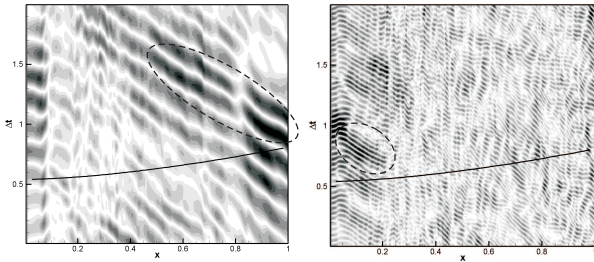
Figure 5: Cross correlation of surface pressure with pressure recorded at $(x, y) = (0.5, 1.5)$ for the flow around a NACA-0006 airfoil at $\alpha = 7°$, $Re = 5 \times 10^4$ and $M = 0.4$ for frequencies $2 < f < 6$ (left) and $9 < f < 20$ (right), showing absolute values over the range $0.06 < C_{pp} < 0.6$. The black lines represent the mean acoustic propagation time and dashed lines highlight regions discussed in the text.

The pressure at a fixed measurement location in the free-stream, denoted $p_f(t)$, and the pressure recorded at the airfoil surface as a function of x, denoted $p_s(x, t)$ were considered. Cross correlations between the two variables were computed as a function of x and the retarded time Δt as

$$C_{pp}(x, \Delta t) = \frac{S_{p_f(t+\Delta t)p_s(x,t)}}{\sigma_{p_f(t+\Delta t)}\sigma_{p_s(x,t)}}, \qquad (5)$$

where S is the covariance and σ the standard deviation. To interpret the results correctly, the time taken for an acoustic wave originating at the airfoil surface to propagate to the free-stream measurement location must be known as a function of x. This was determined by a simple acoustic ray method, whereby ray vectors were integrated as a function of local velocity and sound-speed, coupled with a secant shooting algorithm (refraction effects were neglected because variations in mean sound speed were less than 3%). Since the hydrodynamic and acoustic behaviour vary significantly with frequency, the cross-correlations were computed for finite frequency intervals. This was achieved by computing the Fourier transform of p_{free} and p_{surf}, setting the amplitude of modes outside the desired frequency range to zero, and then reconstructing a time-series by computing the reverse Fourier transform.

The cross-correlation between surface pressure and pressure recorded above the airfoil at $(x, y) = (0.5, 1.5)$ for the flow around a NACA-0006 airfoil at $Re = 5 \times 10^4$, $\alpha = 7°$ and $M = 0.4$ is plotted in Figure (5) (left) for the frequency range $2 < f < 6$. The strongest correlation is associated with downward sloping regions in the vicinity of the airfoil trailing edge, and the mean acoustic-propagation time-line intersects a region of negative correlation at the airfoil trailing edge. This feature is associated with the trailing-edge noise production mechanism, whereby the free-stream pressure correlates to downstream convecting fluctuations within the turbulent boundary layer, which ultimately generate acoustic waves as they convect over the airfoil trailing-edge. This behaviour was observed to be independent of observer location or flow conditions. In this case the upstream history of the noise production mechanism can be traced back to the transition location ($x = 0.2$), and the temporal wavelength of the correlation map near the trailing edge indicates that low frequencies correlate more strongly here. Strong correlation is also observed very near to the leading edge ($0 < x < 0.075$). This is most likely due to the passage of upstream propagating acoustic waves originating at the trailing edge. In this region,

where hydrodynamic instability waves are small in amplitude, these acoustic waves are the largest amplitude pressure disturbances present, and the temporal wavelength is similar to that observed in the vicinity of the trailing edge.

Cross correlations are plotted for the frequency range $9 < f < 20$ in Figure (5) (right). For this frequency interval the additional noise sources are expected to be the dominant source of airfoil self-noise. Firstly, it can be observed that the trailing-edge region no longer exhibits a pronounced region of maximum correlation, hence confirming that the trailing edge is not the dominant noise source in this frequency range. Instead, the most prominent region of maxima occurs in the range $0.05 < x <= 0.2$, displaced from the propagation time line by $\Delta t \approx 0.25$, and appears associated with hydrodynamic instability waves. Assuming that we are correlating to the upstream history of a hydrodynamic event that radiates noise (analogous to the trailing-edge mechanism discussed in the previous paragraph), the local convection velocity can be traced back to the propagation time-line to yield an estimate for the noise source location at $x \approx 0.33$. This lies between the time-averaged transition and reattachment locations ($x = 0.2$ and $x = 0.39$ respectively).

Consistent with our previous studies on NACA-0012 airfoils [25], the location of the additional sources cannot be isolated to a single location. The additional noise source is most likely due to large amplitude pressure fluctuations caused by the separated turbulent flow reattaching onto the airfoil surface. This reattachment is highly unsteady [22], thus the location of noise production will vary in the streamwise and spanwise directions, unlike the noise production mechanism at the airfoil trailing-edge which is fixed in space.

Trailing-edge serrations

In order to investigate the effect of trailing-edge serrations on the hydrodynamic and acoustic fields, DNS with and without trailing-edge serrations were conducted using a purposely developed immersed boundary technique. The method allows for a sharp representation of complex geometries and is described in detail and validated in Sandberg and Jones [23]. For the study on serrations, both serrated and straight flat-plate trailing-edge extensions (represented by the immersed boundary method) were added to a NACA-0012 airfoil to avoid cutting into the airfoil and producing a thick trailing edge at the serration roots, causing bluntness noise. The flow conditions were chosen as $Re = 5 \times 10^4$, $M = 0.4$, and the incidence was set to $\alpha = 5°$ because previous simulations under these conditions exhibited a slightly thinner turbulent boundary layer, and greater tendency toward tonal behavior at low frequencies [15, 22]. A thinner boundary layer means that the trailing-edge serrations do not have to be unduly large and the presence of tonal noise at low frequency allows for investigation of the effect of serrations on tonal noise components. The serration geometry is described in more detail in Jones and Sandberg [26].

In Jones and Sandberg [27] it was determined that there are no significant differences between the turbulent boundary layers for the straight and serrated trailing-edge cases that could account for observed reductions in trailing-edge noise. This implies that a reduction in TE noise must be caused either by modification to the scattering process itself, or by other hydrodynamic behaviour local to the trailing edge.
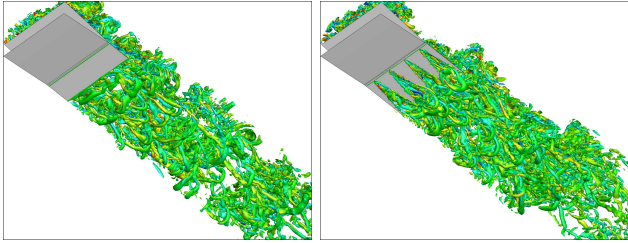
Figure 6: Iso-contours of $Q = 100$ coloured by streamwise vorticity over the range $\omega_x = \pm 100$ for the straight (left) and serrated (right) trailing-edge case.
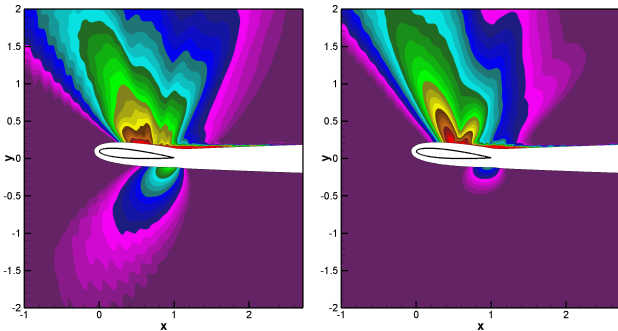
Figure 7: Logarithmically spaced contours of one-third octave averaged modulus of pressure for straight (left) and serrated (right) trailing edge; target frequency is $f = 7.75$.

Iso-surfaces of Q in the vicinity of the trailing edge (Figure (6)) are shown to qualitatively investigate the flow in the vicinity of the trailing-edge serrations. In both cases a wide range of turbulent spatial scales can be observed, including streamwise-orientated, spanwise-orientated and horseshoe-type vortices. Two main differences between the two cases, more clearly identifiable when viewing animations over a period of time, can be observed. Firstly, for the serrated trailing-edge case, the serrations appear to limit the maximum spanwise extent of turbulent structures to a spanwise dimension of one serration width. In the straight trailing-edge case this is not the case, and quasi two-dimensional structures can be observed to occur intermittently that extend for nearly the full domain width. Secondly, the presence of the serrations seems to promote the development of horseshoe-type vortices in the wake, occurring with more regularity, and originating from the serrations themselves. By looking at mean flow variables and Reynolds stress components in the vicinity of the serrations and in the initial wake it was suggested that the formation of these vortices is intensified by the presence of a mean downward (negative v) velocity through the serrations, and that an increase in airfoil incidence may lead to more regular horseshoe vortex production and/or with greater vorticity intensity [26].

To visualize how the radiated sound field is modified by trailing-edge serrations, contours of modulus of pressure are shown in Figure (7). One-third octave averaging about various target frequencies was performed to account for the broadband nature of the airfoil-noise. Here, the mid-range frequency $f = 7.75$ is shown, which corresponds to the most amplified frequency of instabilities in the laminar-turbulent transition region, and for which a trailing-edge noise reduction is expected as f exceeds the cut-on frequency of noise reduction predicted by Howe [13]. It is clearly visible that the trailing edge noise contribution is considerably weakened by the addition of TE serrations, whereas the noise originating from the suction side of the airfoil remains largely unaffected. However, for lower frequencies it was found that the addition of trailing edge serrations can considerably change the noise radiation on the suction side of the airfoil. This led to a study on whether trailing-edge serrations affect the acoustic feedback loop mechanism which is responsible for some of the lower frequency content. The study by Sandberg and Jones [23] found that the effect of serrations on the acoustic feedback loop was negligible, which they attributed to the fact that the laminar-turbulent transition is dominated by a three-dimensional instability mechanism [22] which is unaffected by the serrations.

Acknowledgments

References

[1] Brooks, T., Pope, D., and Marcolini, M., "Airfoil Self-Noise and Prediction," NASA Reference Publication 1218, NASA, 1989.

[2] Ffowcs Williams, J. and Hall, L., "Aerodynamic sound generation by turbulent flow in the vicinity of a scattering half plane," *J. Fluid Mech.*, Vol. 40, No. 4, 1970, pp. 657–670.

[3] Lighthill, M. J., "On sound generated aerodynamically I. General theory," *Proceedings of the Royal Society of London, Series A: Mathematical and Physical Science*, Vol. 211A, No. 1107, 1952, pp. 564–587.

[4] Tam, C. K. W. and Ju, H., "Numerical simulation of the generation of airfoil tones at a moderate Reynolds number," *AIAA Paper 2006–2502*, May 2006, 12th AIAA/CEAS Aeroacoustics Conference (27th AIAA Aeroacoustics Conference), Cambridge, Massachusettes.

[5] Sandberg, R. D., Jones, L. E., Sandham, N. D., and Joseph, P. F., "Direct Numerical Simulations of Tonal Noise Generated by Laminar Flow Past Airfoils," *J. Sound and Vibration*, Vol. 320, No. 4–5, March 2009, pp. 838–858, doi:10.1016/j.jsv.2008.09.003.

[6] Amiet, R., "Noise due to turbulent flow past a trailing edge," *J. Sound and Vibration*, Vol. 47, No. 3, 1976, pp. 387–393.

[7] Paterson, R. W., Vogt, P. G., Fink, M. R., and Munch, C. L., "Vortex noise of isolated airfoils," *Journal of Aircraft*, Vol. 10, No. 5, 1973, pp. 296–302.

[8] Tam, C., "Discrete tones of isolated airfoils," *The Journal of the Acoustical Society of America*, Vol. 55, 1974, pp. 1173.

[9] Arbey, H. and Bataille, J., "Noise generated by airfoil profiles placed in a uniform laminar-flow," *J. Fluid Mech.*, Vol. 134, 1983, pp. 33–47.

[10] Nash, E., Lowson, M., and McAlpine, A., "Boundary-layer instability noise on aerofoils," *J. Fluid Mech.*, Vol. 382, 1999, pp. 27–61.

[11] Desqesnes, G., Terracol, M., and Sagaut, P., "Numerical investigation of the tone noise mechanism over laminar airfoils," *J. Fluid Mech.*, Vol. 591, 2007, pp. 155–182.

[12] Herr, M. and Dobrzynski, W., "Experimental investigations in low-noise trailing-edge design," *AIAA journal*, Vol. 43, No. 6, 2005, pp. 1167–1175.

[13] Howe, M. S., "Noise produced by a sawtooth trailing edge," *The Journal of the Acoustical Society of America*, Vol. 90, 1991, pp. 482.

[14] Oerlemans, S., Fisher, M., Maeder, T., , and Kogler, K., "Reduction of Wind Turbine Noise using Optimized Airfoils and Trailing-Edge Serrations," *AIAA Paper*, Vol. 08-2819, 2008, 14th AIAA/CEAS Aeroacoustics Conference, Vancouver, May.

[15] Jones, L. E., Sandberg, R., and Sandham, N., "Stability and Receptivity Characteristics of a Laminar Separation Bubble on an Aerofoil," *J. Fluid Mech.*, Vol. 648, 2010, pp. 257–296.

[16] White, F. M., *Viscous Fluid Flow*, McGraw Hill, 1991.

[17] Sandham, N., Li, Q., and Yee, H., "Entropy Splitting for High-Order Numerical Simulation of Compressible Turbulence," *J. Comp. Phys.*, Vol. 178, 2002, pp. 307–322.

[18] Sandberg, R. D. and Sandham, N. D., "Direct Numerical Simulation of Turbulent Flow Past a Trailing Edge and the Associated Noise Generation," *J. Fluid Mech.*, Vol. 596, 2008, pp. 353–385.

[19] Carpenter, M. H., Nordström, J., and Gottlieb, D., "A Stable and Conservative Interface Treatment of Arbitrary Spatial Accuracy," *J. Comp. Phys.*, Vol. 148, No. 2, Jan. 1999, pp. 341–365.

[20] Sandhu, H. and Sandham, N. D., "Boundary conditions for spatially growing compressible shear layers," *Report QMW-EP-1100, Faculty of Engineering, Queen Mary and Westfield College, University of London*, 1994.

[21] Sandberg, R. D. and Sandham, N. D., "Nonreflecting zonal characteristic boundary condition for direct numerical simulation of aerodynamic sound," *AIAA J.*, Vol. 44, No. 2, February 2006, pp. 402–405.

[22] Jones, L. E., Sandberg, R., and Sandham, N., "Direct numerical simulations of forced and unforced separation bubbles on an airfoil at incidence," *J. Fluid Mech.*, Vol. 602, 2008, pp. 175–207.

[23] Sandberg, R. D. and Jones, L. E., "Direct numerical simulations of low Reynolds number flow over airfoils with trailing-edge serrations," *J. Sound and Vibration*, Vol. 330, No. 16, February 2011, pp. 3818–3831, doi:10.1016/j.jsv.2011.02.005.

[24] Jones, L. E. and Sandberg, R., "Numerical analysis of tonal airfoil self-noise and acoustic feedback-loops," *J. Sound and Vibration*, Vol. 330, 2011, pp. 6137–6152.

[25] Jones, L. E., Sandberg, R. D., and Sandham, N., "Investigation and prediction of transitional airfoil self-noise," *AIAA Paper*, Vol. 2009–3104, May 2009, 15th AIAA/CEAS Aeroacoustics Conference (30th AIAA Aeroacoustics Conference), Miami, Florida.

[26] Jones, L. E. and Sandberg, R. D., "Numerical Investigation of Airfoil Self-Noise Reduction by Addition of Trailing- Edge Serrations," *AIAA Paper*, Vol. 2010–3703, May 2010, 16th AIAA/CEAS Aeroacoustics Conference (31st AIAA Aeroacoustics Conference), Stockholm, Sweden.

[27] Jones, L. E. and Sandberg, R. D., "Direct numerical simulations of noise generated by the flow over an airfoil with trailing edge serrations," *AIAA Paper*, Vol. 2009–3195, May 2009, 15th AIAA/CEAS Aeroacoustics Conference (30th AIAA Aeroacoustics Conference), Miami, Florida.

Broadband Shock-associated Noise in Screeching and Non-screeching Underexpanded Supersonic Jets

B. André[1], T. Castelain[1,2] and C. Bailly[1,3]

[1] *Laboratoire de Mecanique des Fluides et d'Acoustique,*
UMR CNRS 5509 & Ecole Centrale de Lyon, 69134 Ecully Cedex, France, benoit.andre@ec-lyon.fr
[2] *University Lyon 1, 69622 Villeurbanne Cedex, France, thomas.castelain@ec-lyon.fr*
[3] *Institut Universitaire de France, Paris, France, christophe.bailly@ec-lyon.fr*

1 Introduction

A large part of the current commercial aircraft are powered by a high-bypass-ratio engine, in which a hot primary stream is embedded in a cold secondary flow. At the typical subsonic cruise speeds, the secondary jet becomes imperfectly expanded in flight, which induces a shock-cell structure inside the flow. The interaction of turbulence in the jet mixing layer with the shock-cell system is responsible for the so-called shock-associated noise component of jet noise, which adds up to the ever present turbulent mixing noise. Shock-associated noise is made up of two distinct parts : a tonal noise, referred to as screech, and a broadband one.

Screech has been extensively studied since Powell's pioneering work [1]. Powell explained with some success the generation of this tone by an acoustic feedback loop between the nozzle and an array of acoustic sources coincident with the shocks. This loop is resonant for some frequencies which are the fundamental screech frequency and its harmonics. Furthermore, this phenomenon shows a modal behaviour. A summary of the knowledge on screech is provided in Raman [2].

Broadband shock-associated noise (BBSAN) is linked with screech [3] since their generation process is basically the same. Harper-Bourne & Fisher [4] adapted Powell's stationary source array model to derive some observed properties of this noise component. Much progress on BBSAN was made around 1980 at NASA by Seiner and Norum [5], who associated advanced aerodynamical measurements, for instance of static pressure or turbulence fluctuation levels to acoustic measurements. The use of composite materials, having different noise transmission properties from classical metallic structures, in the fuselage of the next-generation aircraft, has renewed industry's interest for BBSAN. This has prompted new studies on this noise component [6, 7].

While BBSAN comes alongside screech in model laboratory jets, the latter does not seem to be observed in the practical, full-scale problem. But screech is known to have a strong impact on the jet dynamics, for instance on the shock motion [8] or on the large-scale jet motion [9]. It is already known that screech has an impact on BBSAN, explaining the effort that has long been devoted to screech suppression for BBSAN study. Nagel *et al.* [10] suppressed screech in a non-intrusive way, consisting in a large baffle mounted upstream of the nozzle exit, and observed changes on the broadband hump. A projection on the nozzle lip, or *tab*, first proposed by Harper-Bourne & Fisher [4], was extensively used. It clearly affects the shock-cell structure though and the effect on shock noise depends on the location of the tab with respect to the microphones. This arguably makes any conclusion on

Figure 1: Photograph of the notched nozzle (left) and the baseline nozzle (right).

BBSAN without screech uncertain.

The efficiency of long axial slots cut inside the nozzle wall as screech suppressing device was initially demonstrated by Norum [11]. A nozzle with shallow notches cut into the lip was used at NASA, *e.g.* by Bridges & Wernet [12], to study BBSAN specifically. It has the advantage of having a reduced deterioring effect on the jet structure. This strategy is tested in the present paper. Several experimental techniques are used to characterise the impact of the notches on the shock-cell structure and on the salient features of broadband shock-associated noise.

2 Experimental set-up

2.1 Facility and measurement techniques

The supersonic jet is unheated and exhausts into an anechoic room. The wall static pressure is measured approximately fifteen nozzle diameters upstream of the exit. The stagnation pressure is then retrieved from the static pressure value through an estimate of the local Mach number in the measurement cross section. In this paper, the operating condition will be expressed in terms of the ideally expanded jet Mach number M_j. The stagnation temperature is measured by a thermocouple probe. Two different contoured convergent nozzles are used. One is a 38.25 mm diameter nozzle with smooth lips and the other is a 38.7 mm diameter nozzle with 24 notches, or slits, of 1 mm width times 4 mm depth. The notches are cut inside a 5 mm long section of parallel walls terminating the nozzle. Both nozzles have a lip thickness of 0.5 mm. They are displayed in Figure (1) and will be referred to as *baseline* and *notched* nozzle in the following.

Far field acoustic data are obtained from thirteen 6.35 mm diameter PCB condenser microphones fixed on a circular polar antenna 2020 mm from the centre of the

(a)

(b)
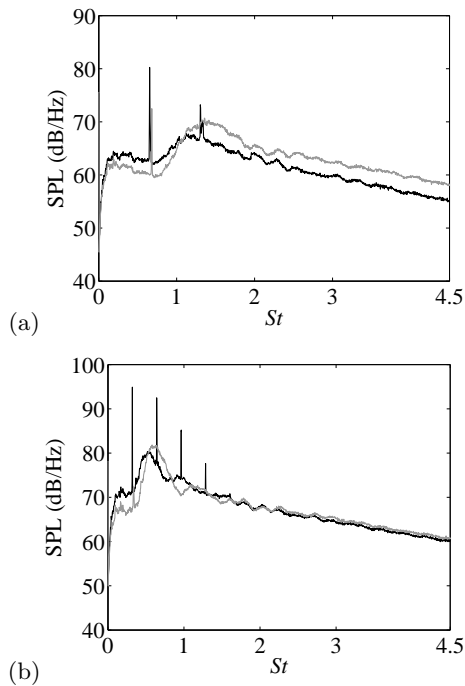
Figure 2: Far field acoustic spectra measured at a polar angle $\theta = 110°$. — baseline nozzle, — notched nozzle. (a) $M_j = 1.10$, (b) $M_j = 1.35$. SPL denotes *sound pressure level*.

nozzle. They are set every 10° from 30° to 150°. In the following, polar angles are measured from the downstream jet axis. Near field acoustic data are also acquired using four 3.175 mm diameter GRAS transducers located at a distance of the order of one jet diameter from the lipline, depending on the operating condition of the jet. The microphones are set perpendicular to the jet axis and are mounted on an axial traverse. All microphone signals are sampled at 102400 Hz by a National Instrument PXI 5733 board.

A Z-type schlieren system, mounted on an axial traverse downstream of the nozzle exit, has been used to visualize flows exhausting through both nozzles. It consists of a light-emitting diode, two f/8, 203.2 mm diameter parabolic mirrors, a knife-edge and a high-speed numerical camera.

Static pressure measurements have been performed by means of short static probes, as designed by Pinckney [13]. The diameter of the probes is 1.5 mm and the holes are located approximately 4.7 mm from the tip. Their compact geometry aims at solving the difficulty of measuring pressure in a flow with high gradients. Such probes have been extensively used for shock-cell structure characterizations, especially in connection with broadband shock-associated noise [14].

2.2 Screech reduction

Far field acoustic spectra are displayed in Figure (2) for $M_j = 1.10$ and 1.35 at a polar angle θ of 110°. They are plotted against the Strouhal number expressed as $St = fD_j/U_j$, with f the frequency, D_j the fully expanded jet diameter and U_j the perfectly expanded velocity. It is evident that the notches are very effective at $M_j = 1.35$. However, the screech reduction is smaller at $M_j = 1.10$. The same conclusions can be reached when examining other polar angles.
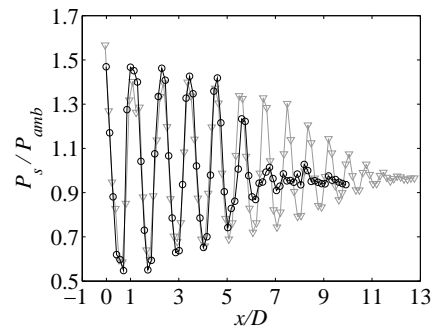
Figure 4: Centreline static pressure profiles, $M_j = 1.35$. ∘ baseline nozzle, ▽ notched nozzle. P_{amb} is the ambient pressure, x the axial coordinate and D the relevant nozzle diameter.

3 Aerodynamical effects of the notches

The influence of the nozzle indentation on the jet development, especially on the shock-cell structure, is now considered. It was recalled in the Introduction that intrusive screech-suppressing methods, such as tabs, deeply altered the shock structure. It is essential that the effect of the cancelling technique be as small as possible in order to be able to relate unambiguously any change in the broadband shock-associated noise shape to screech reduction only.

Mean schlieren pictures obtained by averaging of 500 instantaneous images sampled at 500 Hz are displayed in Figure (3) for $M_j = 1.35$. Each picture results from a collage of four partial mean images taken at different axial stations along the jet. Because of its indentation, it is not clear where the shock-cell structure actually starts in the case of the notched nozzle. To circumvent this question, the first shocks of both jets are axially aligned. The subsequent shock-cell development can then be directly compared.

The jet development is not strongly affected by the change in the nozzle lip geometry. The shock system remains axisymmetric in the case of the notched nozzle. Furthermore, the shock spacing between baseline and notched case seems to be only slightly changed. The second shock-cell is shorter with the notched nozzle, but the shock spacing then remains approximately unchanged afterward. An ejection is induced through the slits, especially visible on the vertical ones, due to the pressure ratio across them between jet and ambient. This also produces a more complex pattern in the first shock-cell.

It is evident that the shock system extends further downstream for the notched nozzle, with more shocks being visible. It is believed that screech is responsible for a quicker damping of the shock-cell structure.

Measurements of static pressure P_s have been performed on the jet centreline at $M_j = 1.35$ with both nozzles. The results, displayed in Figure (4), are in line with the schlieren visualizations : the extension of the shock-cell structure is clearly visible here. However, the strength of the first shock cells, which can be seen as the oscillation amplitude of the static pressure, is very similar for both nozzles. This quantitatively proves that the notched nozzle does not disrupt much the jet development. Finally, it has to be noted that the P_s profiles for the notched nozzle have been translated downstream by 4 mm, the slit depth, for the first shocks to be approximately aligned with their baseline counterparts.
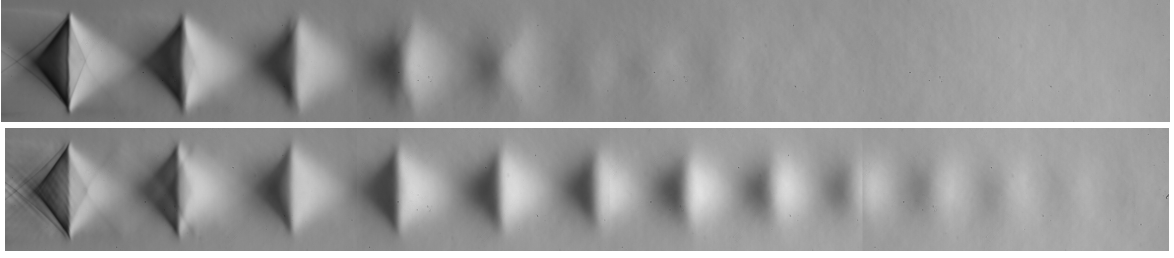
Figure 3: Schlieren visualizations with the baseline (top) and notched (bottom) nozzle, $M_j = 1.35$.

4 Screech effects on the BBSAN

It has been shown in the previous section that the notches in themselves had a small effect on the jet development. It is thus postulated in the following that the differences between broadband shock-associated noise from the two nozzles come entirely from the different screech tone levels. Some salient features are already visible in Figure (2) : the broadband hump is usually enhanced and shifted to higher frequencies. In order to quantitatively analyse the first broadband hump of the acoustic spectra in an objective way, Gaussian curves writing

$$A \exp(-(f - f_p)^2 / (2\sigma^2)) \tag{1}$$

are fitted through the spectra. In expression (Eq. (1)), A is the maximum amplitude of the hump, f the frequency, f_p the peak frequency and σ a measure of the hump width. This procedure allows an objective set of properties for each broadband hump to be obtained.

A detailed traverse of the M_j range from 1.0 to 1.55 has been performed for each nozzle and far field acoustic spectra have been measured at each operating point. For every value of M_j, the first broadband hump in the spectra at $\theta = 90°$ has been fitted by a Gaussian curve and the Strouhal number based on the peak frequency, St_p, has been plotted in Figure (5). Obviously, the peak Strouhal number is decreasing with increasing M_j, owing to the lengthening of the shock-cells. In most cases, St_p is larger for the notched nozzle as for the baseline. This property is in agreement with the baffle experiments of Norum [15]. But the most interesting feature is the tuning existing between f_p and $2 St_s$ for the baseline nozzle, where St_s is the screech Strouhal number. Whereas St_p for the notched nozzle evolves smoothly through the M_j range, it clearly follows the staging process of screech in the baseline configuration (the jump above $M_j = 1.20$ for the notched nozzle is due to a change of interpretation of a continuously evolving hump). This can be related to a modification in shock spacing due to the screech modes, which should not occur in the absence of screech. Moreover, in ranges where two screech frequencies exist in the baseline case, like around $M_j = 1.25$ and 1.40, the broadband hump seems to settle in-between the two tones. The existence of an effect of screech on BBSAN is clearly demonstrated by Figure (5).

The evolution of BBSAN the peak frequency has been estimated over all directivity angles of the far field antenna. The non-dimensional peak wavelength λ_p/D has been plotted against $\cos \theta$ in Figure (6) for $M_j = 1.10$ and 1.35.

Firstly, it is clear that f_p is higher in the case of the notched nozzle, over the entire θ and M_j range. Secondly, all the curves are approximately linear. This comes from the well-known Doppler effect arising on the far field peak frequencies of BBSAN. Harper-Bourne & Fisher [4] and Tam & Tanna [16] found the following expression for
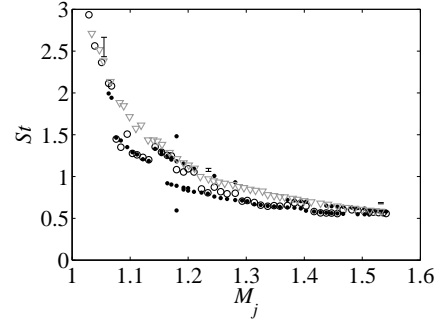
Figure 5: ○ St_p for the baseline nozzle, ▽ St_p for the notched nozzle ; ● two times the screech Strouhal number (baseline nozzle). The bars over $M_j = 1.05$, 1.24 and 1.53 denote the uncertainty ranges as estimated for the notched nozzle.

		M_j			
		1.10	**1.15**	**1.35**	**1.50**
U_c/U_j	**baseline**	0.42	0.58	0.61	0.65
	notched	0.66	0.65	0.65	0.65

Table 1: Values of U_c/U_j found from linear fitting of $f_p(\theta = 90°)/f_p(\theta)$.

f_p, with entirely different models :

$$f_p = \frac{U_c}{L(1 - M_c \cos \theta)} \tag{2}$$

In Eq. (Eq. (2)), U_c is the convection velocity of the vortical structures responsible for the shock noise, M_c is U_c divided by the ambient speed of sound and L is the shock spacing. Seiner & Yu [17] used this relation to estimate the convection velocity. Indeed,

$$f_p(\theta = 90°)/f_p(\theta) = 1 - M_c \cos \theta \tag{3}$$

The same procedure has been applied here for the two nozzles. The resulting values of U_c/U_j are displayed in Table (1). There is a striking difference between baseline and notched nozzle. While the U_c/U_j estimate for the latter is constant with M_j, the estimate for the former keeps rising. At $M_j = 1.50$, both estimates are equal owing to a weak baseline screech. The estimate at $M_j = 1.10$ for the baseline nozzle appears to be very low as compared with usual values from the literature, which could partly arise from the limited number of data points available and the shallow broadband hump over the turbulent mixing noise, making detection more subjective and peak frequencies more uncertain. Panda *et al.* [18] also found a screech mode dependency of convection velocity. When screech is removed, so is the variation of U_c/U_j as well and $U_c/U_j \approx 2/3$.

The cases $M_j = 1.10$ and $M_j = 1.35$ have also been studied in the near field. Only $M_j = 1.10$ is reported

(a)

(b)
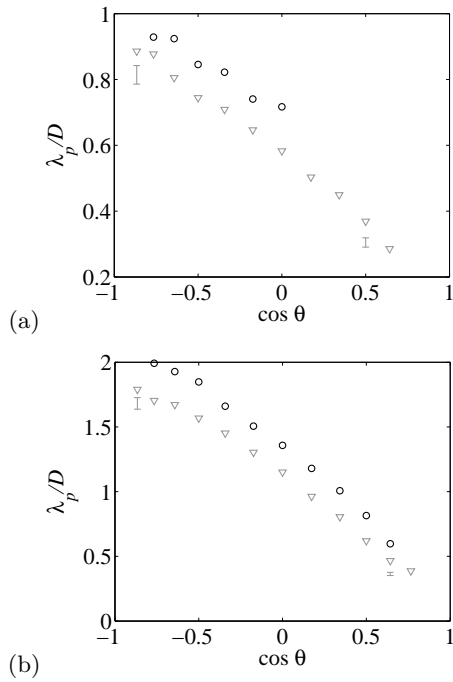
Figure 6: Evolution of non-dimensioned peak wavelength λ_p/D against $\cos\theta$. $\circ$ baseline nozzle, $\triangledown$ notched nozzle. (a) $M_j = 1.10$, (b) $M_j = 1.35$. $\cos\theta$ near one corresponds to the downstream direction. The bars denote the uncertainty ranges as estimated for the notched nozzle.

here, since similar conclusions are reached at the higher Mach number. The 3.175 mm diameter transducers are located 4.9 mm away from the lip line and are moved along the jet. Sample spectra for both nozzles are displayed in Figure (7). Near the nozzle exit, the shape of the broadband hump includes strong oscillations but the spectra are smoother further downstream. In Figure (7), it is seen that the baseline broadband hump does not emerge above the turbulent mixing noise as much as with the notched nozzle. The emergence of the hump has been simply assessed for each near field spectrum by subtracting the background sound pressure level on the left of the broadband hump to the maximum level of the hump and is shown in Figure (8). Two features stand out : (1) the emergence with weak screech is much higher than with strong screech ; (2) the BBSAN disappears in the mixing noise earlier with strong screech than with weak screech. This may be linked to the schlieren visualizations and pressure measurements shown in section 3. A strong screech was said to accelerate the damping of the shock-cell structure, so that fewer cells were visible with the baseline nozzle. As a result, the downstream shock cells are responsible for higher levels of BBSAN in the event of a weak screech than with strong screech tones, inducing higher emergence levels.

The estimation of the peak frequencies of the near field broadband humps are presented in Figure (9). A progressive shift to higher frequencies is apparent as the microphones are moved downstream. This phenomenon is in agreement with similar measurements performed by Norum & Seiner [5]. It seems that the downstream part of the shock-cell system emits shock-associated noise of higher frequency. Admitting the extension of the noise source region with weaker screech, this shift of near field f_p with downstream distance could be the reason for the observed difference in far field peak frequencies between the two nozzles. When the screech is stronger, the downstream shock cells are weakened so that the contribution
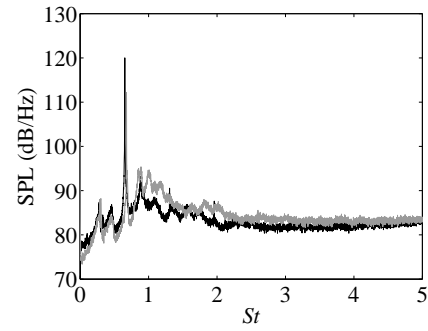
Figure 7: Near field acoustic spectra, acquired at $M_j = 1.10$, $x/D = 1.10$. —— baseline nozzle, —— notched nozzle.
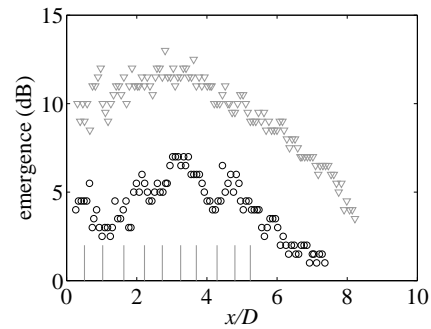
Figure 8: Emergence of broadband hump above mixing noise in the near field, $M_j = 1.10$. $\circ$ baseline nozzle, $\triangledown$ notched nozzle. The vertical lines denote the approximate locations of the first ten shocks, obtained from simultaneous schlieren visualizations of the microphones.

of these cells to the overall BBSAN levels is smaller, resulting in a reduced peak frequency of emission.

5   Concluding remarks

The effect of screech tones on broadband shock-associated noise has been experimentally studied. The screech suppression technique consists of indentations in the nozzle lip. This strategy proves effective for all fully expanded Mach numbers investigated. It has been checked on schlieren visualizations and static pressure measurements that this technique did not disrupt the shock-cell structure, which is not the case when an intrusive tab is used. Especially, the shock spacing is almost
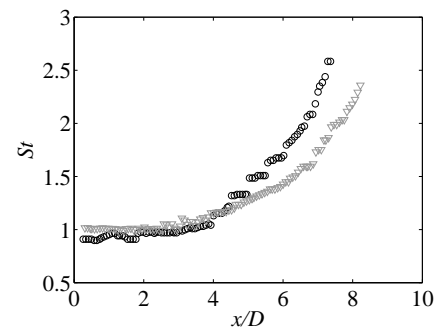
Figure 9: Peak Strouhal number of broadband shock noise in the near field, $M_j = 1.10$. $\circ$ baseline nozzle, $\triangledown$ notched nozzle.

unchanged when using the notched nozzle. An extension of the shock-cell structure has been identified, though, which leads to the conclusion that strong screech tones accelerate the damping of the shock-cell structure.

Far field acoustic measurements have shown that screech has an important effect on broadband shock-associated noise. The existence of a tuning between BB-SAN peak frequency f_p and screech frequency has been made clear from the evolution of these frequencies with M_j. The variations of f_p with directivity angle have been estimated, which has led to an assessment of the convection velocity for several Mach numbers. It has been shown that the ratio of convection velocity over jet velocity was independent on M_j, at least in the range tested, when screech was eliminated. This is in contrast with the mode related variation of U_c/U_j in screeching jets. The increase of f_p when screech is suppressed, already seen by Norum [15], has been confirmed. Near field acoustic measurements have offered an explanation for this property. Indeed, a f_p shift to higher frequencies when the near field microphones move downstream has been identified for the baseline and notched nozzles, along with an extension of the source region for BBSAN when screech is absent. The assumption here is that an excess in high frequency content is produced by the additional shock-cells existing far downstream when screech is suppressed.

More detailed aerodynamical measurements are needed to identify the modifications of the turbulence with and without screech, which has obviously a direct bearing on BBSAN. Especially, the relation between the motion of the vortical structures relatively to that of shocks and BBSAN generation could be investigated, as suggested by Seiner [19]. Indeed, screech has a possible effect on BBSAN simply because of the fact that shocks oscillate at the screech frequency in a screeching jet [8].

Particle image velocimetry will be performed for the two nozzles considered here, which should help to obtain further insight into the question.

Acknowledgements

References

[1] A. Powell, "On the mechanism of choked jet noise," *Proceedings of the Physical Society of London*, vol. 66, no. 408, pp. 1039–1056, 1953.

[2] G. Raman, "Supersonic jet screech: Half-century from powell to the present," *Journal of Sound and Vibration*, vol. 225, no. 3, pp. 543–571, 1999.

[3] C. K. W. Tam, J. M. Seiner, and J. C. Yu, "Proposed relationship between broadband shock associated noise and screech tones," *Journal of Sound and Vibration*, vol. 110, no. 2, pp. 309–321, 1986.

[4] M. Harper-Bourne and M. J. Fisher, "The noise from shock waves in supersonic jets," *AGARD CP 131*, pp. 11–1 – 11–13, 1973.

[5] T. D. Norum and J. M. Seiner, "Broadband shock noise from supersonic jets," *AIAA Journal*, vol. 20, no. 1, 1982.

[6] K. Viswanathan, M. B. Alkislar, and M. J. Czech, "Characteristics of the shock noise component of jet noise," *AIAA Journal*, vol. 48, no. 1, pp. 25–46, 2010.

[7] J. Veltin, B. J. Day, and D. K. McLaughlin, "Correlation of flowfield and acoustic field measurements in high-speed jets," *AIAA Journal*, vol. 49, no. 1, pp. 150–163, 2011.

[8] B. André, T. Castelain, and C. Bailly, "Shock-tracking procedure for studying screech-induced oscillations," *AIAA Journal*, vol. 49, no. 7, pp. 1563–1566, 2011.

[9] B. André, T. Castelain, and C. Bailly, "Experimental study of flight effects on screech in underexpanded jets," *Physics of Fluids*, vol. 23, pp. 1–14, 126102, 2011.

[10] R. T. Nagel, J. W. Denham, and A. G. Papathanasiou, "Supersonic jet screech tone cancellation," *AIAA Journal*, vol. 21, no. 11, 1983.

[11] T. D. Norum, "Screech suppression in supersonic jets," *AIAA Journal*, vol. 21, no. 2, 1983.

[12] J. E. Bridges and M. P. Wernet, "Turbulence associated with broadband shock noise in hot jets," NASA Technical Memorandum 215274, 2008.

[13] S. Z. Pinckney, "A short static-pressure probe design for supersonic flow," NASA Technical Note D - 7978, 1975.

[14] T. D. Norum and J. M. Seiner, "Measurements of mean static pressure and far field acoustics of shock containing supersonic jets," NASA Technical Memorandum 84521, 1982.

[15] T. D. Norum, "Control of jet shock associated noise by a reflector," AIAA Paper 84-2279, 1984.

[16] C. K. W. Tam and H. K. Tanna, "Shock associated noise of supersonic jets from convergent-divergent nozzles," *Journal of Sound and Vibration*, vol. 81, no. 3, pp. 337–358, 1982.

[17] J. M. Seiner and J. C. Yu, "Acoustic near field and local flow properties associated with broadband shock noise," AIAA Paper 81-1975, 1981.

[18] J. Panda, G. Raman, and K. B. M. Q. Zaman, "Underexpanded screeching jets from circular, rectangular and elliptic nozzles," AIAA Paper 97-1623, 1997.

[19] J. M. Seiner, "Advances in high speed jet aeroacoustics," AIAA Paper 84-2275, 1984.

Impact of Inhomogeneous Density Distribution on Acoustic Sources in Turbulent Jets

S. R. Koh[1], G. Geiser[1], H. Foysi[2] and W. Schröder[1]

[1] *Institute of Aerodynamics RWTH Aachen University,*

Wüllnerstraße 5a, D-52062 Aachen, Germany, s.koh@aia.rwth-aachen.de

[2] *University of Siegen, Paul-Bonatz-Straße 9-11, D-57068 Siegen, Germany*

Abstract

The noise generation of a helium-mixture and a hot-air coaxial jet is analyzed by a hybrid large-eddy simulation (LES) acoustic perturbation equations (APE) method. The coaxial jet configuration defined by a strong density gradient at the nozzle exit serves as a test problem to show the impact of the formulation of the entropy source terms on the acoustic field. To be more precise, in the APE-4 formulation a linearization of the second law of the thermodynamics is dropped and a new formulation based on the excess density is introduced. The novel source term remedies the deficit of the high-order source contribution which introduces an overestimate of low frequency acoustics.

1 Introduction

Non-uniform density distributions play an important role in the propagation of sound. The refraction of sound due to a pronounced temperature gradient is just one example. As indicated by Tester and Morfey [1] the mean density gradient partially accounts for sound amplification in subsonic jets. The sound mechanism contains additional sources in the unsteady density field, i.e., the acoustic radiation from a sheared mean flow is amplified by scattering from the mean density gradient [2]. An experimental measurement concerning the role of mass diffusion in a gas mixture [3] indicated a strong increase of acoustic damping by helium and nitrogen dioxides when the local density field was disturbed. Goldstein [4] showed that there is an exact analogy between the acoustic source in a real flow and the linear inviscid fluctuations of a quadrupole plus a temperature dipole source in an arbitrary ideal sheared mean flow. However, the identification of real sources in realistic turbulent flows is hard to achieve since the sound generation is only a small energy fraction of the entire fluid dynamic process.

It goes without saying that there exists a vast amount of literature on single-jet noise whereas just a few papers on coaxial jets have been published compared to the single-jet problem. In general, the analysis of coaxial-jet noise is based on the knowledge of single jets. In an extension of this approach the effect of multiple shear layers has been considered by Morfey and Tester [5] to correct the attenuation of sound and to discuss the scattering of sources in the shear layer. Later, more systematic analyses on heated and/or unheated primary flow configurations have been performed by considering dipole and quadrupole sources which depend differently on the turbulence intensity [6, 7]. That is, some knowledge on the impact of density gradients on the acoustics of coaxial jets is available. Recently, Koh et al. [8] showed the spectral density distributions of the entropy sources to form a cone-like surface being wrapped around the end of the potential core and the acoustic core characterized by the entropy source terms to generate low frequency dipole sound. However, the picture on the sound generation process and the importance of density gradient driven sources is by far not complete. To get further insight in the sound generation and propagation in multiple shear layer jets possessing an inhomogeneous density distribution either due to density or temperature gradients further experimental and numerical analyses are necessary. In these numerical models as little assumptions as possible should be used to have a formulation that is valid for a wide class of configuration. This problem is addressed in this contribution by introducing a formulation of the entropy related source terms that is based on the excess density.

To compute the jet acoustic field at various thermodynamic properties a hybrid large-eddy simulation/computational aeroacoustics (LES/CAA) approach is applied. That is, a two-step method using large-eddy simulation for the flow field and acoustic perturbation equations (APE) for the acoustic field is used [9]. Since a multi-species gas flow is tackled the acoustic source terms are formulated to contain the effects of mass diffusion and the thermal properties are accounted for in the local speed of sound. The source terms in the APE formulation are related to certain noise generation mechanisms and thus, it is possible to analyze the acoustic sources in great detail. Using the noise source terms of the acoustic perturbation equations for a compressible fluid the acoustic field is analyzed by considering, e.g., power spectra and overall sound pressure level distributions.

The organization of the paper is such that first, the acoustic perturbation equations and the new entropy-source formulation are presented, then the numerical approach is briefly outlined, and the results are discussed after the flow configurations are introduced.

2 Numerical method

2.1 Acoustic governing equations

The original APE-4 system [9] reads

$$\frac{\partial p'}{\partial t} + \bar{a}^2 \nabla \cdot \left(\bar{\rho} \mathbf{u}' + \bar{\mathbf{u}} \frac{p'}{\bar{a}'} \right) = -\bar{a}^2 q_c \qquad (1)$$

$$\frac{\partial \mathbf{u}'}{\partial t} + \nabla \left(\bar{\mathbf{u}} \cdot \mathbf{u}' \right) + \nabla \left(\frac{p'}{\bar{\rho}} \right) = \mathbf{q}_m , \qquad (2)$$

Table 1: Flow parameters and notation of the present jets : cjm (helium-air mixture coaxial jet), cja (hot-air coaxial jet), subscript 'p' (primary jet), subscript 's' (secondary jet), subscript '∞' (ambient air).

condition	$\rho_\infty U_s D/\mu_\infty$	U_p/U_s	U_p/a_∞	U_s/a_∞	T_p/T_s	T_s/T_∞	U_p/a_p
cjm	40000	1.1	1.0	0.9	1.0	1.0	0.6
cja	40000	1.1	1.0	0.9	2.7	1.0	0.6

where the right-hand side source terms are

$$q_c = \nabla \cdot (\rho' \mathbf{u}')' - \frac{\bar{\rho}}{c_p} \frac{\bar{D}s'}{Dt} \qquad (3)$$

$$\mathbf{q}_m = -(\boldsymbol{\omega} \times \mathbf{u})' - \left(\nabla \frac{(u')^2}{2} \right)'$$

$$+ \nabla \left(\frac{p'}{\bar{\rho}} \right) - \left(\frac{\nabla p}{\rho} \right)' . \qquad (4)$$

Note that the entropy term of the right-hand side in equation (Eq. (3)) is derived by a linearized form of the second law of thermodynamics. This approach could result in a varying impact of the entropy sources in the general acoustic field.

In non-reacting multi-species gas flows the thermal coefficients vary as a function of temperature and mass fraction. All the transport coefficients are assumed 4th-order polynomials of the temperature. Therefore, the non-uniform specific heat capacities in a mixture gas require to reformulate the noise source terms. That is, the ratio of specific heats γ in the multi-species flow is determined by $\gamma = \sum c_{p_n} Y_n / \sum c_{v n} Y_n$ where the subscript n indicates the n-th component of a mixture gas. The terms $\bar{\rho}/c_p \, \bar{D}s'/Dt$ in equation (Eq. (3)) and $T'\nabla \bar{s} - s'\nabla \overline{T}$ in equation (Eq. (4)) contain the impact of varying thermal coefficients. The mean speed of sound $\bar{a}$ is influenced by the mean mixture heat capacities $c_{p,v} = \sum (c_{p,v_n} Y_n / M_n)\mathbb{R}$.

The entropy term $T'\nabla \bar{s} - s'\nabla \overline{T}$ is related to the density-pressure relation. By using an expression for the excess density ρ_e this density-pressure relation can be rearranged. The excess density ρ_e represents the difference between the acoustic density perturbation $(\rho - \bar{\rho})$ and the acoustic perturbation at an analogous acoustic medium where the density perturbation is isentropic and the sound speed is $\bar{a}$ [10] $\rho_e = (\rho - \bar{\rho}) - (p - \bar{p})/\bar{a}^2$. That is, the perturbed density is determined by the perturbation pressure

$$\frac{\partial p'}{\partial t} - \bar{a}^2 \frac{\partial \rho'}{\partial t} = -\bar{a}^2 \frac{\partial \rho_e}{\partial t} \quad . \qquad (5)$$

In general flows, the right-hand side terms of the pressure-density relation in equation (Eq. (5)) contains non-zero terms due to irreversible production of mixing multi-species mixture.

In the present study, the original form of the entropy source term on the right-hand side of equation (Eq. (3)) is rewritten by using the excess density. The continuity equation with perturbed variables reads

$$\frac{\partial \rho'}{\partial t} + \nabla \cdot (\rho' \bar{\mathbf{u}} + \bar{\rho} \mathbf{u}') = -\nabla \cdot (\rho' \mathbf{u}')' . \qquad (6)$$

Equation (Eq. (6)) and equation (Eq. (5)) are subtracted to eliminate the time derivative of the perturbed density.

The equation of the perturbed pressure reads

$$\frac{\partial p'}{\partial t} + \bar{a}^2 \nabla \cdot (\bar{\rho} \mathbf{u}' + \rho' \bar{\mathbf{u}}) =$$

$$- \bar{a}^2 \left(\frac{\partial \rho_e}{\partial t} + \nabla \cdot (\rho' \mathbf{u}')' \right) . \qquad (7)$$

The excess density $\rho_e = \rho' - p'/\bar{a}^2$ is used to substitute ρ' on the left-hand side to obtain the same left-hand side operator as in equation (Eq. (1)). That is,

$$\nabla \cdot (\rho' \bar{\mathbf{u}}) = \nabla \cdot (\rho_e \bar{\mathbf{u}}) + \nabla \cdot \left(\frac{p'}{\bar{a}^2} \bar{\mathbf{u}} \right) \qquad (8)$$

is plugged into equation (Eq. (7))

$$\frac{\partial p'}{\partial t} + \bar{a}^2 \nabla \cdot \left(\bar{\rho} \mathbf{u}' + \bar{\mathbf{u}} \frac{p'}{\bar{a}^2} \right) =$$

$$- \bar{a}^2 \left(\frac{\partial \rho_e}{\partial t} + \nabla \cdot (\rho_e \bar{\mathbf{u}}) + \nabla \cdot (\rho' \mathbf{u}')' \right) . \qquad (9)$$

Comparison of equation (Eq. (9)) and equation (Eq. (1)) shows that q_c can be replaced by

$$q_c^* = \nabla \cdot (\rho' \mathbf{u}')' + \frac{D\rho_e}{Dt} , \qquad (10)$$

where $D\rho_e/Dt = \partial \rho_e/\partial t + \nabla \cdot (\rho_e \bar{\mathbf{u}})$ is substituted for the $-\bar{\rho}/c_p \, \bar{D}s'/Dt$ term. This entropy source expression based on the excess density was used by Bui et al. [11] in the acoustic perturbation equations for reacting flows.

To accurately resolve the acoustic wave propagation described by the acoustic perturbation equations (Eq. (1)), (Eq. (2)), (Eq. (4)), and (Eq. (10)), the seven-point stencil dispersion-relation preserving (DRP) scheme [12] is used for the spatial discretization and an alternating 5-6 stage low-dispersion and low-dissipation Runge-Kutta method for the temporal integration [13]. On the inner boundaries between the inhomogeneous and the homogeneous acoustic domain an artificial damping zone is implemented to suppress spurious sound generated on the embedded boundaries of the LES and the acoustic domain [14]. An interpolation filter is used to reconstruct the source terms on the Runge-Kutta sub-steps. An optimized filter according to Tam and Hu [15] in a one-dimensional formulation is chosen that is equivalent to a passband least-squares optimized finite impulse response (FIR) filter (cf. Oppenheim and Schafer [16]). According to Figure (1) the maximum error of the reconstructed signal is below 0.1% almost up to the design cutoff frequency chosen as $St_{D,s,\text{cutoff}} = 7$.

2.2 Flow simulation

The governing equations of the flow field are the unsteady compressible Navier-Stokes equations for non-reactive multi-species gas flows. The transport coefficients are assumed 4th-order polynomials of the temperature. The coefficients of the gas mixture are determined

via empirical mixing rules [17, 18, 19]. The numerical details to simulate the turbulent jets are described at length in the literature [8, 20, 21]. To prescribe the coaxial jet inflow a mean velocity profile using the hyperbolic tangent function. The corresponding density distribution is modeled by using the Crocco-Buseman relation and the ideal gas relation. The Reynolds number is 40000 based on the nozzle diameter ($D = 2R$) and the secondary jet velocity (U_s) at the nozzle exit. The Mach number of the secondary stream is $U_s/a_\infty = 0.9$ and the temperature ratio of the secondary flow and the ambient fluid is $T_s/T_\infty = 1.0$. Furthermore, the helium-air mixture configuration possesses a primary jet consisting of helium (30%), nitrogen (53.7%), and oxygen (16.3%) mixture to match the hot-air configuration which has a primary jet temperature $T_p \simeq 2.7T_\infty$. The flow configurations are chosen to focus on the noise sources of the hot-air and the helium-air mixture coaxial jet emphasizing the impact of the density gradient. The notation and the flow parameters of the coaxial jets are summarized in Table (1).

3   Results

In the following, results of single and coaxial turbulent jets are determined. Using the unsteady flow data over a time interval $T_s = 350R/U_s$ the time averaged statistics is obtained. First, the turbulent flow field of the helium-mixture coaxial jet is discussed by comparing the current results with findings of a helium-air coaxial jet and a hot-air coaxial jet denoted by 'cjm' and 'cja', respectively. The acoustic fields of two coaxial jets are analyzed in detail using sound spectra determined by different noise sources.

Figure (2) shows instantaneous contours of density (ρ/ρ_∞), helium gas mass fraction (Y_{He}), and local Mach number (V/a) in the $x = 0$ plane. The coaxial jet at the inflow boundary has a primary stream possessing mass fraction of 30% helium and 70% oxygen-nitrogen mixture and a secondary stream at 23.3% oxygen and 76.7% nitrogen mixture. This configuration mimics a hot coaxial jet configuration with a temperature ratio of $T_p/T_s = 2.7$ between a primary (p) and a secondary (s) jet. In this configuration low density flow develop by mass diffusion of multi-species mixture gases. The mass fraction of helium decreases rapidly at the end of the potential core
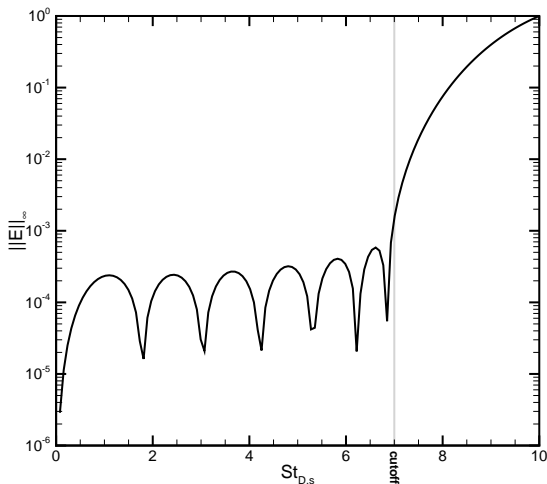
Figure 1: Infinity norm of the error induced by the interpolating FIR filter during source term reconstruction.

(a) ρ/ρ_∞

(b) Y_{He}

(c) V/a
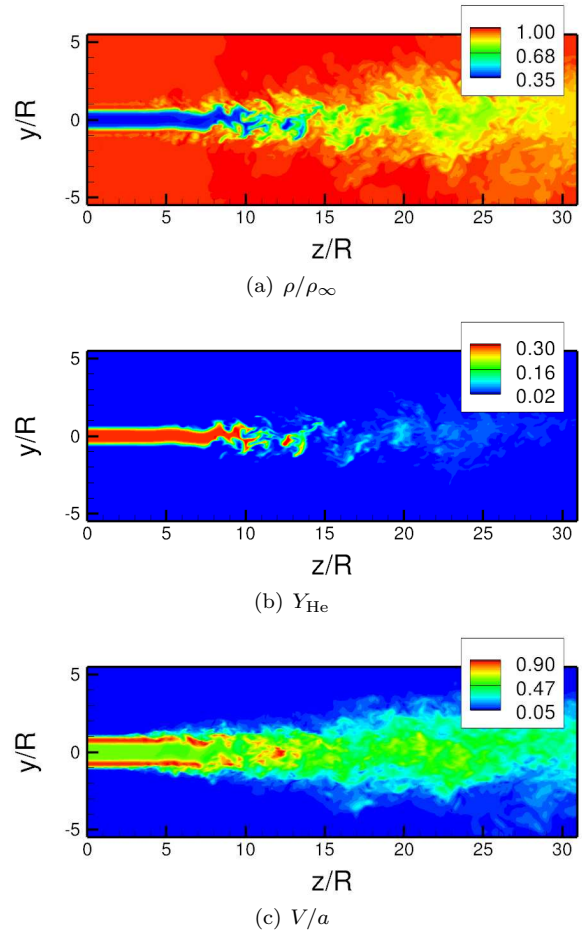
Figure 2: Instantaneous contours of a helium-mixture coaxial jet, (a) density contours, (b) helium mass fraction contours, (c) local Mach number contours defined by $V = \|\mathbf{u}\|$ and the local speed of sound a.

due to a strong turbulence production in the shear layer and a pronounced mixing. The mixing leads to an increased Mach number of the primary jet at the end of the potential core due to the greater Mach number of the secondary stream.

In Figure (3) the axial distributions of the mean centerline velocity normalized by the primary jet velocity at the nozzle exit U_p show the flow development on the jet centerline. The end of potential core (z_e) is matched to emphasize the jet development at the downstream. The helium-air and the hot-air coaxial jet are collapsed to show the rapid decrease of the axial velocity distribution compared to the single jet configurations. The multiple shear layer containing a pronounced density gradient excites the strong turbulence mixing of the coaxial jets.

The turbulence distributions on the jet centerline are presented in Figure (4) for the streamwise and the radial component. The two coaxial jets (cjm and cja) show almost likewise distributions of the turbulent shear stress. The mixing of helium-mixture fluid between the primary and the secondary jet has an equivalent impact on the turbulent fluctuations as a coaxial jet at a hot primary stream. The axial component distribution of cjm peaks at $w'/U_s \simeq 0.15$ whereas that of cja at $w'/U_s \simeq 0.14$. The mass diffusion which is described by Fick's law based on the assumption of a binary mixture seems to generate the slightly different turbulence intensity. The helium-air mixture jet shows a rapid turbulent mixing due to the strong density gradient in the shear layer. That is,
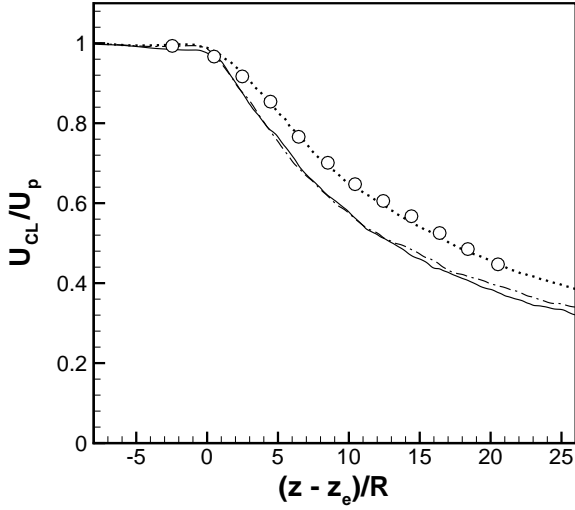
Figure 3: Axial profiles of the mean velocity on the jet centerline, —— (cjm), $- \cdot -$ (cja), $\cdots\cdots$ (single jet, LES result by Koh et al. [8]), $\bigcirc$ (single jet, experimental data by Tanna [22]).

this non-linear turbulence saturation is amplified by the strong density gradient which alters the eddy transport of two different fluids over the shear layer.

The present numerical study focuses on the analysis of the source term formulations in the original APE-4 form (equation (Eq. (3))) and the new formulation (equation (Eq. (10))). Therefore, the acoustic fields and the corresponding noise source formulations will be investigated in detail for the helium-air mixture jet to evidence the impact of the different mixing processes.

In Figure (5) the acoustic directivities at $r_p = 40R_s$ of the coaxial jet acoustics are shown. The maximum OASPL of the helium-air and the hot-air coaxial jet configuration occur at $\theta \simeq 22$ deg from the jet axis. The acoustic field of cjm is determined $2 \sim 3$dB louder than that of cja. The comparison of the turbulence intensity distribution in Figure (4) corroborates the powerful acoustic field of cjm. When the acoustic fields of the coaxial jets are determined only by the vortex sound
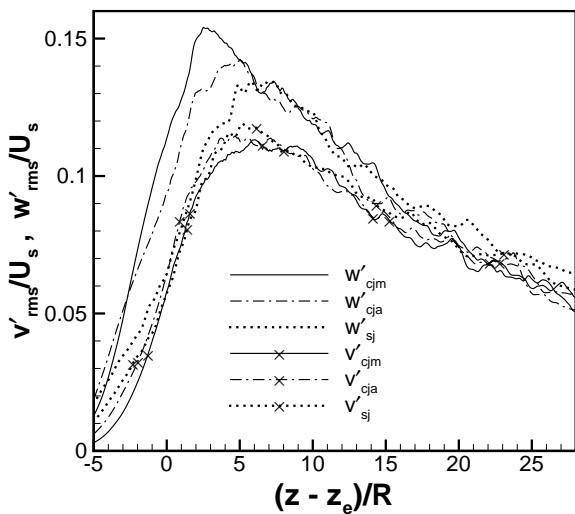
Figure 4: Axial profiles of turbulence intensity at the jet centerline, —— (cjm), $- \cdot -$ (cja), $\cdots\cdots$ (sja) [8], lines without "$\times$" (axial velocity component w'), lines with "$\times$" (radial velocity component v').
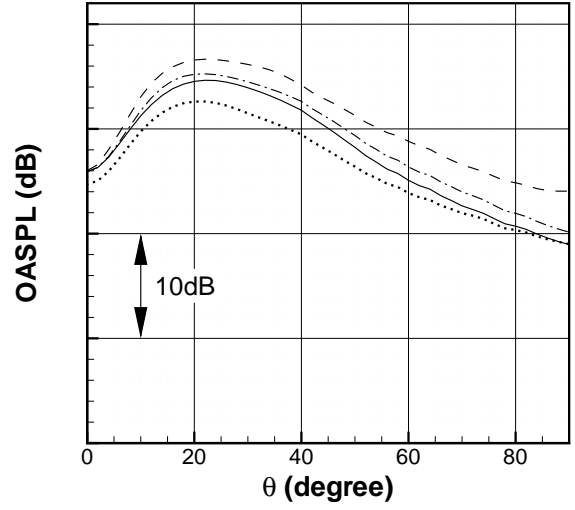
Figure 5: Overall sound pressure level for a helium-air mixture jet determined by —— (cja using eqs. (Eq. (10)) and (Eq. (4))), $- \cdot -$ (cja using eqs. (Eq. (3)) and (Eq. (4))), $- - -$ (cjm using eqs. (Eq. (10)) and (Eq. (4))), $\cdots\cdots$ (cja by Lamb vector $\mathbf{L}'$ only).

source ($\mathbf{L}' = -(\boldsymbol{\omega} \times \mathbf{u})'$) its overall sound generation does not match the acoustic directivity considering the entropy and the nonlinear source. In other words, the vortex sound source is hardly impacted by the inhomogeneous density field which generates heat content fluctuations in the hot-air and the helium-mixture coaxial jet. Over the whole directivity angle the OASPL shows a slight difference between the distribution of the old and the new entropy-source-term formulation.

Considering the distributions of the overall sound pressure level the impact of the two entropy term formulations is illustrated in Figure (6). The acoustic results based on all the noise sources of the hot-air coaxial jet include the density-pressure relation based on the excess density $D\rho_e/Dt$, which is denoted by solid lines, and the original formulation by entropy fluctuations $\bar{D}s'/Dt$, which is denoted by dash-dotted lines. The OASPL distributions with a symbol are determined by each entropy term only. From the downstream direction to the sideline the original APE formulation clearly intensifies the noise generation. The entropy source term in equation (Eq. (3)) inherently includes low-order sound sources which can easily overestimate the low frequency acoustics. That is, the expression of the original formulation clearly increases the low frequency acoustics due to the first order approximation of the second law of thermodynamics. This is indicated by the direct comparison of the ($\alpha D\rho_e/Dt$) and ($-\alpha\overline{(\rho/c_p)}\bar{D}s'/Dt$)-distributions. Especially, in the sideline direction the OASPL-values of the latter already reach the level of the total source represented by the measurements whereas the $\alpha D\rho_e/Dt$-curve possesses a much lower level.

In Figure (7) the acoustic spectra of the hot-air coaxial jet are also analyzed with respect to the effect of the formulation of the entropy source terms. The acoustics determined by the full source term formulation with the new source terms in q_c^* shows the pronounced low frequency ($St_D \simeq 0.25$) radiation at $\theta = 24$ deg. At the sideline direction rather flat sound spectra are observed. The measured acoustic power shows a ω^{-2} decay over a frequency range $0.5 < St_D < 1.5$ similar to Lilley's acoustic analogy of isotropic turbulence [23]. Over the
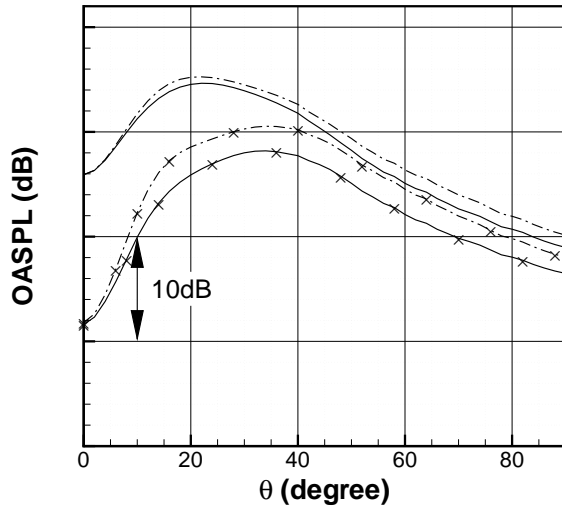
Figure 6: Overall sound pressure level determined by —— (cja using eqs. (Eq. (10)) and (Eq. (4))), − · − (cja using eqs. (Eq. (3)) and (Eq. (4))), —— with "×" (cja using eq. (Eq. (10))), − · − with "×" (cja using eq. (Eq. (3))).

Figure 7: Acoustic power spectra of acoustic pressure for a helium-air mixture jet determined by —— (cja using eqs. (Eq. (10)) and (Eq. (4))), − · − (cja using eqs. (Eq. (3)) and (Eq. (4))), —— with "×" (cja using eq. (Eq. (10))), − · − with "×" (cja using eq. (Eq. (3))), 4 black lines in the upper ($\theta = 24$ deg), 4 blue lines in the lower ($\theta = 90$ deg).

frequency of $St_D = 1.5$ the sound spectrum of the sideline direction shows a marked decrease since at the current low Reynolds number the turbulence energy decay occurs immediately in the high frequency band. The effect of the modified entropy source is clearly observed over the wide frequency band of the downstream and the sideline acoustics. Especially, in the sideline acoustics the first order approximation involved in the original formulation overestimates the low frequency acoustics. However, in the downstream direction the modification of the entropy source impacts on the high frequency noise. Acording to the recent study concerning jet noise mechanisms [24] the sound spectrum is dominated by large turbulence structures and fine-scale turbulence. The large turbulence structure dominates the jet downstream acoustics. In other words, the modified entropy source term describes with accuracy the acoustic cancellation in a high frequency band. The acoustic cancellation is involved in the convection of the large scale turbulent structures.

4 Conclusion

To understand the impact of an inhomogeneous density field on the acoustics, the flow field and the acoustic field of a helium-mixture and a hot-air coaxial jet configuration have been analyzed. The hot-air coaxial jet has an equivalent density distribution as the helium-mixture coaxial jet. The comparison of the turbulent flow fields shows almost an identical distribution of the mean velocity and the turbulence intensity. The strong density gradient in the coaxial jets enhances the turbulent mixing resulting in a strong increase of the Reynolds stress distribution near the end of the potential core. The comparison of the old and the new entropy-source formulation shows the impact of the inhomogeneous density distribution on the acoustic field determined by the hybrid LES /APE approach. The present analysis of the acoustic source terms was detailed by considering two features characterizing the sound generation in the hot-air coaxial jet. The first feature is the downstream acoustics due to the large scale turbulence at the end of the jet potential
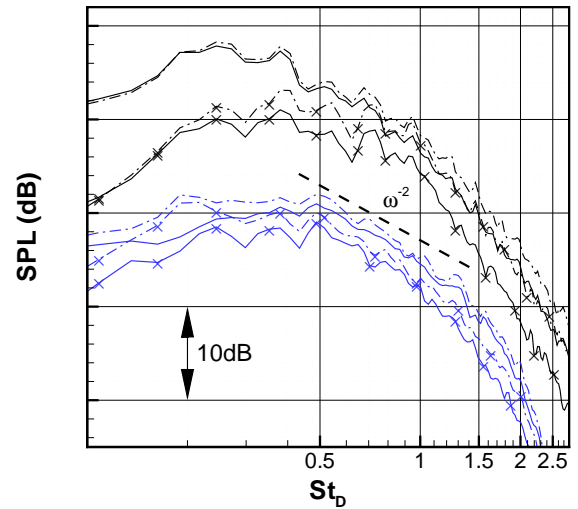
core and the second feature is the sideline acoustics the low-frequency acoustics of which was enhanced by the density gradient. Using the excess density expression the APE-4 system quantifies the detailed acoustics generated by an inhomogeneous flow field. The original noise source formulation overpredicted the acoustic radiation due to the missing contribution of small-scale turbulence. The deficit of this high-order source contribution could lead to an overestimate of the low frequency acoustics since at the low frequency band the low-order acoustics is a more efficient sound source than the high-order component. The proposed new entropy term based on the excess density does not introduce this surplus acoustics.

References

[1] Tester, B. and Morfey, C. L., "Developments in Jet Noise Modelling-Theoretical Predictions and Comparisons with Measured Data," *J. Sound Vib.*, Vol. 46, No. 1, 1976, pp.79–103.

[2] Morfey, C. L., Szewczyk, V., and Tester, B., "New Scaling Laws for Hot and Cold Jet Mixing Noise Based on a Geometric Acoustic Model," *J. Sound Vib.*, Vol. 61, No. 2, 1978, pp.255–292.

[3] Li, Y., Roberts, W., Brown, M., and Gord, J., "Acoustic Damping Rate Measurements in Binary Mixtures of Atomic Species via Transient-Grating Spectroscopy," *Exp. Fluids*, Vol. 39, 2005, pp.687–693.

[4] Goldstein, M., "An Exact form of Lilley's Equation with a Velocity Quadrupole/Temperature Dipole Source Term," *J. Fluid Mech.*, Vol. 443, 2001, pp.231–236.

[5] Morfey, C. L. and Tester, B., "Noise Measurements in a Free Jet Flight Simulation Facility : Shear Layer Refraction and Facility-to-Flight Corrections," *J. Sound Vib.*, Vol. 54, No. 1, 1977, pp.83–106.

[6] Fisher, M., Preston, G., and Bryce, W., "A Modeling of the Noise from Simple Coaxial Jets, Part I : with Unheated Primary Flow," *J. Sound Vib.*, Vol. 209, No. 3, 1998, pp.385–403.

[7] Fisher, M., Preston, G., and Mead, C., "A Modeling of the Noise from Simple Coaxial Jets, Part II : with Heated Primary Flow," *J. Sound Vib.*, Vol. 209, No. 3, 1998, pp.405–417.

[8] Koh, S. R., Schröder, W., Meinke, M., "Turbulence and Heat Excited Noise Sources in Single and Coaxial Jets," *J. Sound Vib.*, Vol. 329, No. 7, 2010, pp.786–803.

[9] Ewert, R. and Schröder, W., "Acoustic Perturbation Equations Based on Flow Decomposition via Source Filtering," *J. Comput. Phys.*, Vol. 188, 2003, pp. 365–398.

[10] Markham, J., "Second-Order Acoustic Fields: Streaming with Viscosity and Relaxation," *Phys. Rev.*, Vol. 86, 1952, pp.497–502.

[11] Bui, T. P., Schröder, W., and Meinke, M., "Numerical Analysis of the Acoustic Field of Reacting Flows via Acoustic Perturbation Equations," *Comput. Fluids*, Vol. 37, No. 9, 2008, pp.1157–1169.

[12] Tam, C. K. W. and Webb, J. C., "Dispersion-Relation-Preserving Finite Difference Schemes for Computational Acoustics," *J. Comput. Phys.*, Vol. 107, 1993, pp. 262–281.

[13] Hu, F. Q., Hussaini, M. Y., and Manthey, J. L., "Low-Dissipation and Low-Dispersion Runge-Kutta Schemes for Computational Acoustics," *J. Comput. Phys.*, Vol. 124, 1996, pp. 177–191.

[14] Schröder, W. and Ewert, R., "LES-CAA Coupling," In *Large-Eddy Simulations for Acoustics*, Cambridge University Press, 2005.

[15] Tam, C. K. W., Hu, F. Q., "An Optimized Multi-Dimensional Interpolation Scheme for Computational Aeroacoustics Applications Using Overset Grids," AIAA Paper 2004-2812, 2004.

[16] Oppenheim, A. V., Schafer, R. W., "Discrete-Time Signal Processing," Prentice-Hall, Inc., ISBN-0-13-216292-X, 1989.

[17] Wilke, C. R., "A Viscosity Equations for Gas Mixture," *J. Chem. Phys.*, Vol. 18, 1950, pp. 517–519.

[18] Bird, R. B., Stewart, W. E., and Lightfoot, E. N., "Transport Phenomena," 2nd Ed., John Wiley & Sons Inc. , 2002.

[19] Mathur, S., Tondon, P. K., and Saxena, S. C., "Thermal Conductivity of Binary, Ternary and Quarternary Mixtures of Rare Gases," *Mol. Phys.*, Vol. 12, Issue 6, 1967, pp. 569–579.

[20] Geiser, G., Koh, S. R., Schröder,W., "Analysis of Acoustic Source Terms of a Coaxial Helium/Air Jet," AIAA Paper 2011-2793, 2011.

[21] Koh, S. R., Geiser, G., Schröder,W., "Reformulation of Acoustic Entropy source Terms," AIAA Paper 2011-2927, 2011.

[22] Tanna, H. K., "An Experimental Study of Jet Noise Part I: Turbulent Mixing Noise," *J. Sound. Vib.*, Vol. 50, 1977, pp. 405–428.

[23] Lilley, G.M., "The radiated noise from isotropic turbulence with application to the theory of jet noise," *J. Sound Vib.*, Vol. 190(3), 1996, pp. 463–476.

[24] Tam, C. K. W., Viswanathan, K., Ahuja, K.K., Panda, J., "The sources of jet noise: experimental evidence," *J. Fluid Mech.*, Vol. 615, 2008, pp. 253–292.

Numerical and Experimental Characterization of Fan Noise Installation Effects

D.-C. Mincu[1] and E. Manoha[1]

[1] *ONERA–The French Aerospace Lab, F-92322, Chatillon, France*

1 Introduction

After decades of continuous reduction of the noise radiated by aeronautic powerplant systems, and especially by modern turbofans with high by-pass ratio, further improvements are now expected from engine installation effects, which means by using the airframe (fuselage, wing, empennage), or even the nacelle itself, as noise shielding surfaces through innovative engine integrations. Current acoustic studies of innovative engine installations rely on combining numerical predictions and experiments, mostly at model scale. Moreover, the development of innovative numerical methods must rely on dedicated experimental database achieved on academic configurations for validation. This was the case, for example, in the European project NACRE (New Aircraft Concepts Research in Europe, 2005-2010) where Airbus recently led studies of the RFN concept [1] (Rear Fuselage Nacelle, see Figure 1, middle) combining (i) experiments in Onera's CEPRA19 aeroacoustic open-jet wind-tunnel and (ii) several up-to-date numerical prediction methods for isolated/installed jet and fan noise from a turbofan engine. In the case of the Payload Driven Aircraft (PDA) or "flying wing" configuration [2] (Figure 1, left), also studied in NACRE (Task 3.2 "Radical Engine Integration" coordinated by Onera), radical solutions were tested with the engine installed as close as possible to the airframe, or even partly buried inside, following interests expressed by the airframer (reduced pitching moment, weight, and noise).

Although less revolutionary, the nacelle itself can be used to generate acoustic installation effects on fan noise, as it is already the case for nacelles with scarfed air inlet, a concept which is assumed to deviate the fan noise propagation in the upward direction. Within the European project OPENAIR (OPtimisation for low Environmental Noise impact AIRcraft), "scarfing" (SAF) concept is tentatively applied to the downstream nozzle of the turbofan (Figure 1, right), with the objective to decrease fan noise levels radiated towards the ground through the turbofan nozzle [3].

However, major issues can occur from these types of installations, for example (i) problems of "fatigue" structure may arise in the RFN concept, (ii) for the scarfed configuration, the thrust axis may be deviated and the mass-flow affected and (iii) for a semi-buried engine, the proximity of the airframe surface may result in a strong distortion of the intake flow and, for extreme configurations, the possible ingestion of the thick airframe boundary layer may occur. In addition, certification issues can become critical, especially for the case of engine burst event and, for this purpose, material and energy absorption analysis must be considered. The numerical prediction of engine acoustic installation effects is very complex because it requires combining (a) the simulation of the noise generation by the engine and the near field acoustic propagation of this noise

in a complex flow, and (b) the acoustic scattering on the aircraft surface and propagation up to the observer and, finally, the possible strong coupling between (a) and (b), through the retroaction of the acoustic field on the noise generation mechanisms. One possible simplification is to rely on a hybrid methodology which deliberately neglects this possible retroaction (Figure 2). The successive steps are the following.

S1. The noise generation and propagation from the isolated engine up to a near field control surface is predicted, for example by use of an accurate CAA (Computational AeroAcoustics) solver.

S2. The acoustic field collected on the control surface is used to compute an incident acoustic field (i) on the aircraft scattering surface and (ii) at the observer position, for example by use of a Kirchhoff method (note that this step is also able to provide the noise radiated by the isolated engine to the observer in farfield).

S3. The acoustic field scattered by the aircraft surface is computed by solving a Helmholtz equation (possibly accounting for the convection by a uniform mean flow) with specific surface boundary conditions, which can be done by another acoustic method, for example based on the BEM (Boundary Element Method).

S4. Finally, the total acoustic field at any observation point is the sum of the incident and the scattered fields.

For several years, Airbus, SNECMA and Onera have collaborated on the development of such hybrid methodology for the prediction of isolated/installed fan noise propagating in the aft direction [4, 5]. This collaboration
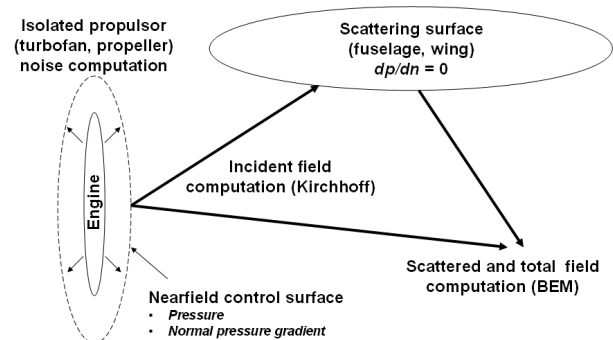
Figure 2: Simplified strategy based on a hybrid methodology for the prediction of engine noise installation effects

recently continued in the framework of the NACRE and OPENAIR programs, with the objective to validate this hybrid methodology against available fan noise experimental databases. In NACRE, the acoustical measurements were collected during the above-mentioned On-

Payload Driven Aircraft   **Rear Fuselage Nacelle**   **Scarfed aft-fan**
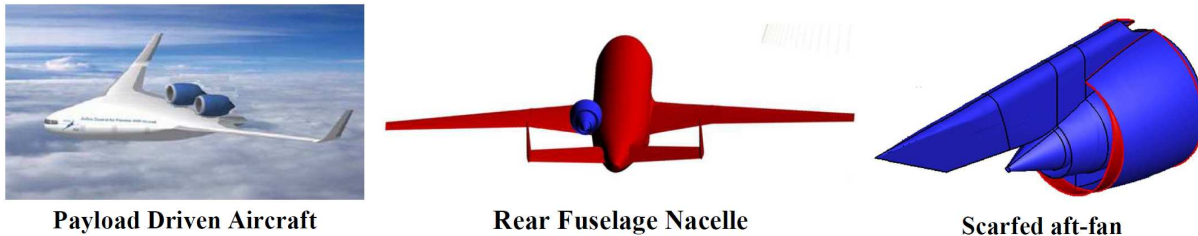
Figure 1: Configurations tested to evaluate the potential of acoustic shielding effect

era's CEPRA19 campaign, in which a turbofan nacelle equipped with a TPS (Turbine Powered Simulator) was tested in RFN configuration, with an Airbus model at scale 1/11 (Figure 3). The NACRE program ended in early 2010, but the collaboration on this approach between Airbus and Onera continued on their own funding. Regarding the OPENAIR program, an experimental campaign is planned in 2012, at QinetiQ, in the NTF open-jet acoustic wind tunnel. In this campaign, fan noise will be simulated with in-duct loudspeakers rings, instead of the TPS used in NACRE.

2 NACRE fan noise experiment

The NACRE experimental fan noise campaign was conducted in CEPRA 19 (Figure 3). Realistic interaction fan noise generation was performed by using a scaled TPS placed along the WT axis and attached to the side wall of the chamber by a symmetrical wing profile covered by acoustic absorbing foam. Real aircraft geometry (commercial single aisle Airbus aircraft model at scale 1/11) was used to account for the installation effects. The aircraft model was mounted on a trolley support allowing 3D positioning around the TPS position. This set-up was ideally designed to allow the validation of the numerical prediction of a real fan noise source with a complex scattering object. The test matrix included the survey of three TPS regimes (approach, cutback and take-off conditions), various external flow Mach numbers and relative positions of the aircraft w.r.t. the TPS. The influence of individual airframe components (wing, empennage), and also parameters such as the slat and flap settings were also evaluated.

In the present work, we will only refer to the configuration corresponding to the approach regime and the M = 0 case, either isolated or installed with the complete aircraft model with retracted slats and flaps. The characterization of the acoustic field inside the bypass duct of the nacelle was performed using an azimuthal array located just upstream the exhaust, made of 54 Kulite unsteady pressure transducers. The farfield acoustic measurements mainly relied on a circular array with a diameter of 5 m containing 48 microphones (azimuthal step 7.5°), which was circling the wind tunnel open jet, centered on the jet axis. This circular array could be moved in the axial direction over a distance of approximately one meter, providing the acoustical field along a circular cylinder. Figure 3 (right side) shows typical results obtained with the circular array of Kulite wall pressure sensors located inside the nacelle. On the upper plot, the RMS pressure at the BPF (Blade Passing Frequency) measured by the sensors show strong oscillations in the azimuthal direction, over an amplitude larger than 10 dB. These oscillations of the RMS pressure are generated by the non-axisymmetry of the by-pass duct, and especially by the bifurcation which generates azimuthal

standing waves by interaction with spinning modes. The lower plot displays a decomposition in azimuthal modes, also at the BPF, of this wall pressure field. The strongest mode (m = -8) corresponds to the fan-OGV interaction mode. Figure 4 (left side) compares the RMS pressure field measured in farfield at the BPF, for the TPS either isolated or installed with the aircraft model, measured with the circular array of diameter 5 m moved in the axial direction. On these plots, the bifurcation and the pylon of the TPS are oriented at the azimuthal angle of 180°, whereas the flyover direction, which of main interest for aircraft noise, is located at 0° (mixed dash-dot lines). Note that all measurements are projected on a sphere of radius 6 m. The plot on the right side of the figure compares the RMS pressure in the flyover direction, showing a shielding factor by the aircraft of about 10 dB.

3 Numerical methodology based on experimental measurements

a) sAbrinA-V0 solver

The initial CAA computations of the fan noise propagation through the non-uniform mean flow in the by-pass duct, is achieved with Onera's CAA parallelized solver sAbrinA-V0 [6] which solves, in the time domain, the full (non-linear) Euler equations in conservative and perturbation form using high order finite difference and spatial filtering schemes (6th order spatial derivatives and 10th order filters) and RK3 Runge-Kutta time marching scheme, on structured multiblock meshes. sAbrinA-V0 benefits from Onera's significant progress in High Power Computing provided by a parallel supercomputer SGI Altix ICE 8200 EX equipped with Intel "Nehalem-EP" quadriprocessors at 2.8 GHz, with a total of 3072 nodes.

b) BEMUSE solver

Modern numerical methods for the solution of BEM equation provide an approximation of the solution by solving a perturbed linear system where the associated matrix is easier to handle. Onera's BEM BEMUSE [7] code uses a Brakhage-Werner [8] integral formulation, an algebraic approach of the kernel approximation based on the Adaptive Cross Approximation (ACA) method initially published by Bebendorf [9] for asymptotically smooth kernel operators, and improved by Grasedyck [10]. Thanks to the algebraic approach, the ACA method can be used as a "black box", computing a low–rank approximation of appropriate matrix blocks, independent on the kernel operator. The size of the final matrix to solve, within the above considerations, is largely diminished from an N^2 to an $N \cdot \log N$ order.
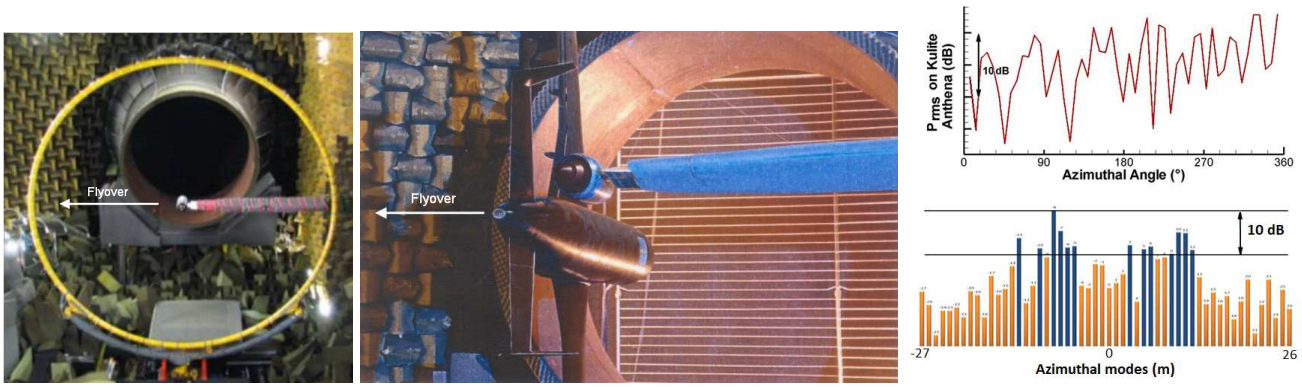
Figure 3: Views of the NACRE experiment in CEPRA 19. Left side: isolated TPS with the ϕ 5 m circular microphone array. Center: TPS in RFN configuration with the aircraft model. Right: Wall pressure fluctuations at the BPF measured by the internal array of Kulite transducers located inside the bypass duct. Upper side: RMS on each Kulite sensor. Lower side: azimuthal Fourier transform
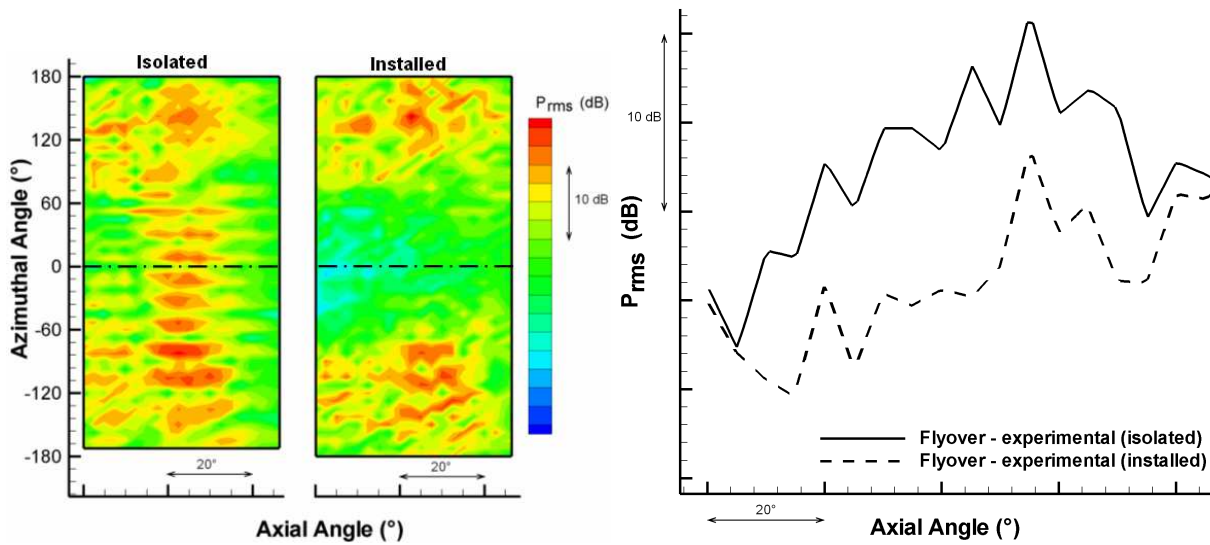
Figure 4: RMS sound field of the isolated/installed TPS, measured by the circular array of 48 microphones (diameter 5 m, extrapolated to r = 6 m). Left side: azimuthal/axial distribution. Right side: cut in the flyover direction. Note: the internal bifurcation is located at the azimuthal angle 0°/360°

c) Computational global parameters

Semi-buried engine for the Payload Driven Aircraft concept.

The main entry data are grids containing the geometries and the RANS mean flows computed by ONERA's Applied Aerodynamics Department. One of the objectives of these aerodynamic computations was to evaluate the influence of the "offset level", corresponding to the vertical distance between the fuselage level and the lowest position of the engine fan plane, divided by the fan diameter. Two different nacelle shapes (Figure 5, left) have been designed by ONERA with the offset level targets of 8 % (Shape 1) and 15 % (Shape 2). This "offset level" difference induces slight differences in the upper lip shape. For both shapes the fan plane is located at x = 1.23R (where R is the fan radius or internal nacelle radius) from the inlet lip. For both nacelle shapes 1 and 2, CAA structured multi-block grids were derived from the RANS grid with specific criteria based on homogeneous cell size depending on the acoustic wave length to be propagated. The grid is adapted to acoustic "in-flow" computations. In these cases, the considered flight Mach number is rather low (approach, M = 0.25), but the flow inside the nacelle can be much higher (up to M = 0.8

in the fan plane), so the acoustic waves in the nacelle travel against strong adverse flow with very small apparent acoustic wavelength. This leads to considerably increase the grid resolution in this region. The final grid was obtained by using Gambit and contains 4.9 millions points.

Rear Fuselage Nacelle concept

a) CAA Computation
The 3D acoustic mesh used for these computations is presented in Figure 5 (middle), showing the splitted blocks for parallel computing on 256 processors. The geometry of the aft TPS with its axisymmetrical non-homogenous mean flow was provided by Airbus. sAbrinA-V0 is used to compute the propagation of fan noise modes, through the nacelle bypass duct and the turbofan exhaust, up to a cylindrical control ("Kirchhoff") surface surrounding the engine. In order to "acoustically" take into account the three-dimensionality of the by-pass duct, an internal bifurcation was added inside the duct between the fan plane and duct exit, with the same axial extent as in the actual TPS. For simplicity sake (the mean flow remains axisymmetrical), the bifurcation was modeled as a rigid wall (Wall

Boundary Condition) with zero thickness. The final grid contains a total of approximately 10 million cells. Each computation was performed on 256 processors, the steady state being reached after 60 acoustical periods in about 10 CPU hours.

b) BEM Computation

The final objective is to use Onera's BEM solver BE-MUSE to compute acoustic installation effects from the acoustic fields collected on the Kirchhoff surface. The position of the control surface is critical. It must be close enough to the nozzle so that the grid stretching in the radial direction does not induce significant numerical dissipation, but not too close in order to avoid mean flow gradients on the surface. This optimal position was generated with the mesh generator GAMBIT and the acoustic field for each computation was simply interpolated using the graphic solver TECPLOT. The radiation surface was discretised, within classical BEM constraints (6 p.p.w.), with an unstructured grid of about 135000 points. The objective of this work is to simulate the acoustic installation effects of the TPS in the presence of the aircraft model. Figure 5 (top, centre) shows the configuration which is targeted to investigate this problem. The complete aircraft geometry is drawn in green, and the control ("Kirchhoff") surface which is used to compute the incident field is in grey color (corresponding to the black line in the CFD respective plot). Considering the TPS aft fan noise directivity, with a main lobe directed in the downstream direction, and with a view to considerably lighten the BEM computation, only the rear part of the aircraft (in green/red color on Figure 5, top center) will be considered in the simulations of installation effects (note that this part contains about 25% of the elements of the entire aircraft, about 118 000 points).

Scarfed aft-fan

The acoustical grid of the reference case for the CAA computation was designed by scaling the one described in reference [11] and modifying it to propagate all cut-on helicoidal modes in the outer field with at least 16 ppw (points per wavelength). The aerodynamic optimization process of the scarfed nacelle geometry was performed by SNECMA and the final configuration was proposed for the acoustical numerical computation. The scarfing of the nozzle was realized by distorting the reference CAA grid into the prescribed shape, keeping the same grid topology. The final CAA computational mesh is composed of about 24 million cells. The RANS stationary mean flow (Figure 3, right, bottom) for both configurations was also performed by SNECMA (using Onera's Navier-Stokes code elsA) using the same inflow conditions as for the reference case. As it was expected, preserving the mass flow rate through a smaller section involves flow acceleration in the axial direction, as it can be observed in Figure 5 (right, bottom) where the longitudinal velocity component is presented in the symmetry plane. One interesting point is that the flow is highly accelerated in the engine axis vicinity and in the downstream part of the pylon there where the acoustical waves generated by the fan are less energetical.

d) Fan noise sources

In an infinite annular duct with uniform flow, any acoustic field can be decomposed as a sum of rotating mode patterns with circumferential and radial (order m and n) pressure distributions, which are the elementary solutions of the convected Helmholtz equation with rigid

wall boundary conditions. For real wave numbers the modes are "cut-on", which means that they propagate in the upstream and/or the downstream directions. Fan noise is generated by rotating forces on blades and periodic load fluctuations due to (i) the wake interaction between the fan rotor and stator and (ii) the interaction of the fan with the ingested non-uniform mean flow. In sAbrinA-v0, the modes are injected, in terms of usual boundary condition (BC), by imposing the downstream analytical solution in fictitious cells at each time step, and taking into account the phase dependency. For the PDA concept, the acoustical cut–on modes in the fan plane were prescribed by MTU at the first harmonic of the BPF corresponding to the normalized frequency $kR = 2\pi fR/c = 22.30$. A total number of 16 modes were injected, representing the rotor/stator interaction [12] with m = k'V-hB (k'=...-2, -1, 0, 1, 2...) and the inflow distortion / rotor interaction. The objective of this study was to compare the acoustical noise emitted in the upward direction by both configurations (Shape 1 & 2) using a limited number of simulations. According to the computing capacities at that time, a "coherent broadband" source was used, meaning that all considered cut-on modes were accounted together in a coherent way, with amplitudes prescribed by MTU (Figure 6, left). Lately, within the RFN program, this assumption was revisited. The acoustic radiation resulted from the un-correlated sum of "cut-on" modes, and the Kulite circular array was assumed to provide a good approximation of this modal distribution. From the experimental mode detection shown on Figure 2, we only retained 13 azimuthal modes within a dynamics (or level range) of 10 dB below the maximum (in blue on Figure 3), each contributing with one or two "cut-on" radial modes (n = 1 and n = 2). Finally, 23 different computations were performed for individual modes with arbitrary amplitude of unity. Then, for each mode, a Kirchhoff integral method was used to derive the farfield noise from the control ("Kirchhoff") double layer surface with a section as indicated in black line in Figure 5. The experimental in-duct detection does not provide any information on the relative power of two different radial modes having the same azimuthal order, as it was the case with the MTU prescriptions. For this reason, in the final summation, the amplitude of the (m, 1) and (m, 2) modes were arbitrarily adjusted to have the same acoustic power. In the process of summing the contributions of all 23 modes, each injected mode distributes its own energy to many other azimuthal (and probably radial) modes, due to the presence of the bifurcation. In order to solve this amplitude problem, the assumption of acoustic linearity was considered. The modal detection process was applied to the acoustic field radiated by all 23 individual modes, and these results contribute to build a matrix problem which is used to find the source modal distribution (again, assuming that radial modes n = 1 and n = 2 have identical power) generating the experimental modal detection. These amplitudes were finally used to combine all modes and obtain estimations of the acoustic near field and farfield. The results in near field are presented on Figure 6 (center), in the form of the distribution of the RMS pressure at the positions of the Kulite sensors, compared to corresponding experimental data. The raw data (in thin lines) show that there is a fair qualitative and quantitative agreement between the simulation and the measurement, although the amplitude of the oscillations is slightly larger for the measurement. The same results are shown after applying a sliding average (thick lines), showing a good agreement (maximum
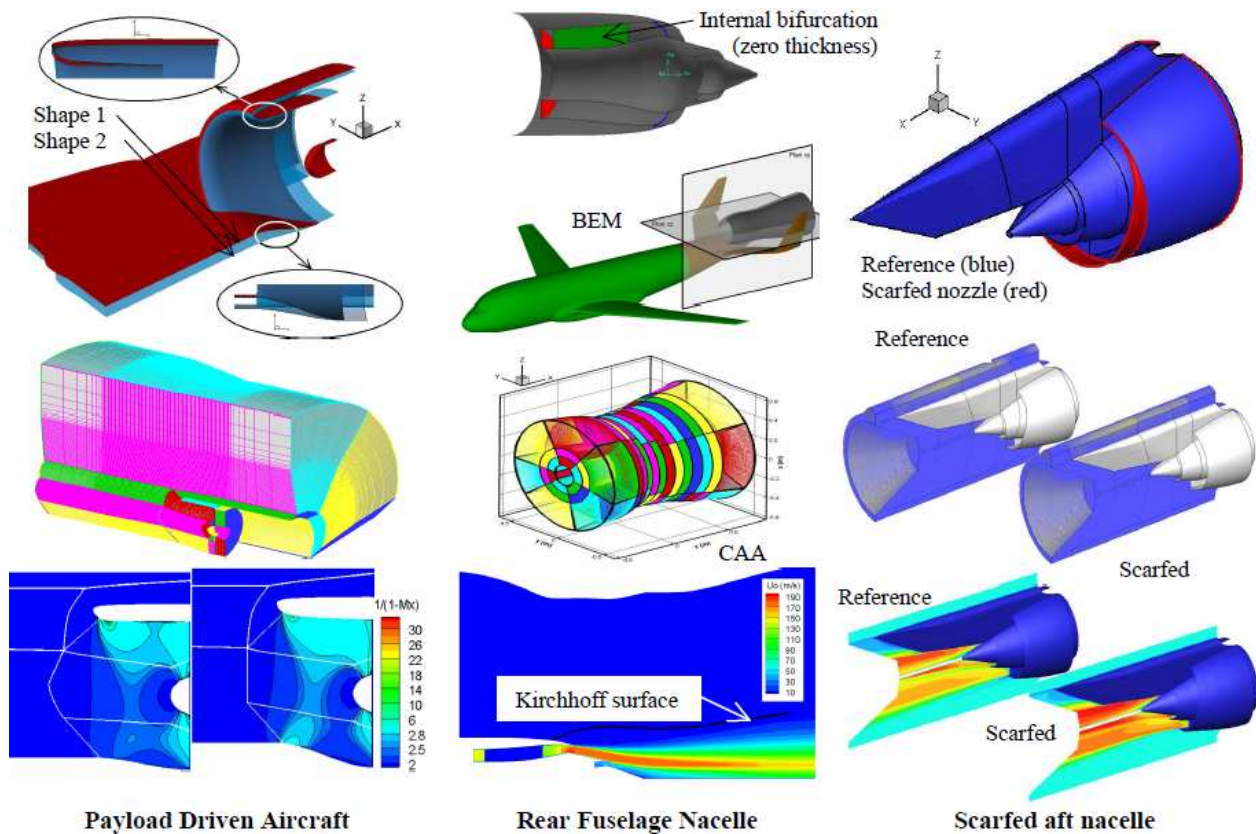
Figure 5: From top to bottom: (1) geometries, (2) acoustical grids and (3) mean flows used in the CAA computations.

difference inferior to 4 dB) between the numerical fitting and the experimental measurements.

The approach used to simulate the source in the RFN configuration was possible because the acoustical modal content was well known and the number and the acoustical properties of modes were available. When experimental data on the in-duct modal content do not exist, which is the case in the scarfed nozzle configuration studied in OPENAIR, all cut-on modes have to be considered, generally with amplitudes scaled with the assumption of evenly distributed acoustic power. This approach is often denoted as "broadband sum", although the context remains in the "tonal noise", at frequencies harmonics of the BPF. Using this approach involves an important number of numerical simulations. In the other hand, if all modes are injected simultaneously (coherent sum), strong interactions will occur between modes and the final solution may not be representative of the physics. In this context, the RPMI (Random Phase Multi-modal Injection) method was developed [13, 15] to associate a random phase to each duct mode, and to launch a limited number of independent simulations, or "RPMI events", much inferior to the original number "n" of modes, preserving the non-interaction effects. Finally, a hundred of azimuthal/radial cut-on modes are injected simultaneously, their amplitude being set to obtain the same acoustic power for each mode. Using this RPMI technique, only 10 different simulations were needed to achieve duct convergence.

4   Results

1. Payload Driven Aircraft concept
For the "coherent broadband" case (Figure 7, left), there is an integration (or averaging) of the effects by all superimposed modes and the level difference between both

shapes is less pronounced, although in favour of Shape 2. For this case, it is interesting to notice that, whatever the nacelle shape, either n°1 or n°2, the radiated noise field is not symmetrical with respect to the nacelle median plane (y = 0). On these figures, we compare iso-contours of the RMS pressure, in horizontal and vertical planes. This very different acoustic behaviour for Shape 1 and Shape 2 is not easily explained. It makes sense that, in the case of Shape 2, the steeper slope at the lower part of the nacelle increases the proportion of acoustic energy which is reflected back, to the inward direction. These reflected waves should combine with the incident waves and produce some weak "standing waves", and a close examination of the RMS field inside the nacelles actually shows slight oscillations which are more pronounced for Shape 2 than for Shape 1. However, those reflected waves are rapidly convected downstream and should fully reflect on the fan plane, where the acoustic mode is injected (a surface which acts as a rigid boundary for the waves coming from the inside of the computational domain). One last unknown point is how much acoustic energy can be dissipated through the acoustic propagation in strong mean flow gradients.

2. Rear Fuselage Nacelle concept
In this part, installation effects have been computed with BEMUSE for all individual modes, from their own surface pressure fields individually computed with sAbrinA-V0 on the control surface. Then, the total (scattered + direct) acoustic field was computed as an uncorrelated sum of all modes contributions. The results are presented on Figure 7 (center). On the left side (lower part), we compare the experimental result to the numerical result obtained with BEMUSE. On a qualitative point of view, the comparison is satisfying, especially with a shadow zone which is shifted towards
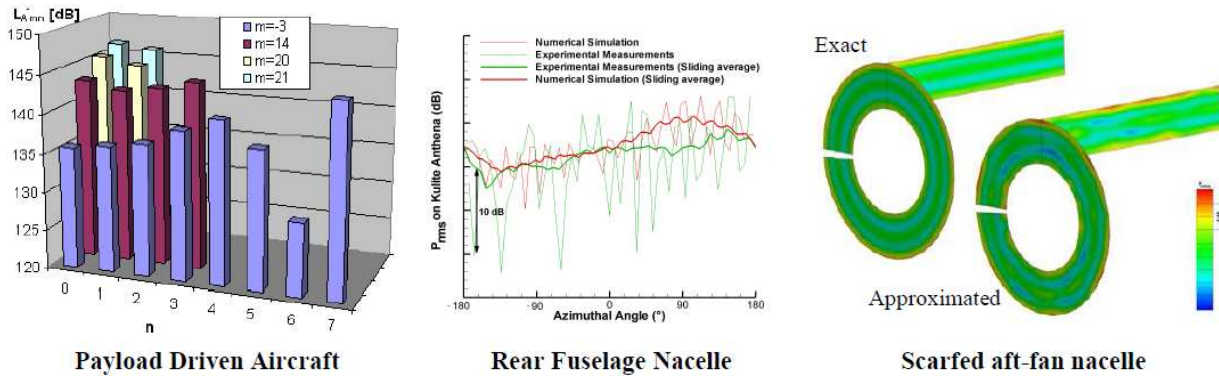
Figure 6: Modal content injected in the CAA computations. From left to right: PDA (MTU predictions); RFN (reconstructed amplitudes on Kulite positions), SAF (RPMI technique)
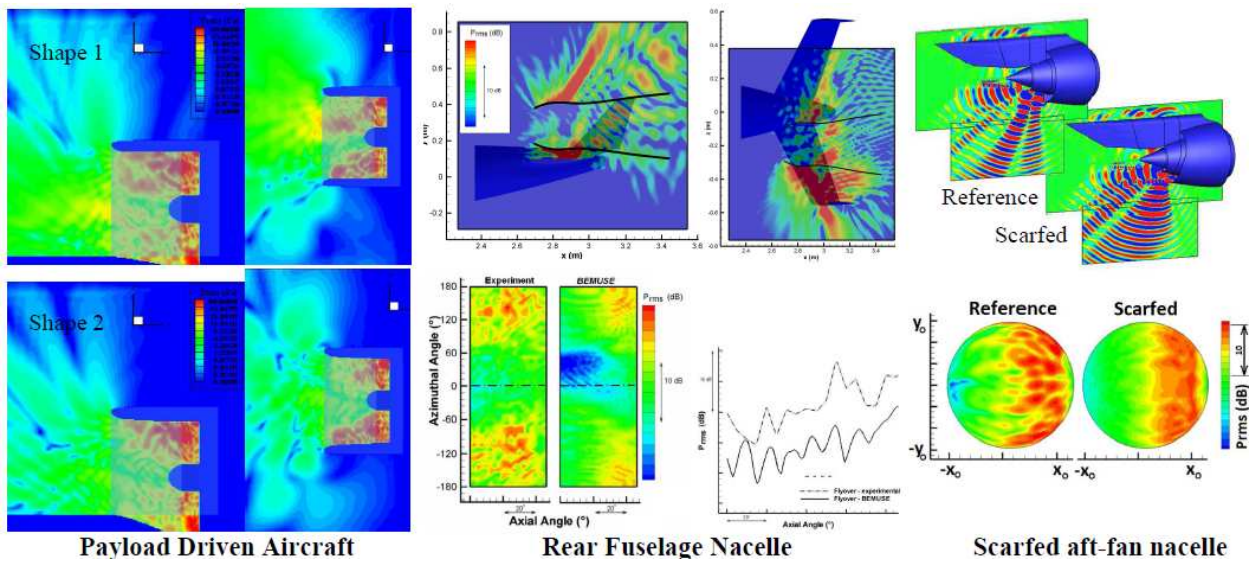
Figure 7: Acoustical results for global evaluation of shielding effects. PDA: transversal and lateral RMS pressure distribution. RFN: noise scattered by the rear empennage (up), RMS pressure comparisons between measurements and numeric (down). SAF: instantaneous view of pressure fluctuations (up), far field directivity (down).

the positive azimuthal angles due to the relative engine aircraft position. However, a detailed comparison of the levels, either observed or computed, in the flyover direction (right side plot) shows that the computation underestimates the experimental level by 7-8 dB. Two points are still very encouraging. It may be observed that the same modulation is preserved between the simulation and the experiments, and also the same slope of directivity. Within these considerations, the engine can be now moved in its axial direction to find the optimum position. In the future, the differences between the prediction and the measurement for this axial position, may be reduced by increasing the amount of cut-on modes, limited in this simulation, and propagating them over a more realistic internal mean flow (the bifurcation thickness in not taken into account in the CFD). The recent implementation of the mean flow in the BEM solver now allows taking into account some flow gradients. Finally, a supplementary effect could be added by also taking into account the inlet fan propagation as shown in [15].

3. Scarfed aft-fan concept
The instantaneous view of nearfield pressure fluctuations (Figure 7, right, up) shows the acoustic pattern but does not provide a global evaluation in the far field domain.

To overcome this problem, a semi-spherical observation surface was placed at a distance of about 400 R from the centre of the fan exhaust plane. The farfield results were averaged in un-correlated way between the 10 simulated RPMI events.

In Figure 7 (right, down), the angular extension of the observation surface around the engine is represented. On this visualization, it is clear that the scarfed nozzle globally radiates lower levels. In order to quantify this overall noise reduction, an azimuthal integration of the RMS pressure levels on the semi-spherical surface was computed, showing that for almost all axial angular positions the attenuation is of between 1 and 3 dB.

5 Conclusions

Based on three concepts of future innovative aircraft, the present work gives insights on today's possibilities to numerically investigate the potential of installation effects for aircraft noise reduction. Most of the presented acoustical tools have now reached some maturity, and they may be successfully used for industrial cases. For all three studied configurations, the shielding effects obtained by different rigid surfaces may be considered as effective (of course with possible consequences on other aircraft performances). For example, in the

case of the scarfed nozzle an almost invisible extension of the lower nacelle may induce significant noise reduction. In all numerical simulations, one critical point is the description of the noise sources, an issue which is particularly addressed in this study, mainly based on assumptions driven by experimental data. Comparisons with analytical solutions or simplified configurations also allowed isolating and understanding phenomena (see references [1, 2, 3]). In the case of the RFN configuration, the proposed hybrid methodology is particularly adapted to parametric studies of the installation effects, especially the relative position of the engine and the aircraft. For that purpose, the NACRE fan noise experimental database remains a valuable tool for further validations of numerical codes and methods. This will be also the case in OPENAIR, where specific measurements will be devoted to the investigation of installation effects.

Acknowledgments

References

[1] Mincu D.C., E. Manoha, C. Parzani, J. Chappuis, S. Redonnet, R. Davy and M. Ecsouflaire, Numerical and experimental characterization of aft - fan noise for isolated and installed configurations, *AIAA-2010-3918*, 16th AIAA/CEAS Aeroacoustics Conference, Stockholm, Sweden, June 2010.

[2] Manoha E., Mincu D.C., Numerical simulation of the fan noise radiated through a semi-buried air inlet, *AIAA Paper AIAA-2009-3293*, AIAA/CEAS Aeroacoustics Conference, Miami, June, 2009.

[3] Mincu D.C., E. Manoha, G. Reboul, S. Redonnet, S. Pascal, Numerical Simulation of Broadband Aft Fan Noise Radiation for Turbofan with Scarfed Nozzle, *AIAA-2011-2941*, 17th AIAA/CEAS Aeroacoustics Conference, Portland, USA, June 2011.

[4] Redonnet S., Desquesnes G., Manoha E., Numerical Study of Acoustic Installation Effects through a Chimera CAA Method, *AIAA-Paper* 2007-3501, 13th AIAA/CEAS Aeroacoustics Conference, 21 - 23 May 2007 Roma (Italy)

[5] C. Polacsek, S. Burguburu, S. Redonnet and M. Terracol, Numerical Simulations of Fan Interaction Noise using a Hybrid Approach, *AIAA Journal*, Vol. 44, $n°6$, June 2006.

[6] Redonnet S., Manoha E. and Sagaut P. "Numerical Simulation of Propagation of Small Perturbations interacting with Flows and Solid Bodies", *AIAA Paper*, 2001-2223, 7th CEAS/AIAA Aeroacoustics Conference, Maastricht, The Netherlands, 28-30 May, 2001.

[7] Juvigny, X., "A Fast Algebraic Boundary Integral Solver", *Eccomas Paper*, Venise, 1998.

[8] Rokhlin, V.,"Rapid solution of integral equations of classical potential theory". *Journal of Computational Physics*, 60, 187–207, (1985)

[9] Bebendorf, M.,"Approximation of boundary element matrices", *Numer. Math.* 86, 565-589 (2000)

[10] Grasedyck, L.,"Adaptive Recompression of H-matrix for BEM", *Technical Report 17*, Max-Planck- Institut fur Mathematik in den Naturwissenschaften, Leipzig (2004)

[11] S. Redonnet, D.-C. Mincu and E. Manoha, Computational AeroAcoustics of Realistic Co-Axial Engines, *AIAA Paper* 2008-2826, 14th AIAA/CEAS Aeroacoustics Conference, Vancouver, Canada, May 2008.

[12] Tyler J.M. and Sofrin T.G., "Axial Flow Compressor Noise Studies", *Trans. SAE, $n°$* 70, pp. 309-332, 1962.

[13] Polacsek C., Desquesnes G., Reboul G., "An Equivalent-Source Model for Simulating Noise Generation in Turbofan Engines", *J. Sound Vib.*, Vol. 323, Issues 3-5, pp 697-717 (2009).

[14] G. Reboul and C. Polacsek, "Towards Numerical Simulation of Fan Broadband Noise Aft Radiation from Aero-engines", *AIAA Journal*, 2010, Vol. 48, no. 9, pp. 2038–2048.

[15] Polacsek, C., Barrier, R., "Numerical simulation of counter-rotating fan aeroacoustics", 13th AIAA/CEAS Aeroacoustics Conference, Rome (Italie), 21-23 mai 2007.

Simulations of Airfoil Noise with the Discontinuous Galerkin Solver NoisSol

A. Birkefeld and C.D. Munz

Institute of Aerodynamics and Gas Dynamics, University of Stuttgart, Germany,
Birkefeld@iag.uni-stuttgart.de

1 Introduction

The most simulation tools for noise generation and propagation are based on hybrid approaches. The noise generation within a fluid flow is extracted from the flow field data as source terms for a noise propagation solver. This is favourable due to the fact, that fluid flow and noise propagation have different scales and different properties. The hybrid approach enables the use of different computational domains and different numerical schemes. Noise propagation is considered in larger domains on necessarily coarser grids with a need for efficient high order numerical methods with low dispersion and dissipation. The numerical schemes for flow simulation need robustness to also capture under-resolved problems and differ from those used in computational acoustics. Within the hybrid approach the noise propagation is usually based on linear wave propagation model, in an acoustic analogy the simple wave equation or in the perturbation approach the linearized Euler equations.

For the numerical solution of noise propagation high order finite difference schemes are often used. Based on structured or block-structured grids their extension to realistic complex geometries is cumbersome. Hence, discontinuous Galerkin schemes became interesting for the computational aeroacoustic community, because these schemes combine high precision, low dispersion and dissipation and a low sensitivity to grid quality on unstructured grids. For the simulation of noise propagation in a highly inhomogeneous mean flow on coarse grids we reported in [9] some problems with the discontinuous Galerkin scheme. Here, the use of a background flow velocity being constant in the big grid cells generate instabilities due to the jumps at the grid cell interfaces. These problems, that resulted from a poor representation of the mean flow properties motivated fundamental modifications to our aeroacoustic solver NoisSol, which will be described in the following. These modifications improved strongly its operability which will be shown by simulation results for airfoil noise simulation in the second part of this paper.

2 Building blocks of the scheme

The acoustic propagation code NoisSol, that will be described here, applies a discontinuous Galerkin scheme of arbitrary high order of accuracy on triangular and tetrahedral grids for the space discretization. For simplicity we restrict ourselves to two space dimensions.

2.1 The basic idea of discontinuous galerkin schemes

As an initial point to the following sections a short explanation of the DG scheme will be given here. This will be done with a general form of a linear system of acoustic equations $\mathbf{u}_t + \underline{\underline{A}}\,\mathbf{u}_x + \underline{\underline{B}}\,\mathbf{u}_y = 0$, e.g. the linearized Euler equations. In the context of a discontinuous Galerkin scheme the equation has to be fulfilled in a weighted integral formulation:

$$\int_Q \frac{\partial \mathbf{u}}{\partial t}\,\Phi_k\,dV = -\int_Q \left(\underline{\underline{A}}\,\frac{\partial \mathbf{u}}{\partial x} + \underline{\underline{B}}\,\frac{\partial \mathbf{u}}{\partial y} \right)\,\Phi_k\,dV$$
$$\forall\,k = 1 \dots n_{DegFr}$$

The test function Φ_k is one element of a complete functional basis and n_{DegFr} is the number of degrees of freedom, which depends on the accuracy of the scheme. Integration by parts yields:

$$\int_Q \frac{\partial \mathbf{u}}{\partial t}\,\Phi_k\,dV = -\int_{\partial Q} \mathbf{F}^h\,\Phi_k\,dS$$
$$+ \int_Q \underline{\underline{A}}\,\mathbf{u}\,\frac{\partial \Phi_k}{\partial x} + \underline{\underline{B}}\,\mathbf{u}\,\frac{\partial \Phi_k}{\partial y}\,dV \quad (1)$$

$\int_Q$ and $\int_{\partial Q}$ denote integration over the current grid cell or all its surfaces, respectively. This is the usual weak formulation as used in a finite element scheme, here restricted to the grid cell Q.

One key ingredient of the DG schemes is the representation of the state variables $\mathbf{u}$ as a superposition of time dependent degrees of freedom $\hat{\mathbf{u}}_k(t)$ times space dependent basis functions $\Phi_k(\xi)$. ξ are the cell-local space coordinates. We use a modal ansatz $\mathbf{u} = \sum_{k=1}^{n_{DegFr}} \hat{\mathbf{u}}_k(t)\,\Phi_k(\xi)$ with orthogonal polynomial basis functions of a maximum degree n_{Poly}, which is equal to the order in space -1.

By writing the flux $\mathbf{F}^h$ as sum of the contribution of the cell itself ('*self*') and its neighbor ('*neighbor*') at each surface and implementing the modal ansatz in (Eq. (1)) we get

$$\frac{d\hat{\mathbf{u}}_l}{dt} \int_Q \Phi_l\,\Phi_k\,dV = \underline{\underline{A}}\,\hat{\mathbf{u}}_l \int_Q \Phi_l\,\frac{\partial \Phi_k}{\partial x}\,dV$$
$$- \underline{\underline{A}}_?^+\,\hat{\mathbf{u}}_l^{self} \int_{\partial Q} \Phi_l^{self}\,\Phi_k\,dS$$
$$- \underline{\underline{A}}_?^-\,\hat{\mathbf{u}}_l^{neighbor} \int_{\partial Q} \Phi_l^{neighbor}\,\Phi_k\,dS$$

Here and in the following equations Einstein's summation convention is used for reasons of space. The indices $+$ and $-$ denote the outbound and inbound parts of the flux vector at this interface. The subscripted question

marks indicate, that the scheme does not directly lead to a decision between 'self' and 'neighbor' at this point. Since the modal basis is chosen orthogonal, the integral $\int_Q \Phi_l \, \Phi_k \, dV$ vanishes for $l \neq k$. This allows the direct calculation of $\hat{\mathbf{u}}_l$ without the inversion of a mass matrix. If every element is mapped to a reference triangle or tetrahedron. which is a linear transformation for non-curved elements, every term gets the mapping determinant as additional factor. Then the space integrals can be precomputed analytically or by quadrature and stored. The resulting reduction of the computational effort and its speed-up is a great advantage of the scheme.

2.2 Variable Jacobi matrices

For space dependent, but cell constant mean flows, the values of the Jacobi matrices A and B are ambiguous at the cell interface. For stronger spatial changes of the matrices this can lead to serious problems, as reported in [9]. To avoid this problem, the scheme is extended with space dependent Jacobi matrices within each cell. Therefore the modal representation $\underline{\underline{A}} = \sum_{i=1}^{n_{DegFrJ}} \underline{\underline{\hat{A}}}_i \, \Phi_i$ is introduced with a polynomial basis of the same type as used for the state variables. The maximum polynomial degree may be lower depending on the demand and rates of change of the problem under consideration.

The resulting scheme then reads as

$$
\begin{aligned}
\frac{d\hat{\mathbf{u}}_l}{dt} & \int_Q \Phi_l \, \Phi_k \, dV \\
= & \underline{\underline{\hat{A}}}_i \, \hat{\mathbf{u}}_l \int_Q \Phi_l \, \frac{\partial}{\partial x} \left(\Phi_i \, \Phi_k \right) \, dV \\
& + \underline{\underline{\hat{B}}}_i \, \hat{\mathbf{u}}_l \int_Q \Phi_l \, \frac{\partial}{\partial y} \left(\Phi_i \, \Phi_k \right) \, dV \\
& - \left(\underline{\underline{\hat{A}}}_{i\,?}^+ + \underline{\underline{\hat{B}}}_{i\,?}^+ \right) \hat{\mathbf{u}}_l^{self} \int_{\partial Q} \Phi_i^? \, \Phi_l^{self} \, \Phi_k \, dS \\
& - \left(\underline{\underline{\hat{A}}}_{i\,?}^- + \underline{\underline{\hat{B}}}_{i\,?}^- \right) \hat{\mathbf{u}}_l^{neighbor} \int_{\partial Q} \Phi_i^? \, \Phi_l^{neighbor} \, \Phi_k \, dS \quad (2)
\end{aligned}
$$

After transferring the equation to a reference element the volume integrals can be precomputed. However, this is not possible for the surface integrals, because the mean flow velocity might change between inbound and outbound along the surface and consequently the steadiness of the matrices $\underline{\underline{A}}^+(\xi)$ and $\underline{\underline{A}}_?^-(\xi)$ is not guaranteed any more. A quadrature formula is used instead.

2.3 Nodal integration

The non-constant Jacobi matrices are fundamental to overcome the problems, that can result from a jump of the Jacobi matrices at the cell interface. But in 2D and 3D it is very cumbersome to enforce unambiguous values at the common surface. A further step ahead is an integration scheme, that combines the values within the cell, represented by the modal basis of the cell, with surface nodes, that can be forced to have identical values for both the adjacent cells. On the other hand, the modal scheme with its hierarchical basis functions allows an easy application of order based filters. Gassner et. al. [2] present a nodal-modal DG scheme, that combines both sets of basis functions.

We adopt this approach here and create additionally to the existing modal representation a nodal one for the state u as well as the Jacobi matrices A and B:

$$
\mathbf{u} = \sum_{i=1}^{n_{DegFr}} \hat{\mathbf{u}}_i \, \Phi_i = \sum_{i=1}^{n_{Nodes}} \tilde{\mathbf{u}}_i \, \psi_i
$$

Hence, the surface flux integral in (Eq. (2)) can be written as

$$
\begin{aligned}
& \int_{\partial Q_j} \mathbf{F}^h \, \Phi_k \, dS \\
& = \sum_{k=1}^{n_{BndNds}} \left(\underline{\underline{\tilde{A}}}_m^+ + \underline{\underline{\tilde{B}}}_m^+ \right) \psi_m(\xi_{Nd_{j,k}}) \, \tilde{\mathbf{u}}_l^{self} \\
& \cdot \psi_l^{self}(\xi_{Nd_{j,k}}) \, \Phi_k^{self}(\xi_{Nd_{j,k}}) \, w_k \\
& + \sum_{k=1}^{n_{BndNds}} \left(\underline{\underline{\tilde{A}}}_m^- + \underline{\underline{\tilde{B}}}_m^- \right) \psi_m(\xi_{Nd_{j,k}}) \, \tilde{\mathbf{u}}_l^{neighbor} \\
& \cdot \psi_l^{neighbor}(\xi_{Nd_{j,k}}) \, \Phi_k^{self}(\xi_{Nd_{j,k}}) \, w_k
\end{aligned}
$$

where $\underline{\underline{A}}$, $\underline{\underline{B}}$, $\hat{\mathbf{u}}_l$, Φ_l and ω_k are the Jacobi matrices, degrees of freedom of the state variables, basis functions and integration weights in the modal scheme, respecitvely, and $\underline{\underline{\tilde{A}}}_m$, $\underline{\underline{\tilde{B}}}_m$, $\tilde{\mathbf{u}}_l$, ψ_l and w_k their equivalents in the nodal scheme. The latter is constructed in the way, that its degrees of freedom are equal to the state at the location of the correspondent node. The distribution of the nodes is based on Gauss-Lobatto points, which, in contrast to the Gauss quadrature points, also include nodes on the interval boundaries and consequently on the element surfaces in 2D or 3D.

The transfer between the modal degrees of freedom and their nodal counterparts can be done by a matrix multiplication $\tilde{\mathbf{u}} = \underline{\underline{\mathcal{V}}} \, \hat{\mathbf{u}}$ and $\hat{\mathbf{u}} = \underline{\underline{\mathcal{V}}}^{-1} \, \tilde{\mathbf{u}}$, respectively, where $\mathcal{V}_{ij} = \Phi_j(\xi_{Nd_i})$ is the Vandermonde matrix and $\mathcal{V}^{-1}$ its pseudo-inverse.

To achieve the full order of the scheme, the integration of $\underline{\underline{A}} \, \mathbf{u}$, each with a modal representation of the degree n_{Poly}, has to be of the order $2 \, n_{Poly}$ with the corresponding number of Gauss points or the product has to be projected on a n_{Poly}-basis which corresponds to an "order truncation". Both of these approaches result in a performance drawback. However, in the nodal scheme, the multiplication is done at each of the nodal points and consequently the product is automatically a projection on a n_{Poly}-basis and needs only the original number of integration points for a full order integration.

2.4 Superparametric elements

For complex shaped domains the spatial discretization with straight edged elements leads to a high number of elements to capture the geometry and to guarantee a good approximation. This may strongly reduce in addition the time step due to their small size. To avoid this, we use curved elements at the curved wall boundaries, which should in principle be based on a mapping ansatz of the same spatial order as the underlying numerical scheme. For practical simulations such a highly accurate representation of the boundary is usually not needed and the acoustic simulation rarely exceeds 4th order of accuracy, an ansatz with $p \leq 3$ is used for the mapping:

$$
\mathbf{x}(\xi, \eta) = \sum_{i=0}^{3} \sum_{j=0}^{3-i} \gamma_{ij} \, \xi^i \, \eta^j \, (1 - \xi - \eta)^{3-i-j}
$$

which can be rewritten as $\mathbf{x}(\xi, \eta) = \mathbf{L}(\xi, \eta) \, \underline{\underline{E}}$ with an space dependent part $\mathbf{L}(\xi, \eta)$ and an element dependent, precomputable part $\underline{\underline{E}} \left(\underline{a}, \underline{b} \right)$ where a are the positions of the element corners and b are the supporting points of the B-splines of the edges.

2.5 Complete scheme

If the previously described parts are put together, the complete space operator can be formulated. In the unit triangle it reads

$$
\begin{aligned}
0 = &\frac{\partial}{\partial t} \hat{u}_{lp}^{(m)} \int_{T^{(m)}} \phi_k^{(m)} \phi_l^{(m)} \left| \underline{\underline{J}} \right| \, d\xi \, d\eta \\
&+ \sum_{j=1}^{3} \int_{\partial T^{(m_j)}} \phi_k^{(m)} F_p^h \left| S \right| \, d\chi \\
&- \hat{u}_{lq}^{(m)} \int_{T^{(m)}} \left[\hat{A}_{pqt} \frac{\partial}{\partial \xi} \left(\phi_k^{(m)} \phi_t^{(m)} \right) \xi_x \right. \\
&+ \hat{A}_{pqt} \frac{\partial}{\partial \eta} \left(\phi_k^{(m)} \phi_t^{(m)} \right) \eta_x \\
&+ \hat{B}_{pqt} \frac{\partial}{\partial \xi} \left(\phi_k^{(m)} \phi_t^{(m)} \right) \xi_y \\
&+ \left. \hat{B}_{pqt} \frac{\partial}{\partial \eta} \left(\phi_k^{(m)} \phi_t^{(m)} \right) \eta_y \right] \phi_l^{(m)} \left| \underline{\underline{J}} \right| \, d\xi \, d\eta \quad (3)
\end{aligned}
$$

with a space dependent $\underline{\underline{J}} = \underline{\underline{J}}(\xi) = \frac{\partial \mathbf{x}}{\partial \xi}$. Some algebra leads to

$$
0 = \frac{\partial}{\partial t} \hat{u}_{lp}^{(m)} \int_{T^{(m)}} \phi_k^{(m)} \phi_l^{(m)} |\underline{\underline{J}}| \, d\xi \, d\eta \quad (4)
$$

$$
+ \sum_{j=1}^{3} \int_{\partial T^{(m_j)}} \phi_k^{(m)} F_p^h \left| S \right| \, d\chi \quad (5)
$$

$$
- \hat{u}_{lq}^{(m)} \left(\hat{A}_{pqt} E_r^y - \hat{B}_{pqt} E_r^x \right) \quad (6)
$$

$$
\cdot \int_{T^{(m)}} \left[\frac{\partial}{\partial \xi} \left(\phi_k^{(m)} \phi_t^{(m)} \right) \frac{\partial}{\partial \eta} L_r \right.
$$

$$
\left. - \frac{\partial}{\partial \eta} \left(\phi_k^{(m)} \phi_t^{(m)} \right) \frac{\partial}{\partial \xi} L_r \right] \phi_l^{(m)} \, d\xi \, d\eta. \quad (7)
$$

The integral term in the part (Eq. (4)) is the entry M_{kl} of the mass matrix, which is element dependent and can be precomputed. Due to the space dependent matrix J the mass matrix has no longer a diagonal form as described in 2.1. However, since it is time independent, it can be calculated, inverted and stored at the initialization of the computation.
The term (Eq. (5)) denotes the sum over the flux integrals over each side of the element and is calculated by quadrature in each time step.
The term in brackets in (Eq. (6)) denotes the element dependent part of the volume integral. It can be precomputed and stored.
The integral term in (Eq. (7)) is the entry K_{ktrl} of the stiffness matrix, which is element independent and can be precomputed as well.

2.6 Mean flow gradients

This scheme now considers the equation $u_t + A u_x + B u_y = 0$. The complete form, however, is either $u_t + (A \, u)_x + (Bu)_y = 0$, e.g., for the linearized Euler equations (LEE), or $u_t + A \, u_x + B \, y + E(A, B) \, u = 0$ with $E \neq A_x + B_y$, e.g., for the acoustic perturbation equations (APE).

If the first case is considered in the scheme, only the stiffness matrix in term (Eq. (7)) has to be modified to

$$
\int_{T^{(m)}} \left[\frac{\partial}{\partial \xi} \phi_k^{(m)} \frac{\partial}{\partial \eta} L_r - \frac{\partial}{\partial \eta} \phi_k^{(m)} \frac{\partial}{\partial \xi} L_r \right]
$$
$$
\cdot \phi_t^{(m)} \phi_l^{(m)} \, d\xi \, d\eta.
$$

2.7 Time discretization - The Taylor-DG scheme

In the well-known ADER-DG scheme [1] the space operator is applied once to the time-integrated state. For this time integration a Taylor series was made for the state, which needed the derivatives at the beginning of the current time step. These were calculated by the Cauchy-Kovalevskaya (CK) procedure, which uses the governing equation to calculate the time derivatives from space derivatives. It can be seen as a cell-local space operator. Due to its locality this operator can be formulated and implemented such, that arbitrary time derivatives can be calculated in one step, which results in a very fast high order predictor. However, this formulation is unique for each equation system and really cumbersome for 2D or 3D equations or in conjunction with source terms.
Hence, a consecutive application of the CK-procedure is left as an alternative. This reduces the speed-up of the ADER-DG scheme and leads to the idea of using a full space operator instead of the local predictor. This is only a small additional effort for the flux integral, but avoids the necessity of the corrector step in the ADER scheme. These modifications lead to the Taylor-DG scheme, which was proposed by Lörcher et. al. [3]. The value at the new time step can now be calculated by a Taylor series in time:

$$
\mathbf{u}(t_{n+1}) = \mathbf{u}(t_n + dt) = \sum_{k=0}^{\mathcal{O}-1} \frac{dt^k}{k!} \left(\frac{\partial}{\partial t} \right)^k \mathbf{u}(t_n) \quad (8)
$$

As described, the time derivatives at the beginning of the time step are calculated by a consecutive application of the space operator to the lower time derivative:

$$
\left(\frac{\partial}{\partial t} \right)^k \mathbf{u}(t_n) = \underline{\underline{\Theta}} \left(\left[\frac{\partial}{\partial t} \right]^{k-1} \mathbf{u}(t_n) \right)
$$
$$
\forall \, k = 1 \dots \mathcal{O} - 1 \quad (9)
$$

The space operator Θ has been formulated in the last sections in the form $\frac{\partial^k}{\partial t^k} u = \Theta(u)$ but can, for a linear equation, also be used like in equation (Eq. (9)) through a consecutive derivation in time of the governing equation. The higher computational effort per time step due to the repeated application of the space operator can partly be compensated by a 50 to 100% higher stable time step. Furthermore, the effort can be reduced by an order-reduction approach, which was as well presented by Lörcher et al. It benefits from the fact, that the higher time derivatives of $\mathbf{u}$ are multiplied by powers of dt, which rises the temporal convergence by $k-1$ (see equation (Eq. (8))). This allows a lower order determination of the derivatives without losing the global order of convergence and can reduce the computational effort. Furthermore, the number of steps is one lower than the temporal order for arbitrary orders, which reduces the effort compared to a high order Runge-Kutta scheme (e.g. standard RK with $\mathcal{O} > 4$ or LDDRK with 5 steps for $\mathcal{O}4$).

2.8 Filtering

The acoustic sources are usually given with a fine spatial resolution on the grid of the flow simulation, while the acoustic propagation allows a coarser grid. This can cause aliasing effects, which lead to serious stability problems in the acoustic simulation. Spatial filtering is a suitable method to avoid this problem. In the presented calculation a modal filter, as presented by Hesthaven [11], was used. The basic idea is to eliminate the small scale disturbances which can not be accurately resolved on the coarser grid, by reducing the influence of the high order modes:

$$u_i^{filtered} = \alpha_i\, u_i \qquad \forall\, i = 1 \dots n_{DegFr} \qquad (10)$$

The filter coefficients depend on the space order to which the degrees of freedom i are related (see Table (1)). It

i_{DegFr}	1	2 ... 3	4 ... 6	7 ... 10
α_i	1.0000	0.9995	0.8688	0.0272

Table 1: Coefficients of modal filter for $p = 3$, $n_{DegFr} = 10$

has to be made sure that the coefficient for the first degree of freedom, which is the cell mean value, is equal to one to ensure the conservation property of the filter. For the presented calculations the filter was applied to $\left(\frac{\partial}{\partial t}\right)^k \mathbf{u}(t_n)$ after each Taylor-DG step.

3 The hybrid grid scheme - PIANO+

As stated before, unstructured grids are very suitable for simulations in complex shaped domains due to their straightforward mesh generation. However, in the far field the generation of structured grids is comparably easy. Hence, it is favourable to benefit from the advantages of structured solvers in terms of memory demand, grid handling effort and visualization. This led to the idea of coupling schemes for those different grid types. These were the presented solver NoisSol and the finite-difference (FD) solver PIANO (Perturbation Investigation of Aerodynamic Noise [10]).

For the hybrid computation the computational domain is splitted such, that both programs work on non-overlapping grids with straight coupling interfaces. The information of the coupling partner are included using ghost cells (DG) or ghost points (FD). There the continuity of the primitive variables is enforced, which proved to be the best way to prevent artificial reflections at the interface. The data exchange is done by an extension of the MPI infrastructure, that was already implemented in both solvers.

The main focus in this coupling framework was on the automatization of the coupling process to make it applicable for industrial applications. For detailed information about the coupled scheme see [8].

4 Application to airfoil noise - the NASA 30P30N test case

One topic that is of great interest for computational aeroacoustic applications in aerospace sciences is the noise generation of an airfoil in high-lift configuration, i.e., with deployed slat and flap.

This application is also a demanding test case for acoustic simulation programs, since it combines a very inhomogeneous flow, a complex geometry and many different noise generation mechanisms. In this application a three part airfoil is examined, which was described by Lockard and Choudhari in 2009 [4]. The calculation presented here bases on a RANS computation for an unswept wing with an angle of attack of 4°, a Mach number of 0.17 and a Reynolds number of 1.7e6. Based on this flow field sound sources in 2D were calculated by Roland Ewert of the IAS at the German Aerospace Center (DLR) applying their Fast Random Particle Mesh (FRPM) method [6]. The source calculation was limited to a rectangular region around the slat trailing edge (see Figure (1)).

The mean flow values have also been taken from the RANS calculation.

The acoustic simulations were performed with the Acoustic Perturbation Equations (APE), type 4 , see Ewert and Schröder [7]. The space and time order of the scheme were set to 4, the time step became 3.45e-5 in both cases. For the uncoupled simulation a
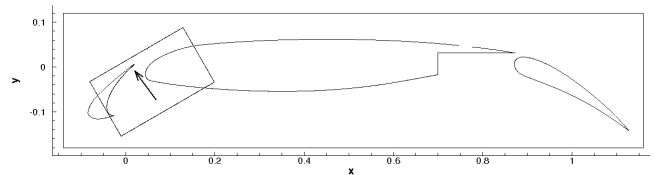
Figure 1: Setup NASA 30P30N (Arrow points to center of microphone circle.)

circular domain with a radius of 3.5 around the origin was used. For the coupled computation 4 NoisSol processes and 4 PIANO processes with 4 blocks each were combined. The grid setup is shown in Figure (2). Figure (3) shows a good qualitative agreement between
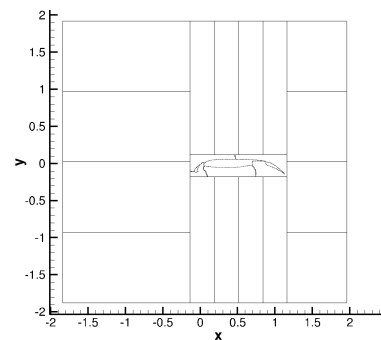
Figure 2: Grid setup for coupled computation

the frequency spectra of the here presented calculations and the reference solution by Lockhard [5]. Also the pressure fields, Figure (4) and Figure (5), agree very well.

Table (2) shows a comparison of the computation times, where t_{sim} is the dimensionless simulated time and t_{CPU} the CPU time in hours. The uncoupled computation has been performed on a cluster with Intel Xeon Nehalem 2.8 GHz CPUs. For the coupled computation an AMD-Opteron equipped cluster with 2.4 GHz has been used.

A conclusion can not be derived straightforward from these results. Motivated by the strong decay of NoisSol's performance some additional test runs

were performed at the same cluster, which showed a 8 times better performance for both solvers. This is probably due to load changes on the system. The tests furthermore showed, that the overall performance for this particular test case is at its optimum between 4 and 8 NoisSol processes coupled to 4 PIANO processes.

Currently under examination is a sudden instability in the near field, which occurred after $t_{sim} \approx 9.0 \approx 260000\ dt$ for pure NoisSol and $\approx 4.6 \approx 135000\ dt$ for PIANO+. Due to the long period of successful computation this is probably related to a strong, source triggered disturbance.
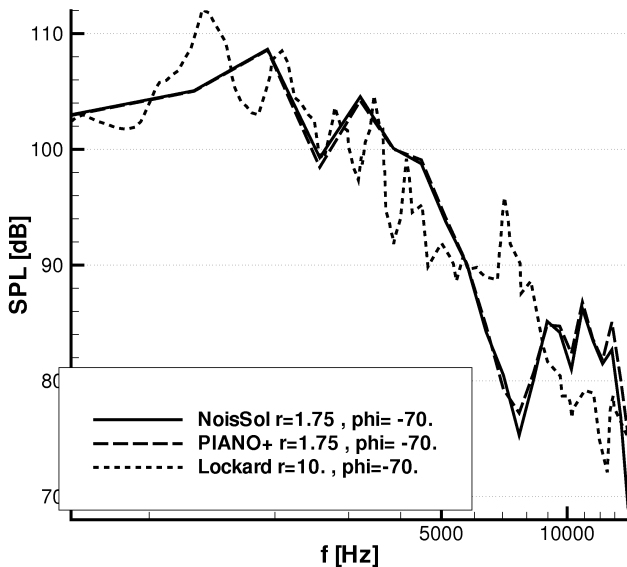
Figure 3: Sound pressure level, NoisSol, PIANO+ and Lockhard [5]
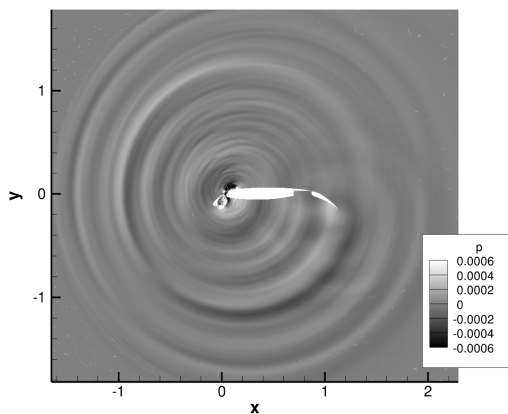
Figure 4: Pressure field, uncoupled computation, t=2.0

5 Conclusion

The presented DG scheme was applied to the NASA 30P30N airfoil noise test case as stand-alone solver and in a coupled framework. The results are very encouraging from the qualitative and quantitative point of view and proved the operability of the scheme. To improve the applicability a reliable examination of the performance behavior of the coupled scheme for different
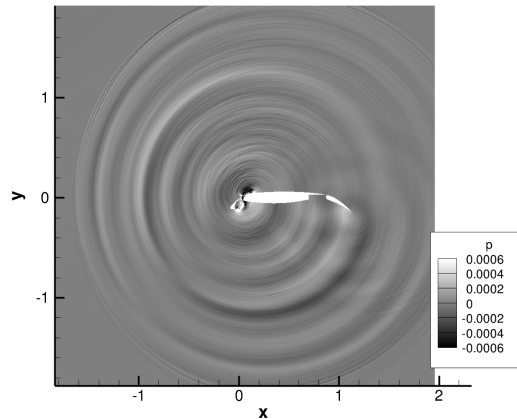
Figure 5: Pressure field, coupled computation, t=2.0

	Uncoupled	Coupled
Code	NoisSol	NoisSol
n_{DegFr}	0.747e6	0.28e6
dx	0.002…0.2	0.002…0.01
t_{sim}	9.03	4.61
t_{CPU}	1840	1370
$t_{CPU}/$ $(n_{DegFr} \cdot t_{sim})$	27.3e-5	106e-5

	Coupled	
Code	PIANO	Combined
n_{DegFr}	6.57e6	6.85e6
dx	0.004	
t_{sim}	4.61	4.61
t_{CPU}	1370	2750
$t_{CPU}/$ $(n_{DegFr} \cdot t_{sim})$	4.53e-5	8.70e-5

Table 2: Computation times

CPU distributions and in comparison to the uncoupled scheme is necessary.

Acknowledgement

References

[1] M. Dumbser: Arbitrary High Order Schemes for the Solution of Hyperbolic Conservation Laws in Complex Domains. PhD thesis, Universität Stuttgart (2005)

[2] G. J. Gassner, F. Lörcher, C.-D. Munz and J. S. Hesthaven: Polymorphic nodal elements and their application in discontinuous Galerkin methods. JCP **228**, Issue 5 (2009)

[3] F. Lörcher, G. Gassner and C.-D. Munz: Arbitrary High Order Accurate Time Integration Schemes for Linear Problems. ECCOMAS CFD (2006)

[4] D. P. Lockard and M. M. Choudhari: Noise Radiation from a Leading-Edge Slat. AIAA paper 2009-3101 (2009)

[5] D. P. Lockard and M. M. Choudhari: The Effect of Cross Flow on Slat Noise. AIAA paper 2010-3835 (2010)

[6] R. Ewert: Broadband slat noise prediction based on CAA and stochastic sound sources from a fast random particle mesh (RPM) method. Computers & Fluids **37** (2008)

[7] R. Ewert and W. Schröder: Acoustic Perturbation Equations based on Flow Decomposition via Source Filtering. JCP **188** (2003)

[8] A. Birkefeld and C.-D. Munz: A Hybrid Method for CAA. Proc. of the 36. Jahrestagung für Akustik der Deutschen Gesellschaft für Akustik DAGA, Berlin (2010)

[9] A. Birkefeld and C.-D. Munz: Advances in Numerical Aeroacoustics with the Discontinuous Galerkin Solver NoisSol. Proc. of the 17. Symposium der Strömungsmechanischen Arbeitsgemeinschaft STAB, Berlin (2010)

[10] J. Delfs, M. Bauer, R. Ewert, H. Grogger, M. Lummer and T. Lauke: Numerical Simulation of Aerodynamic Noise with DLR's aeroacoustic code PIANO. Manual, IAS DLR Braunschweig (2007)

[11] J. S. Hesthaven and T. Warburton: Nodal Discontinuous Galerkin Methods: Algorithms, Analysis and Applications. Springer Verlag, New York (2008)

JET NOISE AND COHERENT STRUCTURES

A. V. G. Cavalieri, P. Jordan and Y. Gervais

Abstract

We present a review of recent work by our group showing how noise at low axial angles from subsonic turbulent jets can be calculated using models of axisymmetric structures. A theoretical basis is developed using Lighthill's analogy, and the lower azimuthal modes in the flow are shown to present higher acoustic efficiencies. The experimental sound field of a Mach 0.6 jet is shown to be predominantly axisymmetric, and to agree with characteristics predicted by a model of axisymmetric structures with amplification, saturation and decay. Such a model is then constructed for the same jet using Parabolised Stability Equations, and good agreement is obtained with both the velocity fluctuations on the jet centerline and the radiated sound field. For situations when time-domain approaches are needed, such as real-time flow control, a wave-packet source model with temporal variations of amplitude and spatial extent is presented, again leading to good agreement to the radiated sound in two Mach 0.9 jet simulations. All the presented results are consistent with the picture of sound generation by coherent structures forming a wavepacket. We argue that such coherent structures do not dominate the velocity fluctuations, as in low-Reynolds-number flows or forced jets, but are still present in turbulent unforced jets, and their high acoustic efficiency compensate their relatively low energy.

1 Introduction

The calculation of the radiated sound by a turbulent flow relies on some knowledge about the fluctuations of the flow variables; for instance, in an acoustic analogy source terms are built as functions of the turbulent flow. In this sense, a better characterisation of the turbulence should lead to improvements of the ability to predict the sound radiation.

One of the first applications of Lighthill's[25] acoustic analogy was done by Proudman[32] by assuming a model of isentropic turbulence. Moreover, the development of causality techniques[24], where the two-point correlation between source and sound is considered as the local contribution of the source to the radiated noise, is based on a similar view of the turbulence as a set of uncorrelated eddies, which reflected the view of turbulence at that time.

This idea was somewhat changed by a series of studies of flow visualisation[11, 3], of forced shear flows[11, 19, 4], and of the near pressure field[31, 35, 37]. Such studies employ techniques that tend to highlight the 'coherent part' of the velocity fluctuations. Of course one cannot claim that a high-Reynolds number jet is entirely constituted of such coherent structures; but their presence, even with a relatively low energy if compared to the overall turbulence, changes dramatically the sound radiation.

The present paper deals with this issue reporting some recent progress on the calculation of the radiated sound by subsonic jets by exploring this coherent velocity fluc-

tuations. In sec. 2 we recall, using Lighthill's theory, how a train of axisymmetric structures may lead to efficient sound generation, particularly for low polar angles. To search evidence of such radiation, in sec. 3 we explore the acoustic field of subsonic jets decomposed into azimuthal Fourier modes, and in sec. 4 a model of coherent structures as instability waves is used to determine the radiated sound. Finally, in sec. 5 we present a wave-packet model with some jitter in amplitude and spatial extent[5] to calculate sound radiation in the time domain, which allows calculation of temporally-localised acoustic bursts that are observed in the acoustic field of jets[21, 18, 23].

2 The acoustic radiation of coherent structures

The solution of Lighthill's equation for the pressure p in the frequency domain is given in a point $\vec{x}$ as

$$p(\vec{x}, \omega) = \iiint \frac{\partial^2 T_{ij}}{\partial y_i \partial y_j}(\vec{y}, \omega) \frac{\exp(-ik|\vec{x} - \vec{y}|)}{4\pi|\vec{x} - \vec{y}|} d\vec{y}, \quad (1)$$

where $k = \omega/c$ and a time factor of $\exp(i\omega t)$ is implied.

The sound radiation for low axial angles can be approximated by using only the T_{11} component of Lighthill's stress tensor. Such a source is only appropriate at these low angles. Throughout this paper we will focus on this component and the associated low angle radiation; however, the agreement between the radiated sound and higher angles may be increased as the other components of the tensor are accounted for.

To explore the effect of coherent velocity fluctuations on the radiated sound, we can use cylindrical coordinates (z, r, ϕ) for the volume integral and decompose Lighthill's tensor on azimuthal modes, as done previously by Michalke[27], Michalke and Fuchs[30] and Mankbadi and Liu[26]. With the far-field assumption, the radiated sound for the T_{11} component is given as

$$p(\vec{x}, m, \omega) = -\frac{(-i)^m k^2 \cos^2\theta e^{-ikx}}{2x}$$

$$\times \int e^{-ikz\cos\theta} dz \int T_{11}(z, r, m, \omega) J_m(kr\sin\theta) r dr. \quad (2)$$

Eq. (2) shows that the different azimuthal modes m of T_{11} radiate sound with a factor related to the Bessel functions J_m that account for the interference within a ring of radius r. In order to show how J_m changes for some values of Strouhal number, we have plotted in Figure (1) the factor $J_m(kr\sin\theta)$ for $r = D/2$ with an acoustic Mach $M = 0.9$ at a position $\theta = 30°$.

We see in Figure (1) that for low Strouhal numbers the axisymmetric mode has the highest acoustic efficiency. For instance, for St = 0.2 the azimuthal mode 1 has a radiation 18dB lower than mode 0 if both modes are considered to have the same amplitude for T_{11}. The higher modes are even less effective. Hence, we should
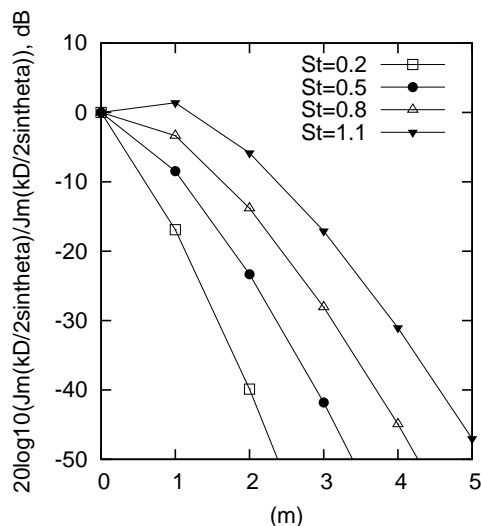
Figure 1: Relative efficiencies of azimuthal mode m compared to the axisymmetric case, considering $\theta = 30°$, $M = 0.9$ and $r = D/2$.

expect considerable sound radiation from structures in the flow with significant azimuthal coherence. For higher frequencies the differences become gradually lower, and $m = 0$ and 1 have similar efficiencies at a Strouhal number around 1. For lower Mach numbers, the dominance of mode 0 is accentuated, as seen in Figure (2) for $M = 0.6$.
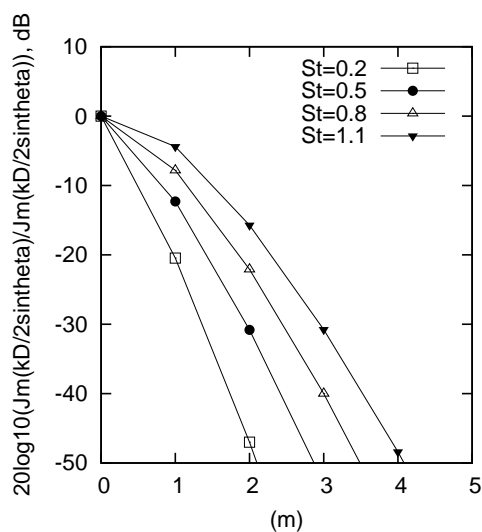
Figure 2: Relative efficiencies of azimuthal mode m compared to the axisymmetric case, considering $\theta = 30°$, $M = 0.6$ and $r = D/2$.

If we are interested at the peak directions and frequencies for subsonic jet noise, which correspond to low angles and low Strouhal numbers, we can thus concentrate on the axisymmetric mode. Moreover, if $kr \sin\theta \ll 1$, we can make a further approximation by taking $J_0(kr \sin\theta)$ to be 1, and the axisymmetric source is equivalent to a line distribution of quadrupoles. The far-field pressure is given by

$$p(\vec{x}, m = 0, \omega) = -\frac{k^2 \cos^2\theta \, \mathrm{e}^{-\mathrm{i}kx}}{2x}$$
$$\times \int \mathrm{e}^{-\mathrm{i}kz\cos\theta}\mathrm{d}z \int T_{11}(z, r, m = 0, \omega)r\mathrm{d}r. \quad (3)$$

A further interesting result is given by Crow[10, 7], who assumed a line distribution consisting of a hydrodynamic wave with an envelope given by a Gaussian,

$$\int T_{11}(z, r, m, \omega)r\mathrm{d}r = 2\rho U\tilde{u}\mathrm{e}^{-\mathrm{i}k_H z}\mathrm{e}^{-\frac{z^2}{L^2}}, \quad (4)$$

to model the amplification, saturation and decay of an instability wave (or wavepacket). For this model the sound radiation is given by

$$p(\vec{x}, m = 0, \omega) = -\frac{\rho_0 U\tilde{u}M_c^2(k_H D)^2 L\sqrt{\pi}\cos^2\theta}{8x}\mathrm{e}^{-\mathrm{i}kx}$$
$$\times \mathrm{e}^{-\frac{L^2 k_H^2 (1 - M_c \cos\theta)^2}{4}}. \quad (5)$$

The exponential dependence of the sound field on θ, present in Eq. (5), has been labelled *superdirectivity*[9, 6]. This dependence is significant if the axial extent of the wavepacket, which is related to L, is comparable to the acoustic wavelength.

This is in contrast with the results for compact sources. A compact eddy has a directivity (for the pressure field) given by the factors $\cos^2\theta$, $\sin^2\theta$ or $\sin\theta\cos\theta$ depending on the orientation of the quadrupole axes. The superdirective field of Eq. (5) is due to the interference in an extensive source between the regions of positive and negative sign.

The theoretical results presented so far show that if such axisymmetric wavepackets, with a high axial extent, are present in a jet, we should expect to measure such superdirectivity in the acoustic field. The next section presents an experimental investigation of this issue.

3 Experimental observations in the acoustic field

The decomposition of the experimental acoustic field into azimuthal Fourier modes can be done either by performing correlations[15, 20] or by using a microphone array[2], and, in a linear context such as any linearised acoustic analogy, we can expect that the lower azimuthal modes will correspond to sound radiation by structures with high azimuthal coherence.

The cited studies[15, 20, 2] have shown that only a small number of azimuthal modes are present in the acoustic field. This is also the case for the near pressure field[37]. Figure (3) reproduces results from Cavalieri *et al.*[6]. The results show that most of the sound radiation at low axial angles is axisymmetric, the higher modes having lower contributions to the OASPL.
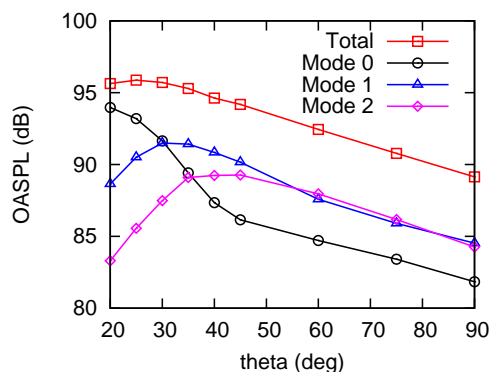
Figure 3: Directivity for a $M = 0.6$ jet.

If we take the peak frequency of the spectrum, which for this jet is St = 0.2, the dominance of the axisymmetric mode is even more pronounced, as seen in Figure (4)(a).
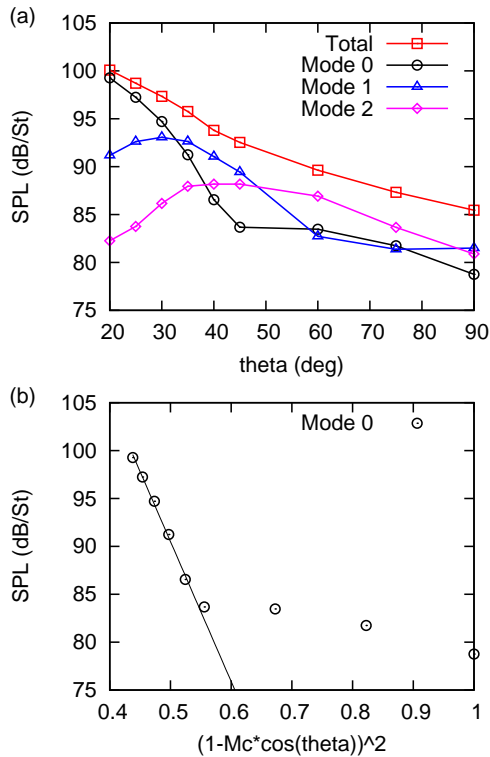
Figure 4: SPL for St=0.2 for the Mach 0.6 jet as a function of (a) θ and (b) $(1 - M_c \cos \theta)^2$.

Additionally, we note that the mode-0 radiation has a peculiar shape, with a sharp increase from $\theta = 45°$ to $\theta = 20°$. To verify if this corresponds to a wave-packet directivity shape such as the one in Eq. (5), we see in Figure (4) the SPL for St = 0.2 as a function of $(1 - M_c \cos \theta)$. The straight line in the plot shows that the sound field of the axisymmetric mode is indeed *superdirective*, in agreement with what would be expected by a source in the form of a hydrodynamic wave of axisymmetric structures with amplification, saturation and decay.

4   Instability-wave models of coherent structures

If one expects the sound source in a jet to have the form of a hydrodynamic wave, models with low computational cost based on spatial instability can be employed. In this case, the Navier-Stokes equations are often linearised using a base flow that can be either the laminar solution or the mean turbulent flow; in the latter case, the linearisation is based on a scale separation between the wavepackets with long correlation lengths and the smaller turbulent structures. It is possible, nonetheless, to extend wave-packet models to include nonlinearities[34, 33].

Stability theory assumes that the flow variables have a dependence on $\exp[i(\omega t - \alpha x - m\phi)]$ if parallel flow is considered[28, 29], or on $\exp[i(\omega t - m\phi)] \exp[i \int_0^x \alpha(x')dx']$ for a base flow changing slowly on the axial direction x[8, 36], where the frequency ω is real and the axial wavenumber α is complex for the spatial instability problem. Such an *Ansatz* is appropriate for the

observed coherent structures in forced jets[11, 19], and one can infer that this may also be the case for a range of frequencies and azimuthal modes of unforced jets. Recent studies[35, 16] have shown that this is indeed the case using comparisons between instability-wave models and the pressure on the near field of jets.

For the M=0.6 jet of section 3, we have modelled wavepackets using linear Parabolised Stability Equations (PSE)[17] taking the experimental mean field as the base flow, as in Gudmundsson and Colonius[16]. The approach is described in more detail by Rodriguez *et al.*[33], and the present results are taken from this reference. Figure (5) presents a comparison of the amplitudes of the calculated instability waves with experimental velocity fluctuations on the jet centerline, measured with a hot wire. Only the axisymmetric mode has axial velocity fluctuations at $r = 0$[1]. Hence, the comparison between experiment and axisymmetric instability waves is appropriate.
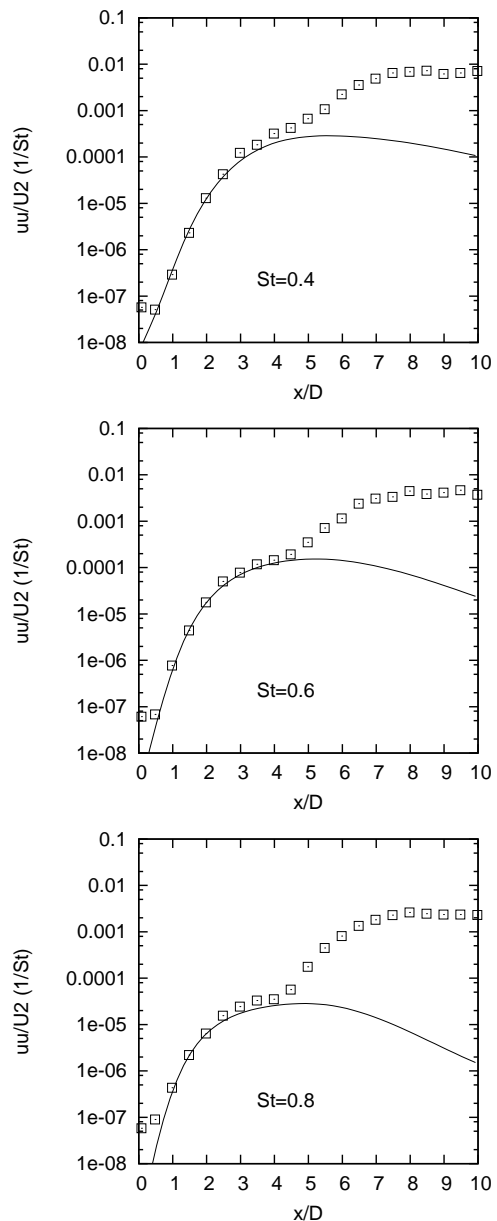
Figure 5: Comparison between PSE (lines) and experiment (points) for $M = 0.6$ and (a) St=0.4, (b) St=0.6 and (c) St=0.8

The results of Figure (5) show a remarkable agreement between the PSE results and the experiment up to $x/D \approx 5$, which is close to the end of the potential core. It should be noted that since these are linear instability waves, the PSE solution has a free amplitude. In Figure (5) the amplitude was matched with the velocity fluctuations at $x = 2D$.

The sound radiation of the instability wave was computed with Eq. (3), with $T_{11}(z, r, m = 0, \omega)$ given as $\rho_0 U(z, r) u(z, r, m = 0, \omega)$, where U is the experimental mean axial velocity and $u(z, r, m = 0, \omega)$ is given by the PSE solution for the axisymmetric mode at each frequency. Results, taken from Rodriguez *et al.*[33], are shown in Figure (6). The agreement found is good, especially considering that the source has been matched only with information from the *velocity* field. The radiated sound from the modelled instability waves is thus consistent with the experimental far acoustic field.
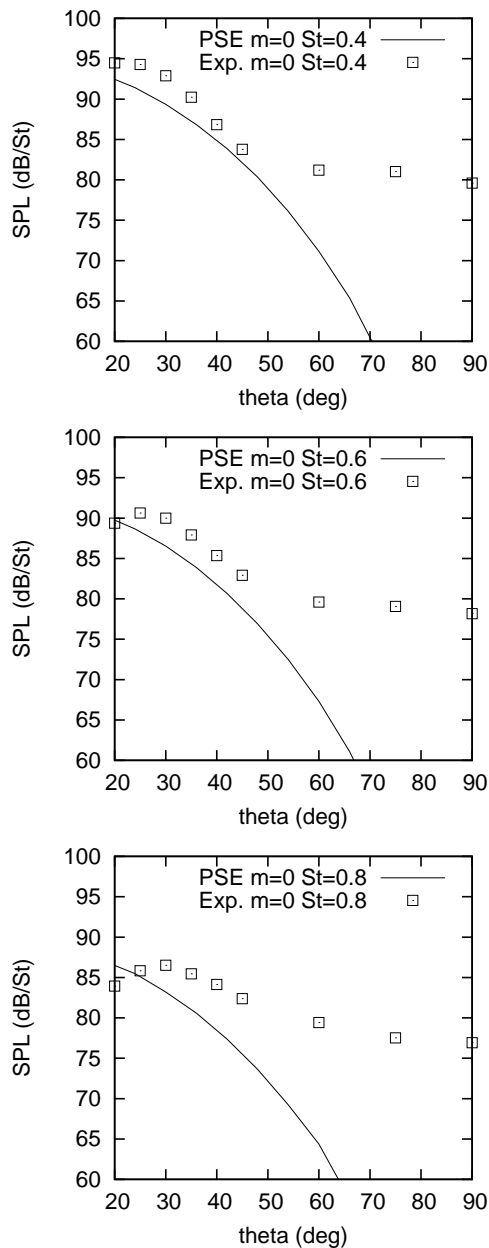
Figure 6: Comparison between the acoustic field calculated with PSE (lines) and the experiment (points) for $M = 0.6$ and (a) St=0.4, (b) St=0.6 and (c) St=0.8

5 A time-domain approach

All the preceding analysis was made on the frequency domain, which simplifies considerably the calculations by the use of periodicity. The results, both in the turbulent and in the acoustic fields, are compared to spectra, and represent thus an average behaviour of the jet.

To obtain information on the spectral content of a flow, one needs information from a long time series to perform Fourier transforms. If we are interested in control applications in real time this can become problematic, and a time-domain prediction of sound radiation can be advantageous.

An attempt to model wave-packet radiation in the time domain is presented by Cavalieri *et al.*[5]. In the present section we recall the proposed approach and some of the results of this reference. The main idea is to model the coherent structures spanning a *range* of frequencies as a wavepacket with a single, central frequency, but with temporal changes of amplitude and spatial extent. This is similar to the work of Ffowcs Williams and Kempton[13], who modelled "jitter" in the convection velocity of a wavepacket.

One of the models in [5] takes the form of a wavepacket with a Gaussian envelope, with slowly-changing amplitude A and spatial extent L:

$$T_{11}(\mathbf{y}, \tau) = 2\rho_0 U \tilde{u} \frac{\pi D^2}{4} \delta(y_2) \delta(y_3)$$

$$\times A(\tau) e^{i(\omega \tau - k_H y_1)} e^{-\frac{y_1^2}{L^2(\tau)}} \quad (6)$$

The source is concentrated on a line, which involves assuming radial compactness as in section 2. With this expression for the T_{11} component of Lighthill's stress tensor, the far-field pressure is given by

$$p(\mathbf{x}, t) = -\frac{\rho_0 U \tilde{u} M_c^2 (k_H D)^2 L \left(t - \frac{|\mathbf{x}|}{c}\right) \sqrt{\pi} \cos^2 \theta}{8|\mathbf{x}|}$$

$$\times A\left(t - \frac{|\mathbf{x}|}{c}\right) e^{-\frac{L^2 \left(t - \frac{|\mathbf{x}|}{c}\right) k_H^2 (1 - M_c \cos \theta)^2}{4}} e^{i\omega \left(t - \frac{|\mathbf{x}|}{c}\right)}. \quad (7)$$

The radiated sound depends on the instantaneous amplitude and interference within a wave-packet. Superdirective radiation, as in Crow's model[10] presented in section 2, is predicted, as can be seen from the exponential dependence on θ. However, in this case the superdirective radiation can occur in intermittent bursts, due to an increase of the amplitude A or a decrease of the source extent L[1]. A number of studies has shown that such bursts are present in the acoustic field of jets[21, 18]. Such bursts are also superdirective[23], and are mostly present for the axisymmetric mode[22]. All these characteristics of the sound radiation of subsonic jets are in agreement with the simplified model of Eq. (6) and Eq. (7).

To assess the pertinency of this model, results of Eq. (7) have been compared to the DNS of Freund[14] and to LES of Daviller[12]. In both cases, the instantaneous amplitudes and spatial extents have been obtained by fits to a short-time Fourier series applied to the axisymmetric mode of the velocity on the jet lipline, filtered

---

[1]Although there is a linear dependence of the radiated sound on L in Eq. (7), which would lead to a reduction of the radiated sound if L decreases, the exponential dependence on $L^2(t - |\mathbf{x}|/c)k^2$ leads to an *increase* of the sound radiation if L is reduced. An example is presented by Cavalieri *et al.*[5, section 3].

for $0.3 \leq$ St ≤ 0.5. Results are shown in Figure (7), taken from [5], and are compared to the axisymmetric mode of the pressure for the same frequency range. The agreement found at low angles (high x_1 in Figure (7)) between the models with "unsteady envelope", i.e. when temporal changes of A and L follow the simulation data, is reasonable for both computations.
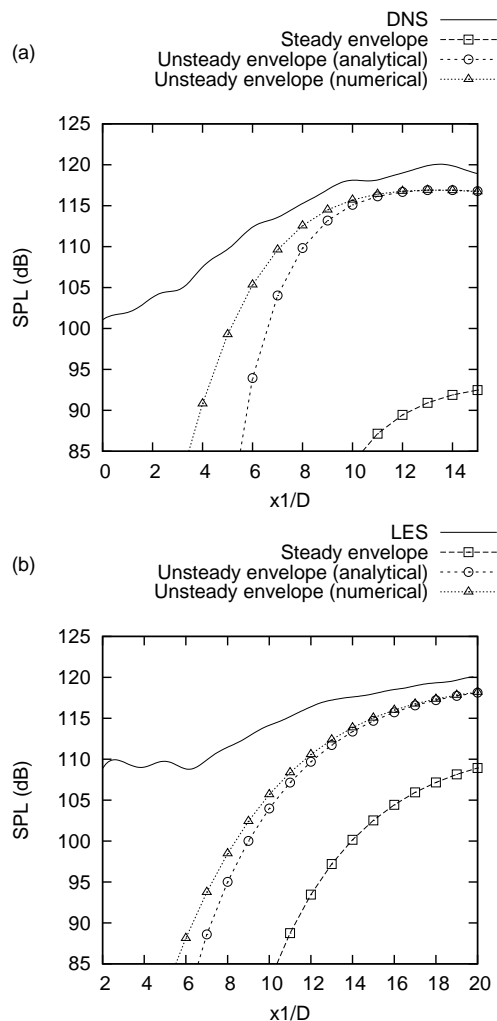
Figure 7: Comparison between jittering wave-packet models and numerical data of Mach 0.9 jets: (*a*) DNS (Freund[14]) and (*b*) LES (Daviller[12]). SPL taken for the axisymmetric mode of the acoustic pressure for $0.3 \leq$ St ≤ 0.5. Taken from [5].

6   Conclusions

The results reviewed in the present paper show that the sound field at low axial angles from subsonic jets can be calculated using source models consisting of a train of axisymmetric structures that undergo an amplitude modulation. This has been accomplished both using experimental data, for which the source is modelled as linear instability waves, or numerical simulations that allow the use of full volume data for the velocity field.

The current progress in both numerical simulations and measurement techniques can guide us further into the nature of the low azimuthal modes in free jets. Although a detailed characterisation of the full turbulent field seems to be a hard task, focus on the axisymmetric and on other low azimuthal modes allows considerable simplifications. Such modes have a

relatively low energy level if compared to the overall turbulent fluctuations[30], but their higher acoustic efficiency can lead to significant sound radiation.

References

[1] G. K. Batchelor and A. E. Gill. Analysis of the stability of axisymmetric jets. *Journal of Fluid Mechanics*, 14(04):529–551, 1962.

[2] C. Brown and J. Bridges. Acoustic efficiency of azimuthal modes in jet noise using chevron nozzles. Technical report, National Aeronautics and Space Administration, 2006.

[3] G. L. Brown and A. Roshko. On density effects and large structure in turbulent mixing layers. *Journal of Fluid Mechanics*, 64(4):775–816, 1974.

[4] G. Broze and F. Hussain. Nonlinear dynamics of forced transitional jets: periodic and chaotic attractors. *Journal of Fluid Mechanics*, 263:93–132, 1994.

[5] A. V. G. Cavalieri, P. Jordan, A. Agarwal, and Y. Gervais. Jittering wave-packet models for subsonic jet noise. *Journal of Sound and Vibration*, 330(18-19):4474–4492, 2011.

[6] A. V. G. Cavalieri, P. Jordan, T. Colonius, and Y. Gervais. Axisymmetric superdirectivity in subsonic jets. In *17th AIAA/CEAS Aeroacoustics Conference and Exhibit*, Portland, OR, USA, June 5-8 2011.

[7] D. G. Crighton. Basic principles of aerodynamic noise generation. *Progress in Aerospace Sciences*, 16(1):31–96, 1975.

[8] D. G. Crighton and M. Gaster. Stability of slowly diverging jet flow. *Journal of Fluid Mechanics*, 77(2):397–413, 1976.

[9] D. G. Crighton and P. Huerre. Shear-layer pressure fluctuations and superdirective acoustic sources. *Journal of Fluid Mechanics*, 220:355–368, 1990.

[10] S. C. Crow. Acoustic gain of a turbulent jet. In *Phys. Soc. Meeting, Univ. Colorado, Boulder, paper IE*, volume 6, 1972.

[11] S. C. Crow and F. H. Champagne. Orderly structure in jet turbulence. *Journal of Fluid Mechanics*, 48(3):547–591, 1971.

[12] G. Daviller. *Etude numérique des effets de temperature dans les jets simples et coaxiaux*. PhD thesis, Ecole Nationale Supérieure de Mécanique et d'Aérotechnique, Poitiers, France (in French), 2010.

[13] J. E. Ffowcs Williams and A. J. Kempton. The noise from the large-scale structure of a jet. *Journal of Fluid Mechanics*, 84(4):673–694, 1978.

[14] J. B. Freund. Noise sources in a low-Reynolds-number turbulent jet at Mach 0.9. *Journal of Fluid Mechanics*, 438:277–305, 2001.

[15] H. V. Fuchs and U. Michel. Experimental evidence of turbulent source coherence affecting jet noise. *AIAA J*, 16(9):871–872, 1978.

[16] K. Gudmundsson and T. Colonius. Instability wave models for the near-field fluctuations of turbulent jets. *Journal of Fluid Mechanics*, 689:97–128, 2011.

[17] T. Herbert. Parabolized stability equations. *Annual Review of Fluid Mechanics*, 29(1):245–283, 1997.

[18] J. I. Hileman, B. S. Thurow, E. J. Caraballo, and M. Samimy. Large-scale structure evolution and sound emission in high-speed jets: real-time visualization with simultaneous acoustic measurements. *Journal of Fluid Mechanics*, 544:277–307, 2005.

[19] A. K. M. F. Hussain and K. B. M. Q. Zaman. The 'preferred mode' of the axisymmetric jet. *Journal of Fluid Mechanics*, 110:39–71, 1981.

[20] D. Juvé, M. Sunyach, and G. Comte-Bellot. Filtered azimuthal correlations in the acoustic far field of a subsonic jet. *AIAA Journal*, 17:112, 1979.

[21] D. Juvé, M. Sunyach, and G. Comte-Bellot. Intermittency of the noise emission in subsonic cold jets. *Journal of Sound and Vibration*, 71:319–332, 1980.

[22] M Kœnig, A. V. G. Cavalieri, P. Jordan, and Y. Gervais. Intermittency of the azimuthal components of the sound radiated by subsonic jets. In *17th AIAA/CEAS Aeroacoustics Conference and Exhibit*, Portland, OR, USA, June 5-8 2011.

[23] M. Kœnig, A. V. G. Cavalieri, P. Jordan, Y. Gervais, and D. Papamoschou. Far-field filtering for the study of jet noise: Mach and temperature effects. In *17th AIAA/CEAS Aeroacoustics Conference and Exhibit*, Portland, OR, USA, June 5-8 2011.

[24] H. K. Lee and H. S. Ribner. Direct correlation of noise and flow of a jet. *The Journal of the Acoustical Society of America*, 52:1280, 1972.

[25] M. J. Lighthill. On sound generated aerodynamically. I. General theory. *Proceedings of the Royal Society of London. Series A, Mathematical and Physical Sciences*, pages 564–587, 1952.

[26] R. Mankbadi and J. T. C. Liu. Sound generated aerodynamically revisited: large-scale structures in a turbulent jet as a source of sound. *Philosophical Transactions of the Royal Society of London. Series A, Mathematical and Physical Sciences*, 311(1516):183–217, 1984.

[27] A. Michalke. A wave model for sound generation in circular jets. Technical report, Deutsche Luft- und Raumfahrt, November 1970.

[28] A. Michalke. Instabilitat eines Kompressiblen Runden Freistrahls unter Berucksichtigung des Einflusses der Strahlgrenzschichtdicke. *Z. Flugwiss*, 19:319–328; English translation: NASA TM 75190, 1977, 1971.

[29] A. Michalke. Survey on jet instability theory. *Progress in Aerospace Sciences*, 21:159–199, 1984.

[30] A. Michalke and H. V. Fuchs. On turbulence and noise of an axisymmetric shear flow. *Journal of Fluid Mechanics*, 70:179–205, 1975.

[31] E. Mollo-Christensen. Jet noise and shear flow instability seen from an experimenter's viewpoint(Similarity laws for jet noise and shear flow instability as suggested by experiments). *Journal of Applied Mechanics*, 34:1–7, 1967.

[32] I. Proudman. The generation of noise by isotropic turbulence. *Proceedings of the Royal Society of London. Series A. Mathematical and Physical Sciences*, 214(1116):119–132, 1952.

[33] D. Rodríguez, A. Samanta, A. V. G. Cavalieri, T. Colonius, and P. Jordan. Parabolized stability equation models for predicting large-scale mixing noise of turbulent round jets. In *17th AIAA/CEAS Aeroacoustics Conference and Exhibit*, Portland, OR, USA, June 5-8 2011.

[34] N. D. Sandham and A. M. Salgado. Nonlinear interaction model of subsonic jet noise. *Philosophical Transactions of the Royal Society A*, 366(1876):2745–2760, 2008.

[35] T. Suzuki and T. Colonius. Instability waves in a subsonic round jet detected using a near-field phased microphone array. *Journal of Fluid Mechanics*, 565:197–226, 2006.

[36] C. K. W. Tam and D. E. Burton. Sound generated by instability waves of supersonic flows. Part 2. Axisymmetric jets. *Journal of Fluid Mechanics*, 138(-1):273–295, 1984.

[37] C. E. Tinney and P. Jordan. The near pressure field of co-axial subsonic jets. *Journal of Fluid Mechanics*, 611:175–204, 2008.

Computational Acoustics And Aerodynamics: A Multi-Objective & Component Outlook

P. G. Tucker

The University of Cambridge
C2AC, School of Engineering
Cambridge, CB3 0DY

Abstract

Aerothermal and aeroacoustic activities are generally treated separately. A more holistic approach is recommended. Noise generation is detrimental to either, stealth, the environment and also potentially energy consumption. Extended explorations involving use of residual acoustic energy for modest positive flow control purposes are needed. There is frequently an intrinsic link between the aeroacoustic and aerothermal behaviours. Hence, we should move to multi-objective, aero-thermo-acoustic design. Many large-scale fluid systems have a high degree of coupling between different zones. Also, the idealized geometrical representations used to represent complex industrial systems can have limited meaning. Hence, larger scale multi-objective simulations are needed. However, these present meshing and computational resource challenges. Although Large Eddy Simulation (LES) and modern analysis techniques allow the links between acoustics and aerodynamics to be readily observed and synergies and tensions explored, typical complex geometry LES make use of excessively under-resolved grids.

1 Introduction

1.1 Environmental impact of energy systems

With the world aircraft fleet projected to double by 2020 & the general growth of energy and transport demands it is becoming urgent to take steps to reduce environmental impact. Noise can be more than just annoying being a contributory factor towards illnesses [1]. Hence, the Advisory Council for Aeronautics Research has set the target of reducing noise by 50% by 2020. They have also set equally ambitious targets for reductions in energy consumption. However, there is a crucial need to treat these elements in a multi-objective sense also exploiting intelligent active and passive control.

Many energy infrastructure projects are based around tremendously powerful & expensive (circa 5% United Kingdom gross domestic product) systems. Hence their initial inception, ultimate success & subsequent refinement is critically based on mathematical/computational models[1].

---

[1] *"Increasingly, simulation is taking the place of expensive and unfeasible experimental testing"* (EPSRC Document "Research priorities and opportunities" 2004). To emphasis the importance, the Office of Science and the Department of Energy in the US, state that "Advances in the simulation of complex scientific and engineering systems provide an unparalleled opportunity for solving major problems that face the nation in the 21st Century" (Scientific Discovery through Advanced Computing – 2000).
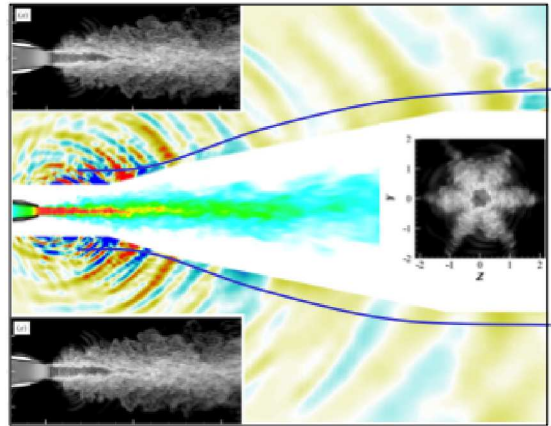
Figure 1: LES of a chevron nozzle showing acoustic waves and turbulence structures in different cut planes (see Xia et al. [2] for more details).

Hence, there is an increasing need to take computational aeroacoustics and computational fluid dynamics skills and link them in both multi-objective design and flow control senses. The output of this linkage being refined predictive technologies and movement towards transformative designs.

1.2 Turbomachinery

Many energy propulsion and generation systems involve gas turbines. A key feature of these is that they consist of rows of rotating blades adjacent to stationary blades. The potential field from the adjacent blades will cause unsteadiness and acoustic waves. This acoustic energy creates boundary layer unsteadiness and hence minor loss (Fritsch and Giles [3]). Charbonnier and Lebouf [4], when modeling a transonic turbine, observed numerous pressure reflections between the stator and rotor blade rows. This resulted in increased energy loss. List et al. [5] show that, when blade rows are in close proximity, bow shocks from downstream blades can enhance upstream vortex shedding and hence acoustics. Furthermore, Raverdy et al. [6], Matsuura and Kato [7], and Atobe and Ikeda [8] demonstrate that (in the absence of upstream wakes) the vortex shedding from blade trailing edges, can couple with suction surface separation bubbles enhancing turbulence. Dufour et al. [9] observe a similar effect but this time for a high-pressure turbine stator. Also, as shown by Butler et al. [10], in turbines, hot streaks, from the combustor migrate to the turbine rotor pressure surface. Hence circumferential variations in inlet temperature will result in unsteady thermal loading

and potential fatigue. However, the convection of the hot spots (entropy waves) also generates noise [11]. Hence, these two elements are intrinsically linked the hot zones both influencing aerodynamics, aeroacoustics and life. The flow in passage containing the blades, is connected by a cavity like (rim seal) zone to the internal cooling system. Rim seal flows are also, in themselves, intrinsically unsteady (see O'Mahoney et al. [12]). They involve complex three-dimensional shear layers. These impinge on downstream surfaces, thus generating an acoustic feedback loop. The blade passing may also potentially excite shear layer cavity interaction resonances or underling unsteady rotor-stator cavity flows.

Through the development bypass ratio engines the jet noise is substantially reduced. Consequently, Tyler and Sofrin [13] explored compressor/fan noise arising from rotating pressure fields spinning with the compressor rotors. Fan noise has both tonal and broadband components [14]. Also, the unsteady rotor-stator interactions will produce sound, notably the interaction of the rotor wakes and tip vortices with downstream stators. These mechanisms will also give rise to aerodynamic loss. Hence, there is a key link between aeroacoustics and aerodynamics. This is particularly so when it is noted that acoustic feedback can substantially modify the mean flow. When exploring flow control, the link can become even clearer. For example, trailing edge ejection can be used to fill in low momentum zones in wakes. This will improve aerodynamic performance but also can reduce noise. Perforated aerodynamic surfaces on intakes can both be used to reduce noise and potentially improve aerodynamic performance [15].
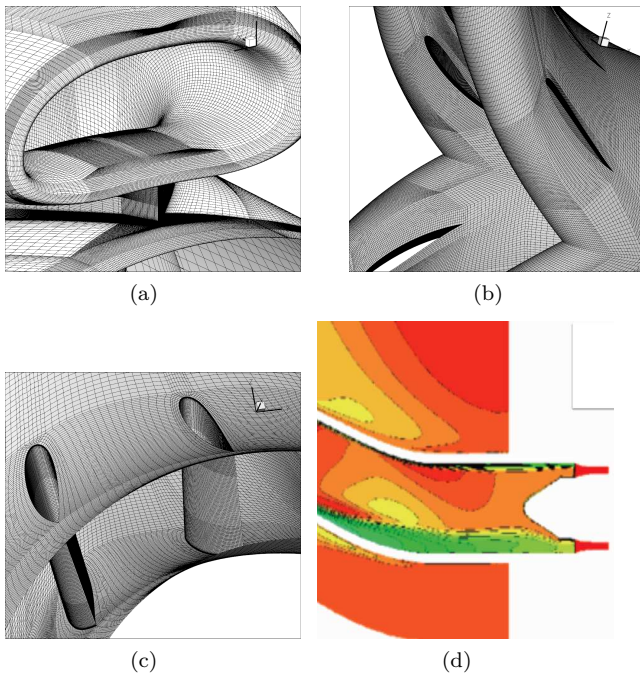
Figure 2: Open rotor intake and duct grid views along with total pressure contours (mid-section plane of a non-bifurcated intake).

As outlined in Eastwood [16], in a real engine upstream of the nozzle, there is a compressor, combustor and turbine. There are also numerous other associated geometrical features. It has been supposed for some time that these may influence the jet noise itself [17] [18]. As noted by Moore [17] the engine internal noise can modify the jet structure. Hence, as can be seen from the above although noise is a byproduct of turbulent flow it can also influ-

ence the flow structure itself. Indeed, Epstein et al. [19] explored to use noise to control compressor stability and [20] separation control on airfoils. Ffowcs-Williams [21] also outlines the potential of noise to both reduce/cancel noise and also enhance aerodynamic performance. The latter are not uncharted waters and pose great research challenges. Nonetheless, the rich flow physics and acoustics insights provided by LES, along with the potential to precisely control excitations might enable us to make advances in the area of using sound to reduce sound and also aerodynamic losses. Hence, there seems a crucial need to treat aerodynamics and aeroacoustics more holistically.
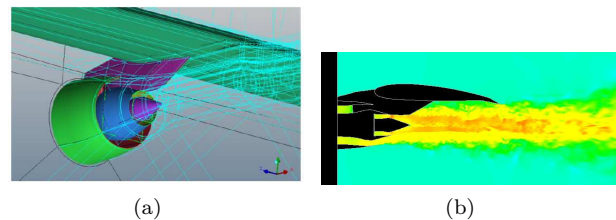
Figure 3: Multiblock grid zones and instantaneous axial velocity contours for a heated jet nozzle-pylon-wing-flap simulation.

Turbochargers (see Baines [22], Winterbone, Nikpour and Frost [23]) are subjected to pulsating flow from engine exhausts. As shown by Baines this can alter the efficiency by nearly 30%. This pulsation might also be a factor in generating excessive turbocharger noise. For radial compressors the impeller blade wakes, as well as resulting in an aerodynamic performance penalty can result in fatigue and also substantial acoustic related problems [24]. Blanco et al. [25] observe that there is a substantial acoustic coupling between the rotor, volute and piping system for centrifugal pumps. Hence, they perform CFD simulations that are coupled to a model for the piping system acoustic modes

1.3 Role of LES

The use of acoustics to positively control flow is far from a new idea. Unfortunately, acoustic fluctuation amplitudes are low relative to for example that of the turbulence. The acoustic energy levels needed to exert substantial flow control can be high (sound pressure levels of around 100 dB) [20] and there is frequency dependence. However, an area of worthwhile exploration would perhaps be to see if ambient noise could be used to produce some modest positive gain. Certainly, with aero engines fractions of a percent in efficiency are of tremendous economic importance. LES solutions readily reveal both flow structural and acoustic information (see, for example, the Figure 1 chevron jet flow LES). Hence, complex interactions can be more readily observed and understood. Techniques are available to correlate acoustic signatures with flow events. An adjoint process does not seem unreasonable where the influence of the acoustic events on the flow can be explored and adjustments made to use the acoustic signatures to positively influence the flow. At a simple level, an acoustic source term at a fixed frequency could be added to numerical solutions. The resulting flow field could be Fourier analyzed. Variations in response at the frequency of excitation or harmonics of it could be indicative of the impact of the acoustic source on the acoustic or flow field. These two aspects could be separated out by a spatial Fourier transform and hence looking at phase velocities.

2 Coupled simulations

A key problem with LES is that inflow and outflow conditions, generally, must be correctly characterized. At inflow boundaries, turbulence must be prescribed that has temporal and spatial scales, which are correctly correlated, and representative of the flow in the actual system. At outflow, for a turbomachine, for example, the need goes beyond simply preventing reflections. For example, a downstream axial compressor redistributes flow and hence has a strong upstream impact. Similarly, upstream rotors have a strong downstream influence. Turbomachines are highly coupled systems. Hence, the specification of inflow and outflow "boundary conditions" presents challenges.
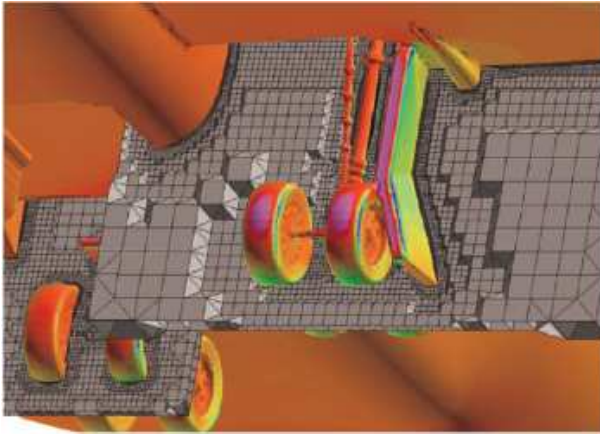
Figure 4: Surface conforming octree grid from Xia et al. [26]

An approach to overcome this and create coupling is to represent upstream and downstream turbomachinery elements using low order models. For example, body forces can be used to replicate the turning and total temperature and pressure distributions. These can be utilized in a multi-fidelity approach. For example in [27] body forces [28] are used to generate the flow turning and axial mass flux induced by an upstream rotor in an open rotor engine and also the influence of a downstream compressor. The rotor model was also adapted to replicate unsteady wakes with controlled momentum deficits, turbulence length scales and intensities. The wakes are found to substantially influence the flow in the intake duct and the distortion levels at the compressor face. The use of azimuthally enhanced body force modeling for fan acoustics is also reported in Defoe et al. [29]. In Eastwood [16] body forces are used to model wakes from upstream blade rows inside a jet nozzle. These wakes generate large scales eddies in the LES simulation. Much work has been conducted on isolated jets, the focus being on exploring noise from the propulsive jet in gas turbine engines. However, as shown in Xia et al. [30] and Eastwood et al. [31] the wing, flap, pylon, and internal jet geometry can substantially influence the development of the jet plume and acoustics. Hence, it seems future evolutions in acoustics modelling should encompass the following elements:

- Multi fidelity modeling that accounts for the coupled nature of systems such as gas turbine engines and hence the challenges with regards to inflow and outflow boundary conditions – especially for LES;

- Multi-objective simulations that enable the tensions between aerodynamic and aeroacoustic re-

quirements to be explored and potential synergies between these elements and ultimately;

- Multi-physics simulations.

Again, in the multi-fidelity context accurately predicting aerodynamic and aeroacoustic behaviour can need coupled fluid-structure calculations. For example, with open rotor engines to accurately capture aerodynamics, blade rotor untwist needs to be captured [32]. In the hydroacoustics of marine propellers structural deflections are a key sound source component as is the multi-physics element of cavitation.

2.1 Meshing and grid densities

As we move to making large scale coupled simulations meshing presents a great challenge. Figures 2 and 3 show meshes and simulations for recent large-scale coupled simulations for intakes of open rotor engines [27] and exhaust plumes [30]. Both present substantial acoustic challenges. In Figure 2, the first three frames give mesh views and the last frame contours of total pressure but for a coupled intake that has no bifurcation (see [27]). Figure 3 shows the block topology and contours of instantaneous axial velocity for a nozzle-pylon-wing-flap LES type calculation. The core flow is hot. The multi-block meshes used for these simulations give relatively high computational performance in terms of accuracy and cost for both computational acoustics and aerodynamics. However, they are tremendously time consuming to produce and need considerable skill. Work automating this process is ongoing [33] [34] [35]. For highly complex geometries, hexahedral rich octree meshes (see Figure 4), with surface conforming cells [26] offer solution accuracy but carry the computational overhead of an unstructured flow solver. On balance perhaps overset grids offer a good balance with regards to computational efficiency and mesh generation time scales [36] [37]. Naturally they are amenable to high order solutions.
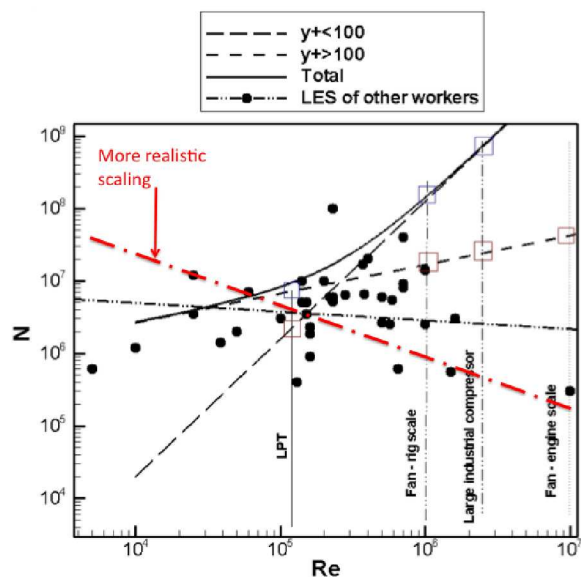
Figure 5: Grid requirements for LES and hybrid LES-RANS combined with typical grid densities actually used by various groups (from [38])

Main gas path turbomachinery calculations the rotor-stator pairs can have non-integer ratios of blade counts. This prevents the use of simple periodic boundary conditions. To overcome this problem adjustments in blade

count are frequently made. However, this will greatly influence the tonal acoustics. Then, to enable reduced circumferential domain calculations chorochronic (in Greek choros relates space and chronos to time) periodicity may need to be exploited. With this, the time history at the periodic boundaries is either directly stored (Erdos et al. [39]) or stored as a Fourier series (Gerolymos et al. [40]) and used in a time-lagged fashion. However, these are not appropriate for LES enforcing rigid correlation of temporal behaviour between blades. [41]. As a final point, Figure 5 shows a plot of LES grid count against Reynolds number for typical turbomachinery calculations. The full symbols represent the LES of other workers reviewed in [38]. The dashed dot dot line is the best fit to this data. The (red) chain dashed line is an estimate of the actual trend of LES grid resolution with Re. It is clear from the plot that typical turbomachinery LES grids do not follow the necessary near Re2.5 cost scaling (see full line) needed for LES, indeed the scaling appears to be to a negative power. Nonetheless, the advent of Graphical Processor Units (GPU) driven by the children's game industry does give access a substantial increase in access to affordable computer power [42]. This should alleviate some of this grid resolution defect but also use will need to be made of hybrid LES-RANS simulations. However, it is noted that the RANS zone will corrupt dipole sound sources and their propagation. Also, Strouhal number limitations when predicting far field sound will need subgrid acoustic source modelling.

3 Conclusions

Extended explorations involving use of residual acoustic energy for modest positive flow control purposes are needed. There is frequently an intrinsic link between the aeroacoustic and aerothermal behaviours. Hence, we should move to multi-objective, aero-thermo-acoustic design. Many large-scale fluid systems have a high degree of coupling between different zones. Also, the idealized geometrical representations used for complex industrial systems can have limited meaning. Hence, larger scale multi-objective and even, ultimately, multi-physics simulations are needed. However, these present meshing and computational resource challenges. Although LES and modern analysis techniques allow the links between acoustics and aerodynamics to be readily observed and synergies and tensions explored typical complex geometry LES make use of excessively under-resolved grids. However, advances in affordable computing such as GPUs will be helpful.

References

[1] Rosenlund Mea, "Increased prevalence of hypertension in a population exposed to aircraft noise," *Occup Environ Med.*, 2001;58:769-773.

[2] Xia H, Tucker P, Eastwood S. "Large-eddy simulations of chevron jet flows with noise predictions," *International Journal of Heat and Fluid Flow.* 2009;30(6):1067-1079.

[3] Fritsch G, Giles M. "Second-order Effects of Unsteadiness on the Performance of Turbomachines." *In: ASME Paper 92-GT-389*; 1992.

[4] Charbonnier D, Leboeuf F. "Development of a model for the deterministic stresses in a transonic turbine stage." *In: Proc. 5th European Conferfence on Turbomachinery*, 2003, Praha.

[5] List MG, Gorrell SE, Turner MG. "Investigation of loss generation in an embedded transonic fan at several gaps using high-fiedlity, time accurate CFD." *Proc. ASME Turbo Expo Power for Land*, Sea and Air GT 2008, Berlin Germany. 2008 Paper No GT-2008-51220.

[6] Raverdy B, Mary I, Sagaut P, "Liamis N. High-resolution large-eddy simulation of flow around low-pressure turbine blade." *AIAA Journal.*, 2003 March;41(3):390-397.

[7] Kato C, Yamade Y, Wang H, Guo Y, Miyazawa M, Takaishi T, Yoshimura S, Takano Y. "Numerical prediction of sound generated from flows with a low Mach number." *Computers & fluids.* 2007;36(1):53-68.

[8] Atobe T, Ikeda T. "Flow instability around a 2D airfoil induced by acoustic disturbances at low Reynolds numbers." *In: ICAS 2010, 27th Int. Congress of the Aeronautical Sciences*, 2010.

[9] Dufour G, Gourdain N, Duchaine F, Vermorel O, Gicquel L, Boussuge J, Poinsot T. "Large Eddy Simulation Applications." 2009.

[10] Butler T, Sharma O, Joslyn H, Dring R. "Redistribution of an inlet temperature distortion in an axial flow turbine stage." *Journal of Propulsion Power.*, 1989;5:64-71.

[11] Schemel C, Thiele F, Bake F, Lehmann B, Michel U. "Sound generation in the outlet section of a gas turbine combustion chamber." *In: 10th AIAA/CEAS Aeroacoustics Conference*, Paper No. 2004-2929.

[12] O'Mahoney TSD, Hills NJ, Chew JW, Scanlon T. "Large-eddy simulation of rim seal ingestion." *ASME Turbo Expo 2010: Power for Land, Sea, and Air (GT2010)*, June 14-18, 2010, Glasgow, UK. 2010 Paper no 2010-22962, pp. 1155-1165.

[13] Tyler J, Sofrin T. "Axial flow compressor noise studies." *SAE transactions.* 1962;70:309-332.

[14] Ashcroft G, Nuernberger D. "A computational investigation of broadband noise generation in a low-speed axial fan." *In: AIAA Paper,* AIAA 2001-0512, 2001.; 2001.

[15] Thomas RH, Choudhari MM, Joslin RD,. "Flow and noise control: toward a closer linkage." *In: ICAS 2002 Congress.* p. pp. 841.1 - 841.10.

[16] Eastwood S. "Hybrid LES - RANS of Complex Geometry Jets." *PhD thesis*, Cambridge University, School of Engineering.

[17] Moore C. "The role of shear layer instability waves in jet exhaust noise." *Journal of Fluid Mechanics.* 1977;80(2):321–367.

[18] Ffowcs Williams JE HD. "Sound generation by turbulence and surfaces in arbitrary motion." *Phil Trans R Soc Lond*, Ser A. 1969;264(8):321-342.

[19] Epstein AH, Ffowcs Williams JE, Greitzer EM. "Active suppression od aerodynamic instabilites in turbomachines." *AIAA J. of Propulsion and Power.* 1986;5(2):204-211.

[20] Collins FG, Zelenevitz J. "Influence of sound upon separated flow over wings." *AIAA J.* 13(3):408-410.

[21] Ffowcs Williams JE. "Noise, anti-noise and fluid flow control." *Phil. Trans. R. Soc. Lond. A.* 2002;360:821-832.

[22] Baines N. "Turbocharger turbine pulse flow performance and modelling - 25 years on." *9th International Conference on Turbochargers and Turbocharging,* Inst. Mech. Eng., 19-20 May 2010 London. 2010.

[23] Winterbone DE. "A Contribution to the Understanding of Turbocharger Turbine Performance in Pulsating Flow." *Proc. Inst. Mech. Eng.*, Part C: Mech. Eng. Sci. 1991.

[24] Guelich JF, Bolleter U. "Pressure pulsations in centrifugal pumps." *ASME J. of Vibration and Acoustics.*, 1992;114:272-279.

[25] Blanco E, Barrio R, Fernandez J, Parrondo J, Marcos A. "Numerical simulation of the generation of fluid-dynamic perturbations in a centrifugal pump due to rotor-volute-circuit interaction." *Proc. v9th European Conference on Turbomachinery,* Fluid Dynamics and Thermodynamics. 2011 615-624.

[26] Xia H, Tucker PG, Dawes WN. "Level sets for CFD in aerospace engineering." *Progress in Aerospace Sciences.* 2010;46(7):274-283.

[27] Loiodice S, Tucker PG. "Coupled open rotor engine intake simulations." *48th AIAA Aerospace Sciences Meeting and Exhibit,* Orlando, Florida, Jan. 2010 Paper No AIAA-2010-840.

[28] Gong Y. "A computational model for rotating stall inception and inlet distortions in multistage compressors." *Ph.D. thesis,* Massachusetts Institute of Technology, US; 1998.

[29] Defoe J, Narkaj A, Spakovszky ZS. "A novel MPT noise prediction methodology for highly-integrated propulsion systems with inlet flow distortion." *In: 15th AIAA/CEAS Aeroacoustics Conference (30th AIAA Aeroacoustics Conference)*, May 11-13, 2009, Miami, Florida, AIAA 2009–3366, 2009.

[30] Xia H, Tucker PG, Eastwood S. "The influence of geometry on jet plume development." Submitted to Progress in Aerospace Sciences. 2011.

[31] Eastwood S, Tucker PG. "Hybrid LES-RANS of complex geometry jets." *Int. J. Aeroacoustics.* 2011;10(5&6):661-686.

[32] Zachariadis A, Hall C. "Application of a Navier-Stokes solver to the study of open rotor aerodynamics." *Journal of Turbomachinery.* 2011;133:031025.

[33] Xia H, Tucker PG. "Fast equal and biased distance fields for medial axis transform with meshing in mind." *Applied Mathematical Modelling.* 2011;35:5804-5819.

[34] Xia H, Tucker PG. "Finite volume distance field and its application to medial axis transforms." *Int. J. of Numerical Methods in Engineering.* 2010;82(1):114-134.

[35] Malcevic I. "Automated blocking for structured CFD gridding with an application to turbomachinery secondary flows." *In: 20th AIAA Computational Fluid Dynamics Conference,* 27 - 30 June 2011, Honolulu, Hawaii, AIAA Paper No. 2011-3049; 2011.

[36] Jefferson-Loveday R, Tucker PG. "LES of impingement heat transfer on a concave surface." *Numerical Heat Transfer, Part A.* 2010;58(4):247-271.

[37] Jefferson-Loveday R, Tucker PG. "Wall resolved LES and zonal LES of round jet impingement heat transfer on a flat plate." *Numerical Heat Transfer, Part B.* 2011;59:190-208.

[38] Tucker PG. "Computation of unsteady turbomachinery flows: Part 2 - LES and hybrids." *Progress in Aerospace Sciences (In Press).* 2011.

[39] Erdos J, Alzner E, McNally W. "Numerical solution of periodic transonic flow through a fan stage.", 1976, p.1976.

[40] Gerolymos G, Michon G, Neubauer J. "Analysis and application of chorochronic periodicity in turbomachinery rotor/stator interaction computations." *Journal of propulsion and power.* 2002;18(6):1139-1152.

[41] Olausson M. "Turbomachinery aeroacoustic calculations using non-linear methods," *PhD Thesis*, Department of Applied Mechanics, Chalmers University of Technology, Gothenburg, Sweden. 2011.

[42] Brandvik T, Pullan G. "Acceleration of a 3D RANS solver using commodity graphics hardware." *In Proceedings of the 46th AIAA aerospace sciences meeting and exhibit,* Reno, Nevada. Paper no. AIAA-2008-0607.

[43] Available from: http://www-diva.eng.cam.ac.uk/energy/acoustics/tyrenoise.html.

[44] Earle S. Press Release - "Sounding the Depths: Supertankers, Sonar, and the Rise of Undersea Noise, Executive Summary." New York, N.Y.:. [Internet]. 1999, Available from: www.nrdc.org.

Analytical and Numerical Wxtensions of Amiet's Incoming Turbulence Noise Theory to Account for Near-field Effects

J. Christophe[1], K. Kucukcoskun[2,3] and C. Schram[1]

[1]*von Karman Institute for Fluid Dynamics,*
1640 Rhode-St-Genèse, Belgium
julien.christophe@vki.ac.be, christophe.schram@vki.ac.be
[2]*LMS International, 3001 Leuven, Belgium*
[3]*Current address: Laboratoire de Mécanique des Fluides et d'Acoustique,*
UMR CNRS 5509 & Ecole Centrale de Lyon, 69134 Ecully Cedex, France
korcan.kucukcoskun@ec-lyon.fr

1 Introduction

Flow-generated sound is nowadays a serious concern in many engineering applications. The noise pollution generated is particularly problematic in transport industry. In aeronautical applications, the noise emitted by wings and high-lift devices [5, 20, 22, 23], is a significant component of the overall noise radiated. In automotive industry, the cooling fan systems [6] are examples of flow-generated noise that are considered as key factors in the overall appreciation of a vehicle. In other domains of industrial applications as in wind turbines [10], laptops or desktops cooling fan systems [15], or Heating, Ventilating and Air Conditioning (HVAC) [7, 16], the aerodynamic noise is also a major concern.

These applications have in common that the generic aerodynamic noise production mechanism is due to the interaction between an airfoil with the turbulent flow in which it is submerged. In some instances the turbulence is generated upstream of the airfoil and is convected over it with the main flow, in which case we refer to an *incoming turbulence noise* production mechanism. In other configurations the blade is placed in a laminar incoming flow, but turbulence is still generated in the boundary layers that develop along the chord of the blade, and is scattered by the blade trailing edge. This is commonly referred to as *trailing-edge noise* or *self-noise*. Both mechanisms have been considered by Amiet [3, 4], with an analysis based on linearized airfoil theory to model the lift variation of the airfoil subjected to incoming or self-generated turbulence in a first step, and on Curle's aeroacoustic analogy [9] to predict the radiation of the equivalent dipoles in a second step.

A number of simplifying hypotheses are made in the derivation of these theories. It is for example often assumed that the listener is located in the geometrical and acoustical far-field of the blade. While valid for certain applications (e.g. wind-turbines), this hypothesis is clearly violated for a fan confined within a casing, if we want to evaluate the incident field on the casing to compute the acoustic scattering by the rotor neighboring surfaces. This aspect constitutes the focus of this work, in which we investigate acoustical and geometrical near-field effects that are often ignored when applying Amiet's theory. The work presented in this paper is focused on the incoming turbulence noise problem, but the proposed improvements could also be applied on the trailing-edge noise theory [4, 17, 21] as well.

2 Amiet's theory for incoming turbulence noise

An airfoil of chord $C = 2b$ and span $2d$ is placed in a turbulent fluid with a mean flow velocity U. The x axis is the streamwise/chordwise direction, aligned with the convection speed U, y is the spanwise direction and z the crosswise direction. The origin of the coordinates system is at the center of the airfoil. The turbulence is assumed to be frozen and represented in terms of its spectral wavenumber components, k_x and k_y, as illustrated in Fig. 1.
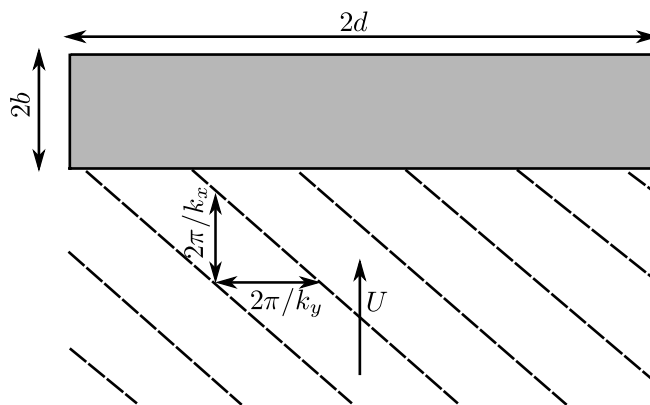
Figure 1: Representation of a single skewed gust sweeping over the airfoil.

The airfoil is assumed to be a flat plate of zero thickness, and linearised theory is applied. For this particular problem, an analytical solution is found for the transfer function between the impacting gust and the airfoil pressure jump. This is obtained by iteratively solving scattering problems at the airfoil edges. The main leading-edge scattering obtained by assuming the airfoil extends toward infinity in the downstream direction, is then corrected by a trailing-edge back-scattering contribution which fully accounts for the finite chord length [2, 19, 18].

The acoustic response of the airfoil subjected to incoming turbulence involves the radiation of spanwise and chordwise distributed dipoles obtained from the pressure jump across the airfoil surface. The airfoil and the coordinate system are represented on Fig. 2. The coordinates
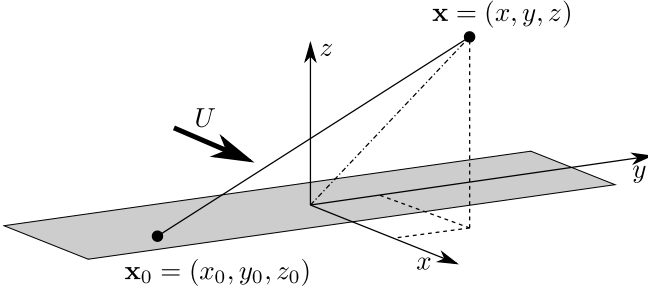
Figure 2: Coordinate system of an airfoil placed in a uniform velocity U in the x direction with a dipole source located at $\mathbf{x}_0$ and a receiver located at $\mathbf{x}$.

of the observer are defined as $\mathbf{x} = (x, y, z)$ and the local coordinates on the airfoil surface are $\mathbf{x}_0 = (x_0, y_0, z_0)$. The local system of coordinates is located at the center of the airfoil, with then $z_0 = 0$ as the airfoil surface is infinitively thin and aligned on the (x, y) plane. The airfoil is placed in a uniform flow in the chordwise positive x direction, defining a Mach number $M = U/c_0$ and the corresponding parameter $\beta = \sqrt{1 - M^2}$, with c_0 the speed of sound. The position of the receiver, taking into account convection effect, is then given by the vector:

$$\mathbf{x}_t = \left(((x - x_0) - M\sigma_s)/\beta^2; y - y_0; z\right), \quad (1)$$

with $\sigma_s = \sqrt{(x - x_0)^2 + \beta^2[(y - y_0)^2 + z^2]}$. The magnitude of the vector $\mathbf{x}_t$, i.e. the propagation distance corrected for convection effects, is then written as:

$$\sigma_t = (\sigma_s - M(x - x_0))/\beta^2. \quad (2)$$

The sound radiation of a single dipole placed on the airfoil for a particular angular frequency ω (and $k = \omega/c_0$) is given by [9, 11]:

$$p(\mathbf{x}, \omega; \mathbf{x}_0) = \frac{ikz\,\hat{l}(\mathbf{x}_0, \omega)}{4\pi\sigma_s^2}\, e^{-ik\sigma_t}\left(1 + \frac{1}{ik\sigma_s}\right), \quad (3)$$

where $\hat{l}$ is the lift component of the dipole considered. Integrating over the complete surface of the airfoil S_y, the corresponding power spectral density (PSD) for the sound pressure observed at the receiver position due to a dipole network on the airfoil is then expressed as:

$$S_{pp}(\mathbf{x}, \omega) = \iint_{S_y} \iint_{S_y'} \left(\frac{\rho_0 kz}{2}\right)^2 U \frac{1}{\sigma_s^2 \sigma_s'^2}$$
$$\left(1 + \frac{1}{ik\sigma_s}\right)\left(1 + \frac{1}{ik\sigma_s'}\right)^* e^{-ik(\sigma_t - \sigma_t')}$$
$$\int_{-\infty}^{\infty} \Phi_{ww}(K_x, k_y)\, e^{-ik_y(y_0 - y_0')}$$
$$g(x_0, K_x, k_y)\, g^*(x_0', K_x, k_y)\, dk_y dS_y' dS_y \quad (4)$$

where the superscript $()^*$ denotes the complex conjugate operator. $K_x = \omega/U$ is a particular value of the chordwise wavenumber, $\Phi_{ww}(K_x, k_y)$ is the power spectrum of the incoming gust upwash velocity component, and the aerodynamic transfer function g relates the incoming gust to the profile pressure jump as introduced above (see Ref. [3] for more details on the derivation). No assumptions on the acoustical or geometrical far-field are applied in the development of this formulation and it can be used in a general context.

2.1 Far-field approximations

In the acoustic far-field, we have for the acoustical near-field contribution $1/ik\sigma_s' \ll 1$, and Eq. (4) becomes:

$$S_{pp}(\mathbf{x}, \omega) = \iint_{S_y} \iint_{S_y'} \left(\frac{\rho_0 kz}{2}\right)^2 U \frac{1}{\sigma_s^2 \sigma_s'^2}\, e^{-ik(\sigma_t - \sigma_t')}$$
$$\int_{-\infty}^{\infty} \Phi_{ww}(K_x, k_y)\, e^{-ik_y(y_0 - y_0')}$$
$$g(x_0, K_x, k_y)\, g^*(x_0', K_x, k_y)\, dk_y dS_y' dS_y. \quad (5)$$

2.1.1 Geometrical spanwise near-field and chordwise far-field

Kucukcoskun *et al.* [13, 14] considered the particular case of an observer placed at a distance that is comparable to the spanwise extension of the airfoil. When considering large aspect ratio airfoils and an observer placed at similar distance than the spanwise extent, $(y - y_0)^2 \approx y^2$ may consist in a gross approximation while supposing that $(x - x_0)^2 \approx x^2$ can be still quite reasonable. The simplified propagation distance is then considered to be :

$$\sigma_s \approx \sigma_k = \sqrt{x^2 + \beta^2(y - y_0)^2 + \beta^2 z^2}. \quad (6)$$

This simplified propagation distance σ_s appears in two different terms of formulation (5), in the complex exponential $e^{-ik(\sigma_t - \sigma_t')}$, through the use of Eq. (2), and in the scaling factor $\frac{1}{\sigma_s^2 \sigma_s'^2}$. The influence of the simplified propagation distance of Eq. (6) on the final sound result is assumed to have more importance on the scaling factor than on the complex exponential. The scaling factor of formulation (5) is then approximated using

$$\frac{1}{\sigma_s^2} \approx \frac{1}{\sigma_k^2}. \quad (7)$$

Concerning the complex exponential, a first order development in Taylor series around the center of the airfoil $(x_0, y_0) = (0, 0)$ of the observer distance σ_s is considered, requiring the sound listener to be placed in the geometrical far-field.

$$\sigma_s \approx \sigma_0 \left(1 - \frac{xx_0 + \beta^2 yy_0}{\sigma_0^2}\right), \quad (8)$$

where $\sigma_0^2 = x^2 + \beta^2(y^2 + z^2)$.

In this geometrical spanwise near-field (but chordwise far-field) approximation, we obtain [14]:

$$S_{pp}(\mathbf{x}, \omega) = \left(\frac{\rho_0 kzb}{2}\right)^2 U \int_{-\infty}^{\infty} |\mathcal{K}(\mathbf{x}, K_y, k_y)|^2$$
$$\Phi_{ww}(K_x, k_y)\, |\mathcal{L}(\mathbf{x}, K_x, k_y)|^2\, dk_y, \quad (9)$$

where the function $\mathcal{K}$ is expressed as a combination of exponential integrals E_1 [1] (with $K_y = ky/\sigma_0$), as shown by Kucukcoskun *et al.* [13], and $\mathcal{L}$ is the aeroacoustic transfer function introduced by Amiet [19].

2.1.2 Geometrical spanwise and chordwise far-field

When the listener is located at a large number of airfoil chord *and* span lengths from the airfoil, the assumption

$(y - y_0) \approx y$ becomes acceptable,

$$\frac{1}{\sigma_s^2} \approx \frac{1}{\sigma_0^2}, \quad (10)$$

and Eq. (9) can be further approximated by:

$$S_{pp}(\mathbf{x}, \omega) = \left(\frac{\rho_0 k z b}{\sigma_0^2}\right)^2 \pi U d$$
$$\int_{-\infty}^{\infty} \frac{\sin^2\left[(K_y - k_y) d\right]}{\pi d (K_y - k_y)^2}$$
$$\Phi_{ww}(K_x, k_y) \left|\mathcal{L}(\mathbf{x}, K_x, k_y)\right|^2 dk_y, \quad (11)$$

which is the expression derived by Amiet [3] that can be further simplified in case of large aspect ration airfoil, for which the cardinal sine function of Eq. (11) tends to a Dirac function of the spanwise wavenumber k_y:

$$S_{pp}(\mathbf{x}, \omega) = \left(\frac{\rho_0 k z b}{\sigma_0^2}\right)^2 \pi U d$$
$$\Phi_{ww}(K_x, K_y) \left|\mathcal{L}(\mathbf{x}, K_x, K_y)\right|^2. \quad (12)$$

3 Numerical validation

In order to compare the different formulations, a numerical test is performed. The sound spectrum emitted by an airfoil subjected to homogeneous turbulence properties is considered and computed using the different formulations at various distances z on the line $(x, y) = (0, 0)$. A von Karman spectrum model [12] is selected for the turbulent energy spectrum impacting on the airfoil and an incoming velocity $U = 13.2$ m/s, a turbulence intensity $TI = 0.2$, and a turbulent length scale $\Lambda = 0.005$ m are chosen as representative of an experiment described by Christophe [8]. The airfoil chord is $C = 0.041$ m, and a large aspect ratio airfoil is assumed by using a span $2d = 40\,C$ such that formulation (12) or (11) can be used without any difference for the far-field reference solution.

3.1 Influence of geometrical near-field assumptions

The first comparison is related the results provided by the geometrical far-field expression (12) or (11), the spanwise near-field expression (9) and the direct numerical integration of formulation (5). All formulations do not consider the acoustical near-field corrections. Formulation (5) is integrated numerically using Monte Carlo techniques, further details about the methods and the corresponding implementation are found in Ref. [8]. Figure 3 (top) shows the variation with the distance from the airfoil z of the sound power level for a frequency of 2000 Hz ($kc = 1.5$ and $kd = 30.3$). The results show that all the formulations give similar results for $z > 2d$, pointing out the limit of application of the far-field formulation not taking into account the geometrical near-field effects. The use of the general formulation (5) exhibits a first deviation from the far-field approximation at $z = 2d$ corresponding to the size of the spanwise extent of airfoil and a second deviation around $z = d/20$ corresponding to the chord size. Between those two points, the evolution of the sound power spectrum is linear (in logarithmic scale) with respect to the observer distance. The
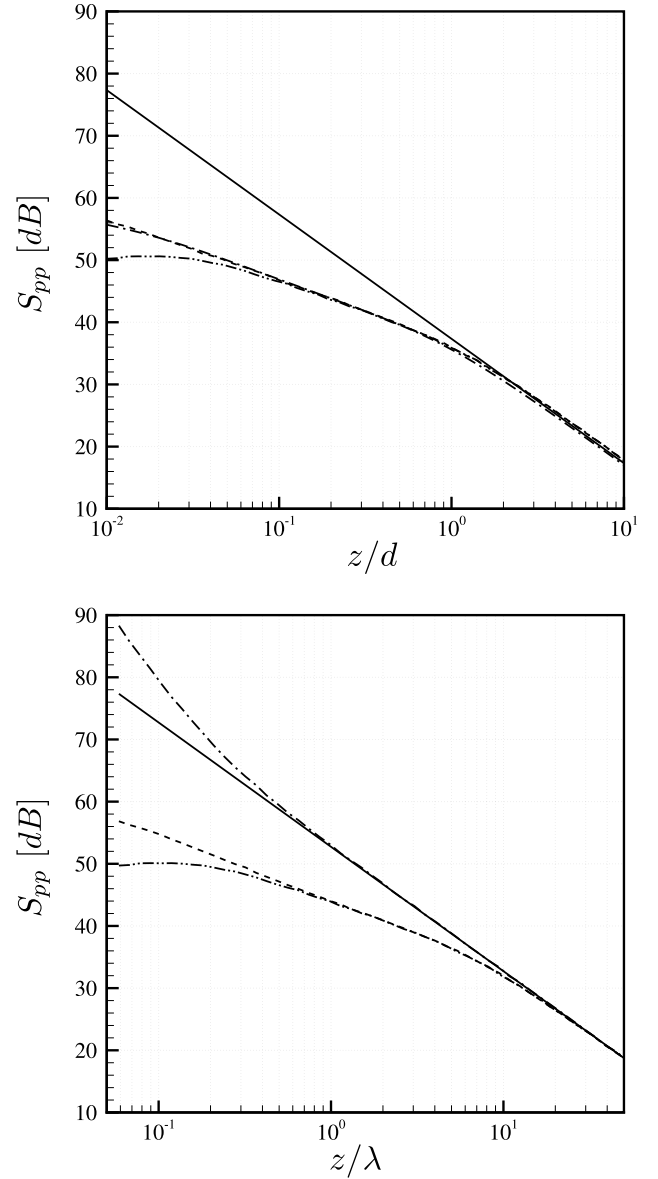
Figure 3: Sound power level predicted above the airfoil at different z locations. (Top) Effect of geometrical near-field assumption : (plain) Amiet's far-field solution (11), (dash-dots) geometrical spanwise near-field formulation (9), (dash-dot-dots) direct numerical integration of formulation (5) without any geometrical assumption and (dashed) with geometrical assumption in the chord direction. (Bottom) Effect of acoustical near-field assumption : (plain) Amiet's far-field solution (11) and (dash-dots) with the acoustical near-field terms, (dash-dot-dots) direct numerical integration of formulation (5) without any geometrical assumption and (dashed) with the acoustical near-field terms.

spanwise near-field expression (9), neglecting chorwise effects and taking spanwise effects only in the scaling term defined in Eq. (7) is compared to the direct numerical integration of formulation (5), without any geometrical assumptions. The maximum difference between formulations is up to 5 dB for $z < d/20$, where chordwise effects start to appear, but improves highly the solution compared to the far-field Amiet's solution. If a direct numerical integration of formulation (5) is performed with similar assumptions than in formulation (9), identical results are obtained between both formulations. The spanwise effects neglected in the exponential term to obtain formulation (9) have then a negligeable effect on the sound results. The near-field expression (9) is attractive for geometrical near-field computation due to its facility of implementation and solution robustness, compared to direct integration requiring higher computational time to obtain similar accuracy due to the low convergence of Monte Carlo techniques. Nevertheless the direct integration of the Amiet's general formulation (5) is a valuable tool to test the different assumptions/simplifications that could be introduced in the Amiet's theory and to quantify the level of accuracy relative to the different assumptions.

3.2 Influence of acoustical far-field assumptions

The same test case is used to evaluate the acoustical far-field approximation introduced in formulation (5) compared to the general formulation (4). Figure 3 (bottom) shows the results obtained using Amiet's theory at different observer distances from the airfoil including geometrical near-field terms and acoustical near-field terms, together with combinations of the different simplifications. A first observation is that the differences are appearing, as expected, for a distance comparable to the magnitude of the acoustical wavelength. The difference observed using acoustical near-field terms on formulation (11) is around 10 dB close to the airfoil while the difference observed on formulation (4) is around 6-7 dB. It seems then that the influence of acoustical near-field terms are attenuated when geometrical near-field terms are taken into account. Finally, we should notice that, for the particular frequency selected ($f = 2000$ Hz), avoiding the use of acoustical near-field terms in the computation can be acceptable while for smaller frequencies, the deviations could increase dramatically, the influence of the acoustical near-field terms increasing with lower frequencies.

4 Concluding remarks

In this work, we have investigated the influence of the geometrical and acoustical near-field effects that could be important in case of observers close to the airfoil surface. Those effects have been studied through an implementation of a generalised formulation of Amiet's theory using the Monte Carlo technique to solve the five dimensional integral involved in the formulation. This generalised formulation revealed to be an efficient tool to verify the assumptions and estimate the potential of simplified formulations based on Amiet's theory taking geometrical near-field effects into account. Nevertheless, the Monte Carlo technique used in the generalised formulation requires a large computational effort to obtain accurate results, but the implementation would be easily used in parallel to improve its efficiency.

References

[1] M. Abramowitz and I. A. Stegun. *Handbook of Mathematical Functions with Formulas, Graphs, and Mathematical Tables.* Courier Dover Publications, 1964.

[2] J. J. Adamczyk. The Passage of an Infinite Swept Airfoil Through an Oblique Gust, 1974. CR 2395.

[3] R. K. Amiet. Acoustic Radiation from an Airfoil in a Turbulent Stream. *Journal of Sound and Vibration*, 41(4):407–420, 1975.

[4] R. K. Amiet. Noise due to Turbulent Flow past a Trailing Edge. *Journal of Sound and Vibration*, 47(3):387–393, 1976.

[5] T. F. Brooks, S. B. Pope, and M. A. Marcolini. Airfoil Self Noise and Prediction. NASA Reference Publication, July 1989.

[6] S. Caro and S. Moreau. Aeroacoustic Modeling of Low Pressure Axial Flow Fans. In *6th AIAA/CEAS Aeroacoustics Conference*, 2000. AIAA-2000-22094.

[7] C. Carton de Wiart, P. Geuzaine, Y. Detandt, J. Manera, S. Caro, Y. Marichal, and G. Winckelmans. Validation of a Hybrid CAA Method: Noise Generated by a Flap in a Simplified HVAC Duct. In *16th AIAA/CEAS Aeroacoustics Conference*, 2010. AIAA-2010-3995.

[8] J. Christophe. *Application of Hybrid Methods to High Frequency Aeroacoustics.* von Karman Institute for Fluid Dynamics, 2011.

[9] N. Curle. The Influence of Solid Boundaries upon Aerodynamic Sound. *Proceedings of the Royal Society of London. Series A, Mathematical and Physical Sciences*, 231(1187):505–514, 1955.

[10] S. A. L. Glegg, S. M. Baxter, and A. G. Glendinning. The Prediction of Broadband Noise from Wind Turbines. *Journal of Sound and Vibration*, 118(2):217–239, 1987.

[11] M. E. Goldstein. *Aeroacoustics.* McGraw-Hill Inc., 1976.

[12] J. O. Hinze. *Turbulence.* McGraw-Hill Inc., 1975.

[13] K. Kucukcoskun, J. Christophe, J. Anthoine, C. Schram, and M. Tournour. An Extension of Amietï£¡s Theory for Spanwise-Varying Incident Turbulence and Broadband Noise Scattering Using a Boundary Element Method. In *16th AIAA/CEAS Aeroacoustics Conference*, 2010. AIAA-2010-3987.

[14] K. Kucukcoskun, J. Christophe, C. Schram, and M. Tournour. Broadband Scattering of the Incoming Turbulence Noise of a Stationary Airfoil: Experimental Validation of the Semi-Analytical Model. Submitted to AIAA J.

[15] M. A. Mac Donald, Y. Nishi, and J. Gullbrand. Notebook Blower Inlet Flows : Experiments and Modeling. In *Fan Noise 2007*, 2007.

[16] O. M. Mohamud and P. Johnson. Broadband Noise Source Models as Aeroacoustic Tools in Designing Low NVH HVAC Ducts. In *SAE Technical Paper Series*, 2006. 2006-01-1192.

[17] S. Moreau and M. Roger. Back-Scattering Correction and Further Extensions of Amietï£¡s Trailing-Edge Noise Model.Part II : Application. *Journal of Sound and Vibration*, 323:397–425, 2009.

[18] S. Moreau, M. Roger, and V. Jurdic. Effect of Angle of Attack and Airfoil Shape on Turbulence-Interaction Noise. In *11th AIAA/CEAS Aeroacoustics Conference*, 2005. AIAA-2005-2973.

[19] R. W. Paterson and R. K. Amiet. Acoustic Radiation and Surface Pressure Characteristics of an Airfoil Due to Incident Turbulence, 1976. CR 2733.

[20] S. Pérennès and M. Roger. Aerodynamic Noise of a Two-Dimensional Wing with High-Lift Devices. In *4th AIAA/CEAS Aeroacoustics Conference*, 1998. AIAA-1998-2338.

[21] M. Roger and S. Moreau. Back-Scattering Correction and Further Extensions of Amietï£¡s Trailing-Edge Noise Model. Part 1: Theory. *Journal of Sound and Vibration*, 286:477–506, 2005.

[22] B. A. Singer, D. P. Lockard, and K. S. Brentner. Computational Aeroacoustic analysis of Slat Trailing-Edge Flow. *AIAA Journal*, 38(9):1558–1564, September 2000.

[23] M. Terracol, E. Labourasse, E. Manoha, and P. Sagaut. Simulation of the 3D Unsteady Flow in a Slat Cove for Noise Prediction. In *9th AIAA/CEAS Aeroacoustics Conference*, 2003. AIAA-2003.3110.

ERCOFTAC Workshops and Summer Schools

Title	Location	Date	Organisers	Email addresses
New challenges in turbulence research II	Les Houches, France.	18/03/2012 – 23/03/2012	Naso, A. Bourgoin, M. Pumir, A. Rousset, B.	Aurore.Naso@ec-lyon.fr
Fast methods in scientific computing	Montestigliano, Italy	26/03/2012	Schmid, P. Gallaire, F. Martinelli, F. Bagheri, S.	info@montestigliano-workshop.com
Workshop on multiscale fractal turbulence	London, UK.	26/03/2012 – 27/03/2012	Laizet, S. Vassilicos, J.C.	s.laizet@imperial.ac.uk j.c.vassilicos@imperial.ac.uk
SIG35 workshop on fundamental aspects of turbulence	Paris, France.	03/05/2012 – 04/05/2012	Cambon, C.	Claude.Cambon@ec-lyon.fr
8th. ECI International conference on boiling and condensation heat transfer	Lausanne, Switzerland	03/06/2012 – 07/06/2012	Thome, R.	John.Thome@epfl.ch
Fundamentals of microscale heat transfer	Lausanne, Switzerland.	11/06/2012 – 15/06/2012	Thome, R	John.Thome@epfl.ch
Unsteady Separation in Fluid-Structure Interaction	Mykonos, Greece.	18/06/2012	Braza, M. Bottaro, A.	marianna.braza@imft.fr alessandro.bottaro@unige.it
3rd International workshop on the turbulent combustion of sprays	Rottmannsaal, Heidelberg-Handschuhsheim, Germany	2/09/2012	Gutheil, E. Masri, A. R. Mastorakos, E. Merci, B. Raman, V. Roekaerts, D. Sadiki, A.	gutheil@iwr.uni-heidelberg.de assaad.masri@sydney.edu.au em257@eng.cam.ac.uk bart.merci@ugent.be v.raman@mail.utexas.edu d.j.e.m.roekaerts@tudelft.nl sadiki@ekt.tu-darmstadt.de
13th Workshop on two-phase flow predictions	Halle, Germany.	17/09/2012 – 20/09/2012	Sommerfeld, M.	martin.sommerfeld@iw.uni-halle.de
20th Polish national fluid dynamics conference	Gliwice, Poland.	17/09/2012 – 20/09/2012	Wroblewski, W. Drobniak, S.	wlodzimierz.wroblewski@polsl.pl drobniak@imc.pcz.czest.pl

ERCOFTAC Special Interest Groups

1. Large Eddy Simulation

Geurts, B.J.
University of Twente, Holland.
Tel: +31 53 489 4125
Fax: +
b.j.geurts@math.utwente.nl

4. Turbulence in Compressible Flows

Comte, P.
University of Poitiers, France.
Tel: +33 5 49 36 60 11
Fax: +33 5 49 36 60 01
Pierre.comte@tea.univ-poitiers.fr

5. Environmental CFD

Armenio, V.
Università di Trieste, Italy.
Tel: +39 040 558 3472
Fax: +39 040 572 082
vi.armenio@gmail.com

10. Transition Modelling

Dick, E.,
University of Gent, Belgium.
Tel: +32 9 264 3301
Fax: +32 9 264 3586
erik.dick@ugent.be

12. Dispersed Turbulent Two Phase Flows

Sommerfeld, M.
Martin-Luther University, Germany.
Tel: +49 3461 462 879
Fax: +49 3461 462 878
martin.sommerfeld@iw.uni-halle.de

14. Stably Stratified and Rotating Flows

Redondo, J.M.
UPC, Spain.
Tel: +34 93 401 7984
Fax: +34 93 401 6090
Redondo@fa.upc.es

15. Turbulence Modelling

Jakirlic, S.
Darmstadt University of Technology, Germany.
Tel: +49 6151 16 3554
Fax: +49 6151 16 4754
s.jakirlic@sla.tu-darmstadt.de

20. Drag Reduction and Flow Control

Choi, K-S.
University of Nottingham, England.
Tel: +44 115 9513 792
Fax: +44 115 9513 800
kwing-so-choi@nottingham.ac.uk

24. Variable Density Turbulent Flows

Anselmet, F.
IMST, France.
Tel: +33 4 91 505 439
Fax: +33 4 91 081 637
fabian.anselmet@irphe.univ-mrs.fr

28. Reactive Flows

Tomboulides, A.
Aristotle University of Thessaloniki, Greece.
Tel: +30 2310 991 306
Fax: +30 2310 991 304
ananiast@enman.auth.gr

32. Particle Image Velocimetry

Stanislas, M.
Ecole Centrale de Lille, France.
Tel: +33 3 20 337 170
Fax: +33 3 20 337 169
stanislas@ec-lille.fr

33. Transition Mechanisms, Prediction and Control

Hanifi, A.
FOI, Sweden.
Tel: +46 8 5550 4334
Fax: +46 8 5550 3481
ardeshir.hanifi@foi.se

34. Design Optimisation

Giannakoglou, K.
NTUA, Greece.
Tel: +30 210 772 1636
Fax: +30 210 772 3789
kgianna@central.ntua.gr

35. Multipoint Turbulence Structure and Modelling

Cambon, C.
ECL Ecully, France.
Tel: +33 4 72 186 161
Fax: +33 4 78 647 145
claude.cambon@ec-lyon.fr

36. Swirling Flows

Braza, M.
IMFT, France.
Tel: +33 5 61 285 839
Fax: +33 5 61 285 899
braza@imft.fr

37. Bio-Fluid Mechanics

Poelma, C.
Delft University of Technology, Holland.
Tel: +31 15 278 2620
Fax: +31 15 278 2947
c.poelma@tudelft.nl

38. Micro-thermofluidics

Borhani, N.
EPFL, Switzerland.
Tel: +41 21 693 3503
Fax: +41 21 693 5960
navid.borhani@epfl.ch

39. Aeroacoustics

Bailly, C.
Ecole Centrale de Lyon, France.
Tel: +33 4 72 186 014
Fax: +33 4 72 189 143
christophe.bailly@ec-lyon.fr

40. Smoothed Particle Hydrodynamics

Le Touzé, D.
Ecole Centrale de Nantes, France.
Tel: +33 2 40 37 15 12
Fax:
david.letouze@ec-nantes.fr

41. Fluid Structure Interaction

Longatte, E.
EDF, France.
Tel: +33 1 30 87 80 87
Fax: +33 1 30 87 77 27
elisabeth.longatte@edf.fr

42. Synthetic Models in Turbulence

Nicolleau, F.
University of Sheffield, England.
Tel: +44 114 22 27867
Fax: +44 114 22 27890
f.nicolleau@sheffield.ac.uk

43. Fibre Suspension Flows

Hämäläinen, J.
Lappeenranta University of Technology, Finland.
Tel: +358 40 596 1999
jari.hamalainen@lut.fi

44. Fundamentals and Applications of Fractal Turbulence

Fortune, V.
Université de Poitiers, France.
Tel: +33 5 49 45 40 44
Fax: +33 5 49 45 36 63
veronique.fortune@lea.univ-poitiers.fr

45. Uncertainty Quantification in Industrial Analysis and Design

Meyers, J.
Katholieke Universiteit Leuven, Belgium.
Tel: +32 16 322 502
Fax: +32 16 322 985
johan.meyers@mech.kuleuven.be

ERCOFTAC Pilot Centres

Alpe – Danube – Adria

Reichl, C.
Austrian Institute of Technology,
Giefinggasse 2,
A-1210 Wien,
Austria.

Tel: +43 1 50550 6605
Fax: +43 1 50550 6439
christoph.reichl@arsenal.ac.at

Belgium

Geuzaine, P.
Cenaero,
CFD Multi-physics Group,
Rue des Frères Wright 29,
B-6041 Gosselies,
Belgium.

Tel: +32 71 919 334
philippe.geuzaine@cenaero.be

Czech Republic

Bodnar, T.
Institute of Thermomechanics AS CR,
5 Dolejskova,
CZ-18200 Praha 8,
Czech Republic.
Tel: +420 224 357 548
Fax: +420 224 920 677
bodnar@marian.fsik.cvut.cz

France – Henri Bénard

Cambon, C.
Ecole Centrale de Lyon.
LMFA,
B.P. 163,
F-69131 Ecully Cedex,
France.
Tel: +33 4 72 18 6161
Fax: +33 4 78 64 7145
claude.cambon@ec-lyon.fr

France South

Braza, M.
IMF Toulouse,
CNRS UMR – 5502,
Allée du Prof. Camille Soula 1,
F-31400 Toulouse Cedex,
France.
Tel: +33 5 61 28 5839
Fax: +33 5 61 28 5899
marianna.braza@imft.fr

France West

Comte, P.
Université de Poitiers,
CEAT/LEA
F-86036 Poitiers Cedex,
France.
Tel: +33 5 49 36 60 11
Fax: +33 5 49 36 60 01
Pierre.comte@tea.univ-poitiers.fr

Germany North

Gauger, N.R.
CCES,
RWTH Aachen Univesity,
Schinkelstr. 2,
D-52062 Aachen,
Germany.
Tel: +49 241 80 98 660
Fax: +49 241 80 92 600
gauger@mathcces.rwth-aachen.de

Germany South

von Terzi, D.
Inst. Thermische Strömungsmaschinen,
Universität Karlsruhe (TH),
Kaiserstr. 12 (Geb. 10.91, Zi. 201)
D-76131 Karlsruhe,
Germany.
Tel: +49 721 608 6829
vonterzi@its.uni-karlsruhe.de

Greece

Papailiou, K.D.
National Tech. University of Athens,
Laboratory of Thermal Turbomachines,
9 Iroon Polytechniou,
P.O. Box 64069,
Gr-15710 Athens,
Greece.
Tel: +30 210 772 1634
Fax: +30 210 772 1658
kpapail@ltt.ntua.gr

Iberian East

Onate, E.
Universitat Politecnica de Catalunya,
Edificio C-1, Campus Norte,
Gran Capitan s/n,
E-08034 Barcelona,
Spain.
Tel: +34 93 401 6035
Fax: +34 93 401 6517
onate@cimne.upc.es

Iberian West

Theofilis, V.
Universidad Politécnica de Madrid,
Plaza Cardenal Cisneros 3,
E-28040 Madrid,
Spain.
Tel: +34 91 336 3291
Fax: +34 91 336 6371
vassilis@torroja.dmt.upm.es

Italy

Martelli, F.
University of Florence,
Department of Energy,
Via Santa Marta 3,
I-50139 Firenze, Italy.
Tel: +39 055 479 6237
Fax: +39 055 479 6342
francesco.martelli@unifi.it

Netherlands

Ooms, G.
J.M. Burgerscentrum,
Research School for Fluid Mechanics,
Mekelweg 2,
NL-2628 CD Delft,
Netherlands.
Tel: +31 15 278 1176
Fax: +31 15 278 2979
g.ooms@wbmt.tudelft.nl

Nordic

Wallin, S.
Swedish Defence Research Agency FOI,
Computational Physics,
S-16490 Stockholm,
Sweden.
Tel: +46 8 5550 3184
Fax: +46 8 5550 3062
stefan.wallin@foi.se

Poland

Rokicki, J.
Warsaw University of Technology,
Inst. of Aeronautics & Applied Mechanics,
ul. Nowowiejska 24,
PL-00665 Warsaw,
Poland.
Tel: +48 22 234 7444
Fax: +48 22 622 0901
jack@meil.pw.edu.pl

Switzerland

Jenny, P.
ETH Zürich,
Institute of Fluid Dynamics,
Sonneggstrasse 3, ML H 38,
CH-8092 Zürich,
Switzerland.
Tel: +41 44 632 6987
Fax: +41 44 632 1147
jenny@ifd.mavt.ethz.ch

United Kingdom

Barton, I.
BAE Systems,
ATC – Sowerby, FPC 267,
P.O. Box 5,
Bristol BS34 7QW,
England.
Tel: +44 117 302 8251
Fax: +44 117 302 8007
iain.barton@baesystems.com

Best Practice Guidelines for Computational Fluid Dynamics of Dispersed Multi-Phase Flows

Editors

Martin Sommerfeld, Berend van Wachem
&
René Oliemans

The simultaneous presence of several different phases in external or internal flows such as gas, liquid and solid is found in daily life, environment and numerous industrial processes. These types of flows are termed multiphase flows, which may exist in different forms depending on the phase distribution. Examples are gas-liquid transportation, crude oil recovery, circulating fluidized beds, sediment transport in rivers, pollutant transport in the atmosphere, cloud formation, fuel injection in engines, bubble column reactors and spray driers for food processing, to name only a few. As a result of the interaction between the different phases such flows are rather complicated and very difficult to describe theoretically. For the design and optimisation of such multiphase systems a detailed understanding of the interfacial transport phenomena is essential. For single-phase flows Computational Fluid Dynamics (CFD) has already a long history and it is nowadays standard in the development of air-planes and cars using different commercially available CFD-tools.

Due to the complex physics involved in multiphase flow the application of CFD in this area is rather young. These guidelines give a survey of the different methods being used for the numerical calculation of turbulent dispersed multiphase flows. The Best Practice Guideline (BPG) on Computational Dispersed Multiphase Flows is a follow-up of the previous ERCOFTAC BPG for Industrial CFD and should be used in combination with it. The potential users are researchers and engineers involved in projects requiring CFD of (wall-bounded) turbulent dispersed multiphase flows with bubbles, drops or particles.

Table of Contents

1. Introduction
2. Fundamentals
3. Forces acting on particles, droplets and bubbles
4. Computational multiphase fluid dynamics of dispersed flows
5. Specific phenomena and modelling approaches
6. Sources of errors
7. Industrial examples for multiphase flows
8. Checklist of '*Best Practice Advice*'
9. Suggestions for future developments
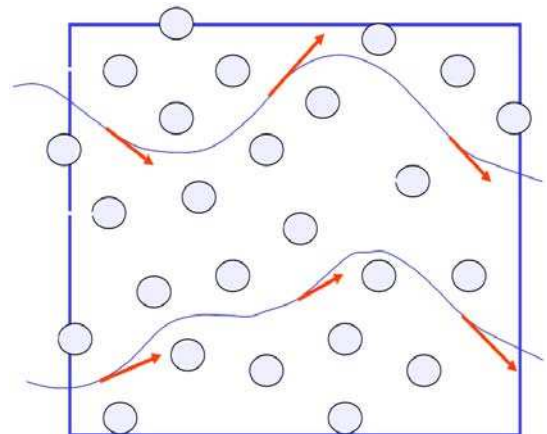
Copies of the Best Practice Guidelines can be acquired electronically from the ERCOFTAC website:

www.ercoftac.org

Or from:

ERCOFTAC CADO
Crown House
72 Hammersmith Road
London W14 8TH, United Kingdom

Tel: +44 (0)207 559 1429
Fax: +44 (0)207 559 1428
Email: Richard.Seoud-ieo@ercoftac.org

The price per copy (not including postage) is:

ERCOFTAC members

First copy	*Free*
Subsequent copies	45 Euros
Students	30 Euros
Non-ERCOFTAC academics	90 Euros
Non-ERCOFTAC industrial	180 Euros